FERMILAB-THESIS-2002-46

SEARCH FOR THE SUPERSYMMETRIC PARTNER OF THE TOP QUARK IN DILEPTON EVENTS PRODUCED IN PROTON-ANTIPROTON COLLISIONS AT $\sqrt{s}$= 1.8 TeV

A Thesis

Submitted to the Faculty

of

Purdue University

by

Arnold Pompoš

In Partial Fulfillment of the

Requirements for the Degree

of

Doctor of Philosophy

December 2002

Dedicated to Šárka, my mother Rózsika and father Gyula.

ACKNOWLEDGMENTS

It is like a sequential electric circuit. It will not function if even only one of its elements is missing. Here, I will try to express my deepest thanks to elements of *my* circuit. Šárka, without your infinite continuous support and love, my doctoral thesis would have stopped at this section. Thank you for making sure that the "Results" chapter also got included. I thank my parents Rózsika and Gyula for the trust in me and love they showed to me every minute of my life. You made it easier for me to make crucial decisions, among them to start and finish my doctoral studies far away from you. Ctirad, Prof. Ctirad Klimčík, my advisor during my studies in Prague. Thank you for opening the door to the world of science for me. You made it possible for me to travel and gain valuable experience at Europe's prime high-energy labs and science institutions.

Who knows what would have happened if I have not met Prof. László Gútay at CERN who offered me the possibility to study at Purdue University. Thank you for making the jump across the Atlantic ocean easy and smooth for me. Because of you and your wife Éva, I continued to be surrounded by a lovely home environment when I arrived in America. While I thanked Šárka for making sure that I got from "Introduction" all the way to "Results", I thank my advisors Prof. Virgil Barnes, Prof. Daniela Bortoletto and Dr. Stephan Lammel, for making sure that the chapters in between were not empty! You were the ones who introduced me to the environment of Fermilab, one of the world's prime high-energy physics laboratories. I thank you for your endless support, trust and optimism. You were "The Living Examples" showing me how the hard scientific work can be fun and enjoyable. (Prof. Barnes on a cherry picker in the CDF assembly hall at 3 a.m. building the plug calorimeter.) Please allow me to express one more time my special thank to Dr. Stephan Lammel, my

closest advisor (his office was right next to mine) at Fermilab. Stephan, you have created a scientific and human environment around you, which I think is far beyond any expectations a graduate student can have! It was a privilege to work with you and listen to your advise. Thank you.

Judy Jackson, thank you for offering me to be part of your team at the Office of Public Affairs at Fermilab. It was a great and very enjoyable experience to work with you. Last, but not least I thank everybody who helped me when I made my first steps in learning English and also those who helped me to keep my culture alive while being away from my home. Among them, Dr. Cathy Heinsohn, a friend and my true English teacher, thank you for your prompt reply ("Hi Arnold, I do not have a room for you, but welcome to America") to my first e-mail to the Purdue community desperately looking for a place to stay: "Hello, I Arnold is look for accommodation.". It started a priceless friendship with you. Also Prof. Arnold Tubis and the faculty of the Physics Department at Purdue, thank you for always standing behind me when various English and culture originated bumps on my road arose. Teta and Ujo Málkovi, I admire your patience. I thank you for your never-ending cheering for my best. Dr. Aba Teleki, Želka and Paul Budinsky, and many other friends whom all I cannot list here, thank you for your friendship.

I hereby gratefully acknowledge financial support during my PhD thesis research, from the U. S. Department of Energy research grant number DE-FG02-91ER40681 to the Purdue University High Energy Physics group, Task G.

TABLE OF CONTENTS

Page

Page

Page

Page

LIST OF TABLES

Table Page

Table Page

Table Page

Appendix Table Page

LIST OF FIGURES

Figure Page

Figure Page

Figure Page

Figure Page

Figure Page

ABSTRACT

Pomposš, Arnold, Ph.D., Purdue University, December, 2002. Search for the Supersymmetric Partner of the Top Quark in Dilepton Events Produced in Proton-Antiproton Collisions at $\sqrt{s}$= 1.8 TeV. Major Professors: Virgil Barnes, Daniela Bortoletto.

Supersymmetric partners of top quarks, stops, will be pair produced at the Fermi National Accelerator Laboratory in proton-antiproton collisions at a center-of-mass energy $\sqrt{s}$= 1.8 TeV if kinematically accessible. Within the framework of the Minimal Supersymmetric extension of the Standard Model, the stop quarks are assumed to decay into a lepton, a bottom quark and a supersymmetric neutrino, sneutrino. Thus the experimental signature of stop presence in the data would be two opposite electric charge leptons, hadronic jets and substantial energy imbalance in the detector due to the escaping, undetected sneutrinos. We searched a total of $\int \mathcal{L}dt$ = 107.2 pb^{-1} of data collected by the Collider Detector at Fermilab experiment. No evidence of a stop signal has been found which allows us to calculate a 95% confidence level upper limit on the number of stop-originated events in the data of this size. We have translated this into a 95% confidence level exclusion region in the stop versus sneutrino mass plane.

1. Introduction

Each era of human history had great thinkers who believed that "law and order" exist in our Nature. They were convinced that Nature, its structure and laws can be described and understood all the way down to the most fundamental levels. Due to the tremendous technical improvements of available experimental techniques, the view of the underlying structure and governing law of the world is constantly evolving. First, it was the theory of four elements, fire, water, soil and air. It continued through Dalton's atomic theory to the deterministic description of solid bodies, light, thermodynamic ensembles, electromagnetic and gravitational field. At the frontier today, we believe the right description of Nature is the probabilistic theory of the tiniest elements of our world, the smallest entities we are made of, the elementary particles. The understanding and description of this microworld reveals its very fundamental connection to the megaworld of stars, galaxies and ultimately the universe itself.

So far the most successful theory of elementary particles and their interactions is the Standard Model (SM) [1, 2, 3]. It is based on fundamental symmetries existing in the quantum world. It gives a very good description of all phenomena existing at energy levels we can probe with current experiments. Nevertheless, physicists realize that it cannot be the ultimate theory of everything, because it does not answer some fundamental questions. It fails to incorporate gravity, it breaks down at very high energy scales and does not predict the values of its parameters. Therefore, there must be a theory beyond the Standard Model.

One good candidate for such a theory is the Minimal Supersymmetric extension of the Standard Model (MSSM) [4, 5, 6]. It introduces the idea of the existence of a new symmetry of Nature, supersymmetry (SUSY), which unifies the spin-half fermions

Table 1.1
Running periods of the Fermilab Tevatron and corresponding luminosities collected by the CDF experiment.

	Run 1A	**Run 1B**
Data Taking Period	08/1992 - 05/1993	01/1994 - 06/1995
Integrated Luminosity	18.6 pb^{-1}	88.6 pb^{-1}

with integer-spin bosons. SUSY doubles our world of elementary particles, because it assigns to each SM particle a supersymmetric partner whose spin differs by one half.

In this thesis we present the results of our experimental search for the supersymmetric partner of the top quark, the stop quark. We searched the proton-antiproton collision data (see Tab. 1.1) produced at a center-of-mass energy of 1.8 trillion electron volts, collected by the Collider Detector at Fermilab (CDF) at the Fermi National Accelerator Laboratory, near Chicago, USA.

The thesis has the following structure. In chapter 2 we give a brief introduction to the Standard Model. Chapters 3 and 4 summarize the theory of supersymmetry, describe the Minimal Supersymmetric Standard Model and show its particle content focusing on particles related to our search. In chapter 5 we describe the experimental apparatus, Fermilab's proton-antiproton collider, the Tevatron, and the detector of the $p\bar{p}$ collision products, the CDF detector. In chapter 6 we introduce our strategy of the search for the superpartner of the top quark. Chapters 7 and 8 define particles in terms of detector measurable quantities. Chapter 9 introduces the data set in which we searched for the stop quark. Various background sources mimicking the stop signal are described in chapter 10. In chapter 11 we introduce the Monte Carlo event generator which allows us to study in great detail the expected stop and background events. The first comparison of observed data with expected signal and background is done in chapter 12. In chapter 13, selection cuts on various event variables are developed in order to enhance the signal and reduce the background. The uncertainties of our measurement are discussed in chapter 14. Finally, results of the search

and the conclusion are presented in chapters 15 and 16. Appendices A-E describe some of the mathematical tools used to build the MSSM. Appendix F lists the lepton identification cuts applied to select the Run 1A and Run 1B SUSY dilepton samples. Appendix G shows the trigger spectrum of the analyzed data, and Appendix H summarizes the number of generated and expected stop events for various points in the MSSM parameter space.

2. The Standard Model

The Standard Model (SM) is the most successful theory of elementary particles and their interactions we currently have. Its validity has been confirmed in many ways since it was created. For example, one of its biggest triumphs was the prediction, and later the experimental observation of the electroweak bosons [7]. It was built by Glashow-Salam-Weinberg as a gauge theory where particles are treated as quanta of fields on which various representations of the gauge group act. It was a beautiful theory, but quite far from reality, because all elementary particles were predicted to be massless. The foundations of the theory were nevertheless so strong, that it had not been immediately turned over, but instead, a serious effort to overcome this problem was made. By adding a scalar field, the Higgs field[8], to the theory the dream came true. A simple mechanism to generate masses to particles was developed and a hunt for new particles predicted by the Standard Model begun. It was at the Fermi National Accelerator Laboratory (Fermilab) in 1995, where the heaviest elementary particle, the top quark was discovered[9]. In 2000 Fermilab provided the direct evidence for the next to last missing particle, the tau neutrino [10]. So far, the evidence for the manifestation of the Higgs field in Nature, the Higgs boson, is missing. Teams of scientists from all over the world are collecting collision data at Fermilab hoping to discover the Higgs boson in the near future. In the following sections we give a brief overview of the structure of the Standard Model.

2.1. Particle Content of the Standard Model

The fundamental particle constituents of the Standard Model (see Tab. 2.1) are *leptons* (electron, muon, tau) and *quarks* (up, down, charm, strange, top, bottom). The *gauge particles* (photon, Z-boson, W-bosons, gluons) carry the interactions. The

Higgs particle will be described later as the one responsible for breaking the electroweak symmetry. Leptons and quarks are fermions (spin $\frac{1}{2}$ particles) while the gauge particles and the Higgs particle are bosons (spin 1 particles).

In the matter sector, *leptons* and *quarks*[1] are grouped into 3 families:

$$1^{\text{st}}\text{ family}: \; L_e = \begin{pmatrix} \nu_e \\ e \end{pmatrix}_L \; , \; R_e = e_R \; , L_u = \begin{pmatrix} u \\ d' \end{pmatrix}_L \; , \; R_u = u_R \; , \; R_d = d_R \quad (2.1)$$

$$2^{\text{nd}}\text{ family}: \; L_\mu = \begin{pmatrix} \nu_\mu \\ \mu \end{pmatrix}_L \; , \; R_\mu = \mu_R \; , L_c = \begin{pmatrix} c \\ s' \end{pmatrix}_L \; , \; R_c = c_R \; , \; R_s = s_R \quad (2.2)$$

$$3^{\text{rd}}\text{ family}: \; L_\tau = \begin{pmatrix} \nu_\tau \\ \tau \end{pmatrix}_L \; , \; R_\tau = \tau_R \; , L_t = \begin{pmatrix} t \\ b' \end{pmatrix}_L \; , \; R_t = t_R \; , \; R_b = b_R . \quad (2.3)$$

The handedness indices "L" and "R" are introduced in the Appendix B. The fact, that there are only 3 families in the theory, is derived purely from experimental observation. Notice also, that there are no right handed neutrinos (ν_R) in the theory. This is again an assumption based on experimental observation, although some recent experimental results hint that this assumption should be revisited[12].

The gauge sector possesses the following *gauge bosons*: $\gamma,\ Z^0,\ W^+,\ W^-,\ g_i$, where $i \in \{\bar{R}B,\ \bar{R}G,\ \bar{B}R,\ \bar{G}R,\ \bar{B}G,\ \bar{G}B,\ \frac{1}{\sqrt{2}}(\bar{R}R - \bar{B}B),\ \frac{1}{\sqrt{6}}(\bar{R}R + \bar{B}B - 2\bar{G}G)\ \}$ with $R,\ B$ and G being the color quantum numbers[2].

The electroweak symmetry breaking sector has the *Higgs particle* : H

---

[1]Notice that the down type quarks have primes in their names. They are related to the weak eigenstates (d, s, b) of the unbroken SM via CKM matrix $\mathbf{V_{CKM}}$ [11] which mixes the families as $(d', s', b')^T \equiv \mathbf{V_{CKM}}(d, s, b)^T$

[2]One would expect nine existing combinations of three quark colors. However, as we will see later, gluons must carry color, therefore one of the possible combinations, $\frac{1}{\sqrt{3}}(\bar{R}R+\bar{B}B+\bar{G}G)$, is forbidden, since it is colorless.

Table 2.1
List of Standard Model particles and their most fundamental properties. Each of these particles are currently believed to be pointlike and elementary, *i.e.* without any further internal structure. Electric charge Q and the hypercharge Y are given in units of the elementary charge $|e| = 1.609 \times 10^{-19}\ C$.

Leptons (spin = 1/2)				
Name		Mass (GeV/c^2)	Electric charge Q	Hypercharge Y
ν_e	electron neutrino	$< 7 \times 10^{-9}$	0	$(\nu_e)_L = -1/2$
e	electron	0.000511	-1	$e_L = -1/2$, $e_R = -1$
ν_μ	muon neutrino	$< 3 \times 10^{-4}$	0	$(\nu_\mu)_L = -1/2$
μ	muon	0.106	-1	$\mu_L = -1/2$, $\mu_R = -1$
ν_τ	tau neutrino	$< 3 \times 10^{-2}$	0	$(\nu_\tau)_L = -1/2$
τ	tau	1.7771	-1	$\tau_L = -1/2$, $\tau_R = -1$
Quarks (spin = 1/2)				
u	up	0.005	$+2/3$	$u_L = 1/6$, $u_R = 2/3$
d	down	0.01	$-1/3$	$d_L = 1/6$, $d_R = -1/3$
c	charm	1.5	$+2/3$	$c_L = 1/6$, $c_R = 2/3$
s	strange	0.2	$-1/3$	$s_L = 1/6$, $s_R = -1/3$
t	top	175	$+2/3$	$t_L = 1/6$, $t_R = 2/3$
b	bottom	4.7	$-1/3$	$b_L = 1/6$, $b_R = -1/3$
Symmetry breaking particle (spin = 1)				
H	Higgs	?	0	1/2
Gauge particles (spin = 1)				
γ	photon	0	0	0
W^-	boson	80.22	-1	-1
W^+	boson	80.22	$+1$	$+1$
Z^0	boson	91.187	0	0
g	gluons	0	0	0

2.2. Symmetries of the Standard Model

The gauge group of the Standard Model is $SU(3)_C \times SU(2)_L \times U(1)_Y$, where C denotes color, L handedness and Y hypercharge[3].

There are three coupling constants (one for each group) entering the theory (α_s, g, and $g'/2$ for the $SU(3)_C,\ SU(2)_L,\ U(1)_Y$ respectively). The electromagnetic (g') and the weak (g) couplings are not independent. They are related by the relations:

$$g' = g\tan\theta_W, \quad e = g\sin\theta_W, \quad e = g'\cos\theta_W,$$

where the weak angle θ_W is a parameter of the Standard Model and is determined by experiment[13], and e is the elementary electric charge.

After introducing the particle content and the gauge group of the SM, the next step is to assign the particles their transformation properties. The left handed leptons ($L_l,\ l \in \{e,\ \mu,\ \tau\}$) and quarks ($L_q,\ q \in \{u,\ c,\ t\}$) are weak-isospin (*i.e.* $SU(2)_L$) doublets. The right handed leptons ($R_l,\ l \in \{e,\ \mu,\ \tau\}$) and quarks ($R_q,\ q \in \{u,\ d,\ c,\ s,\ t,\ b\}$) are weak-isospin ($SU(2)_L$) singlets. Each of the quarks are color ($SU(3)_C$) triplets and all the other particles are color ($SU(3)_C$) singlets. The interactions of particles are carried by the gauge fields:

- A_μ for $U(1)_Y$ the electromagnetic interaction
- b^a_μ for $SU(2)_L$ the weak interaction, $a = 1, 2, 3$
- B^a_μ for $SU(3)_C$ the strong interaction, $a = 1, \ldots 8$.

The mathematical expressions of the local infinitesimal gauge transformations acting on the particles and gauge fields are given in Tab. 2.2.

In order to illustrate the gauge model building process, we focus on the electroweak sector $SU(2)_L \times U(1)_Y$ of the Standard Model. The electroweak (EWK) part of the SM Lagrangian is:

$$\mathcal{L}_{EWK} = \mathcal{L}_{gauge} + \mathcal{L}_{lepton} + \mathcal{L}_{quark} \tag{2.4}$$

[3]The relationship between the $SU(2)_L$ T_3 isospin component, the $U(1)_Y$ hypercharge Y and the electric charge Q of a particle is given by Gell-Mann-Nishijima relation $Q = T_3 + Y$.

where,

$$\begin{aligned}
\mathcal{L}_{lepton} &= \sum_{l=e,\mu,\tau} \bar{R}_l i\gamma^\mu(\partial_\mu + ig' A_\mu Y) R_l \\
&\quad + \sum_{l=e,\mu,\tau} \bar{L}_l i\gamma^\mu(\partial_\mu + ig' A_\mu Y + \frac{ig}{2}\vec{\tau}\cdot\vec{b}_\mu) L_l \qquad (2.5) \\
\mathcal{L}_{quark} &= \sum_{q=u,d,c,s,t,b} \bar{R}_q i\gamma^\mu(\partial_\mu + ig' A_\mu Y) R_q \\
&\quad + \sum_{q=u,c,t} \bar{L}_q i\gamma^\mu(\partial_\mu + ig' A_\mu Y + \frac{ig}{2}\vec{\tau}\cdot\vec{b}_\mu) L_q \qquad (2.6) \\
\mathcal{L}_{gauge} &= -\frac{1}{4} F^a_{\mu\nu} F_a^{\mu\nu} - \frac{1}{4} f_{\mu\nu} f^{\mu\nu} \qquad (2.7)
\end{aligned}$$

with

$$f_{\mu\nu} = \partial_\nu A_\mu - \partial_\mu A_\nu, \quad F^a_{\mu\nu} = \partial_\nu b^a_\mu - \partial_\mu b^a_\nu + g\epsilon_{jk}{}^a b^j_\mu b^k_\nu \qquad (2.8)$$

where $\bar{L}_l = (\bar{\nu}_L, \quad \bar{l}_L)$. Similarly for $\bar{L}_q$. This Lagrangian is invariant under local $SU(2)_L \times U(1)_Y$ transformation shown in Tab. 2.2. It is clear that Eqs.(2.4-2.6) do not give the complete description of our world of particles because what they describe are **massless particles** only. From experiments we know that three of the gauge bosons and all of the fermions are massive however. In order to adjust the theory to agree with experimental results, we cannot just simply add mass terms to the Lagrangian, because the local gauge invariance would be broken and we would completely lose the original idea of building the theory as a gauge theory. The way out is, to admit that the $SU(2)_L \times U(1)_Y$ symmetry is broken! *But how?*

2.3. Electroweak Symmetry Breaking through the Higgs Mechanism

From the very beginning of the Standard Model history, scientists tried to find mechanisms, that would break the $SU(2)_L \times U(1)_Y$ symmetry, allowing the mass terms of leptons and gauge bosons to be present in the Lagrangian. We will briefly mention three models for symmetry breaking: (1) the single elementary Higgs model; (2) the two elementary Higgs doublet model; (3) the composite Higgs model with dynamical symmetry breaking.

Table 2.2

Transformation of particles and gauge fields under gauge transformations. The $\vec{b}_\mu$ ($\vec{B}_\mu$) has 3(8) components $b^a_\mu(B^a_\mu)$. Variables $\alpha(x)$, $\vec{\beta}(x)$, and $\vec{\gamma}(x)$ are the infinitesimal parameters of the transformations and Y is the hypercharge. By $\vec{\tau}$ ($\vec{\lambda}$) we denoted the 3(8) Pauli(Gell-Mann) matrices. The g', g, α_s are the coupling constants. The cross products are defined via the structure constants f_{abc} of the groups, $(A \times B)_a = f_{abc} A_b B_c$.

	$L_{l,q}$	$\rightarrow$	$(1 - ig'Y\alpha(x))L_{l,q}$
	$R_{l,q}$	$\rightarrow$	$(1 - ig'Y\alpha(x))R_{l,q}$
$U(1)_Y$	A_μ	$\rightarrow$	$A_\mu + \partial_\mu \alpha(x)$
	$\vec{b}_\mu$	$\rightarrow$	$\vec{b}_\mu$
	$\vec{B}_\mu$	$\rightarrow$	$\vec{B}_\mu$
	$L_{l,q}$	$\rightarrow$	$(1 - \frac{1}{2} ig\vec{\tau}\vec{\beta}(x))L_{l,q}$
	$R_{l,q}$	$\rightarrow$	$R_{l,q}$
$SU(2)_L$	A_μ	$\rightarrow$	A_μ
	$\vec{b}_\mu$	$\rightarrow$	$\vec{b}_\mu + \partial_\mu \vec{\beta}(x) + g\vec{\beta}(x) \times \vec{b}_\mu$
	$\vec{B}_\mu$	$\rightarrow$	$\vec{B}_\mu$
	L_l	$\rightarrow$	L_l
	L_q	$\rightarrow$	$(1 - i\alpha_s \vec{\lambda}\vec{\gamma}(x))L_q$
	R_l	$\rightarrow$	R_l
$SU(3)_C$	R_q	$\rightarrow$	$(1 - i\alpha_s \vec{\lambda}\vec{\gamma}(x))R_q$
	A_μ	$\rightarrow$	A_μ
	$\vec{b}_\mu$	$\rightarrow$	$\vec{b}_\mu$
	$\vec{B}_\mu$	$\rightarrow$	$\vec{B}_\mu + \partial_\mu \vec{\gamma}(x) + \alpha_s \vec{\gamma}(x) \times \vec{B}_\mu$

2.3.1. Elementary Higgs Model

1. Single Higgs doublet approach:

We introduce a field ϕ called the Higgs field [8]

$$\phi = \begin{pmatrix} \phi^+ \\ \phi^0 \end{pmatrix} \tag{2.9}$$

which behaves as a complex scalar under Lorentz transformations and as a doublet under $SU(2)_L$ isospin transformation with isospin $T_\phi = \frac{1}{2}$ and hypercharge $Y_\phi = \frac{1}{2}$. Its kinetic, mass and interaction terms are described by the standard renormalizable Lagrangian of scalar particles:

$$\mathcal{L}_{scalar} = \left|\mathcal{D}_\mu \phi\right|^2 - V(\phi), \tag{2.10}$$

where the covariant derivative D_μ and the potential $V(\phi)$ are:

$$\mathcal{D}_\mu = \partial_\mu + ig' A_\mu Y + \frac{ig}{2}\vec{\tau}\cdot\vec{b}_\mu, \qquad V(\phi) = \mu^2\phi^\dagger\phi + \lambda(\phi^\dagger\phi)^2 \tag{2.11}$$

Notice, that μ^2 is the name of the parameter and it does not mean the square of μ. The λ parameter is chosen to be positive in order to have the scalar potential bounded from below. The Lagrangian of Eq.(2.10) is invariant under $SU(2)_L \times U(1)_Y$ symmetry, therefore we can add it to the electroweak Lagrangian (2.4).

If $\mu^2 > 0$, then the Lagrangian $\mathcal{L}_{scalar}$ describes a QED theory with a massless photon A_μ and two real scalar particles ϕ and ϕ^* with the same mass $\sqrt{\mu^2}$. Interesting thing happens, if we consider the other case, namely $\mu^2 < 0$. Then the scalar potential $V(\phi)$ has a non-vanishing minimum and the Higgs field gets a non-zero vacuum expectation value $\langle\phi^\dagger\phi\rangle = -\frac{1}{2}\mu^2/\lambda$[8]. By choosing the vacuum expectation value (VEV) of the Higgs to be

$$\langle\phi\rangle = \begin{pmatrix} 0 \\ v/\sqrt{2} \end{pmatrix}, \tag{2.12}$$

where $v/\sqrt{2} \equiv \sqrt{(-\frac{1}{2}\mu^2/\lambda)}$, we can redefine the field ϕ of Eq.(2.9) by introducing four new real scalar fields $\vec{\xi}(x), H(x)$ by the expression:

$$\phi(x) \equiv \exp(\frac{i\vec{\xi}(x).\vec{\tau}}{2v}) \begin{pmatrix} 0 \\ (v + H(x))/\sqrt{2} \end{pmatrix}. \tag{2.13}$$

By **choosing** $\vec{\beta} = \frac{\vec{\xi}}{gv}$ in the $SU(2)$ gauge transformations shown in Tab. 2.2, we can eliminate the $\vec{\xi}$ field such a way that we obtain for the Higgs field the following form:

$$\phi(x) \to \phi'(x) = \frac{1}{\sqrt{2}} \begin{pmatrix} 0 \\ v + H(x) \end{pmatrix}. \tag{2.14}$$

Substituting[4] (2.14) into $\mathcal{L}_{scalar}$ in Eq.(2.10) we obtain

$$\begin{aligned} \mathcal{L}_{scalar} &= \tfrac{1}{2}\partial_\mu H(x)\partial^\mu H(x) + \frac{1}{4}g^2 W^+_\mu W^{-\mu}(v + H(x))^2 \\ &+ \frac{1}{8}\frac{e^2}{\sin^2\theta_W \cos^2\theta_W} Z^0_\mu Z^{0\mu}(v + H(x))^2 \\ &- (\mu^2(\tfrac{1}{2}(v + H(x)))^2 + \lambda(\tfrac{1}{2}(v + H(x)))^4)\ldots \end{aligned} \tag{2.15}$$

where $\gamma_\mu = A_\mu \cos\theta_W + b^3_\mu \sin\theta_W$, $Z^0_\mu = -A_\mu \sin\theta_W + b^3_\mu \cos\theta_W$, $W^\pm_\mu = \frac{b^1_\mu \mp i b^2_\mu}{\sqrt{2}}$ are the physical states, of the photon γ, Z^0, and $W^\pm$ vector bosons. After regrouping Eq.(2.15) we can read out the Higgs and gauge bosons masses[5]:

$$m^2_H = -2\mu^2 = 2\lambda v^2, \quad m_W = g\frac{v}{2}, \quad m_Z = \frac{m_W}{\cos^2\theta_W}, \quad m_\gamma = 0$$

By introducing the Higgs field, so far we were able to give masses to the vector bosons, but the scalar field is still decoupled from the fermionic world and the fermions are still massless. The solution to this problem is hidden in the Yukawa coupling terms, which for the first family read:

$$\mathcal{L}_{Yukawa} = -\left(\lambda_u \bar{R}_u \bar{\phi}^\dagger \cdot L_u + \lambda_d \bar{R}_d \phi^\dagger \cdot L_u + \lambda_e \bar{R}_e \phi^\dagger \cdot L_e + \text{h.c.}\right), \tag{2.16}$$

where λ_u, λ_d and λ_e are the Yukawa coupling constants[6]. This Lagrangian is also invariant under electroweak symmetry and can be added to (2.4). We demonstrate how fermions acquire mass by using the first family leptons only. By plugging the

[4]Because Lagrangian $\mathcal{L}_{scalar}$ is $SU(2)_L$ invariant, it has the same form in ϕ and ϕ' fields.

[5]We can determine the real value of the v parameter by relating the relevant terms from $\mathcal{L}_{lepton}$ to already measured Fermi coupling constant by noting $v = (G_F\sqrt{2})^{-1/2} \simeq 246$ GeV.

[6]An important observation for the future supersymmetry construction is that in order to give masses to the up-type quarks, we have to have the $\bar{\phi}$ field present in the Lagrangian (2.16). The field $\bar{\phi} \equiv i\sigma_2\phi^* = \begin{pmatrix} (\phi^0)^* \\ -\phi^- \end{pmatrix}$ is the conjugate to ϕ. This field cannot be present in the SUSY Yukawa terms, and that is the reason for the necessity of having two Higgs doublets in SUSY.

Higgs field from (2.14) into $\mathcal{L}_{Yukawa}$ we obtain the electron mass term as well as a term describing the coupling of the Higgs to electrons.

$$\mathcal{L}_{Yukawa}^{electron} = -\lambda_e \frac{v + H(x)}{\sqrt{2}} (\bar{e}_R e_L + \bar{e}_L e_R) = -m_e \bar{\psi}_e \psi_e - \frac{\lambda_e}{\sqrt{2}} H \bar{\psi}_e \psi_e, \tag{2.17}$$

where the electron mass is

$$m_e = \frac{v \lambda_e}{\sqrt{2}}$$

and we introduced ψ_e by (see Appendix B):

$$e_R \equiv \tfrac{1}{2}(1 + \gamma_5)\psi_e \qquad e_L \equiv \tfrac{1}{2}(1 - \gamma_5)\psi_e.$$

Similar procedure applies to the leptonic members of other families and to quarks.

2. Two Higgs doublets approach:

The Standard Model can be built even with one Higgs doublet only. However, in "beyond the SM" theories, it proves to be useful (and necessary) to have two Higgs doublets

$$\phi_1 = \begin{pmatrix} \phi_1^+ \\ \phi_1^0 \end{pmatrix}, \quad \phi_2 = \begin{pmatrix} \phi_2^0 \\ \phi_2^- \end{pmatrix}. \tag{2.18}$$

Both of them are $SU(2)_L$ doublets with $T_\phi = \frac{1}{2}$, but with opposite hypercharge $|Y_\phi| = 1/2$. Their Lagrangian is

$$\mathcal{L}_{scalar} = \left|\mathcal{D}_\mu \phi_1\right|^2 + \left|\mathcal{D}_\mu \phi_1\right|^2 - V(\phi_1, \phi_2) \ , \tag{2.19}$$

with

$$V(\phi_1, \phi_2) = (\ \phi_1^\dagger \quad \phi_2^\dagger\ )\, \mathbf{M}^2 \begin{pmatrix} \phi_1 \\ \phi_2 \end{pmatrix} + \cdots \ , \tag{2.20}$$

where $\mathbf{M}^2$ is a 2×2 matrix. As in section (2.3.1), the fields ϕ_1 and ϕ_2 obtain non-zero VEVs,

$$\langle \phi_1 \rangle = \begin{pmatrix} 0 \\ v_1/\sqrt{2} \end{pmatrix}, \quad \langle \phi_2 \rangle = \begin{pmatrix} 0 \\ v_2/\sqrt{2} \end{pmatrix} \tag{2.21}$$

and we can follow the idea from the previous section to build a model with two Higgs doublets. It turns out that the ratio $\frac{v_1}{v_2}$ will play an important role in supersymmetry. In fact, in scientific literature it has its own name, $\tan\beta \equiv \frac{v_1}{v_2}$.

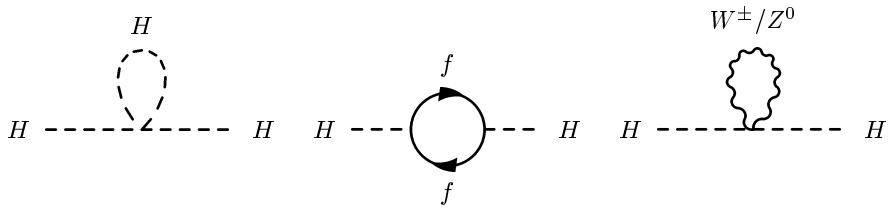

Figure 2.1. Scalar, fermion and vector boson loop corrections to the Higgs mass.

2.3.2. Difficulties with the Higgs Sector

Having introduced Higgs as an elementary particle, some problems arose with the radiative corrections to its mass. There are three contributing diagrams[7] (see Figs. 2.1). It can be shown by using the Feynman rules derived from the Lagrangian (2.17) in [14], that the above diagrams yield the following contributions [15]:

- the scalar loop diagram is proportional to $g^2 \int \frac{d^4k}{(2\pi)^4} \frac{1}{k^2 - m_\phi^2}$;
- the fermion loop diagram is equal to $-2N(f)\lambda_f^2 \int \frac{d^4k}{(2\pi)^4} \frac{1}{k^2 - m_f^2}$ where $N(f)$ is the multiplicity factor. For instance for quarks, $N(q) = 3$;
- the vector boson loop diagram is proportional to $g^2 \int \frac{d^4k}{(2\pi)^4} \frac{1}{k^2 - m_W^2}$.

All these terms are **quadratically divergent** as the internal loop momentum k gets very large.

One could argue that this divergency does not cause a major problem, because most likely the SM is not the final theory (*f.i.* because it does not describe gravity), so it has to be valid only up to certain energies, let us say up to the Planck mass M_{Pl}, when a new, so called grand unified theory (GUT) starts to take over. Taking this mass as the cut off (Λ) for k, then the divergent behavior is eliminated. For the

[7] The logarithmically divergent diagrams are not our major concerns, because in analogy with QED, they can be easily renormalized.

physical mass of the Higgs boson in the lowest order of perturbation theory, we would then have the following relation:

$$m_H^2 \sim m_0^2 + \text{radiative correction terms} \tag{2.22}$$

After plugging in the radiative corrections in terms of the cut-off Λ, we obtain

$$m_H^2 \sim m_0^2 - \Lambda^2 \sum \lambda_i \tag{2.23}$$

The coupling constants λ_i are assumed to be of order of 1. There is a strong belief, that the Higgs mass m_H is not larger than of the order of 1 TeV [16, 17]. This means that if Λ is really of order of M_{Pl} (*i.e.* about 10^{19} GeV/c^2), the m_0 (the bare mass of the Higgs boson) parameter must compensate for the huge contributions of the radiative corrections in such a way that the resulting m_H is around 1 TeV. This compensation would have to be incredibly precise as we go to higher and higher orders in perturbation theory. This problem is known as the "fine tuning problem".

It is possible to postulate that the theory should be fine tuning free, but the price would be that the cut-off parameter Λ must be below approximately 1 TeV. This then suggests the existence of new phenomena around the energy scale of 1 TeV. One such example of new physics could be the existence of Supersymmetry. But what kind of physics has Nature chosen above 1 TeV would nevertheless still remain unknown.

2.3.3. Composite Higgs Particle

This alternative to the EWK symmetry breaking model was proposed by Weinberg and Susskind [18]. It introduces a new gauge interaction acting on new flavor fermions, (U, D). The nature of the new interaction is very similar to quantum chromodynamics (QCD), the part of the SM which describes the strong interactions. The U, D fermions are massless, coupled to $SU(2)_L \times U(1)_Y$ exactly the same way as the SM (u, d) quarks are, but the nonperturbative scale Λ (mentioned in the previous section) for this new section would be much larger than the electroweak scale. The model is built such a way, that the $SU(2)_L \times U(1)_Y$ symmetry is spontaneously broken by chiral condensates

of U or D fields and it contains a composite field with $T = \frac{1}{2}, Y = 1/2$ (just as the elementary Higgs field had) that provides a mechanism to give mass to the gauge bosons.

As an example of such a "Strong Dynamics Theory" we briefly mention Technicolor. The new fermions are called technifermions. Those are the fields on which the fundamental representation of the technicolor gauge group acts. This gauge interaction is denoted G_{TC}. The theory contains also composite scalars (such as the Higgs particle) and particles called technimesons. These particles are bound states of technifermions, held together by the technicolor interaction. The gauge group of the theory is then $G_{TC} \times SU(3)_C \times SU(2)_L \times U(1)_Y$, where TC, C, L, Y stand for technicolor, color, handedness and hypercharge respectively. The standard particles and the technimesons are technicolor singlets. The G_{TC} gauge group is usually picked to be $SU(N)$, so the technifermions are technicolor "N-plets".

Very popular are models, where $N = 8$. At hadron colliders, TC octets, like technipions, can be pair produced and an intensive search for them is on going in the the Tevatron data[19].

3. Supersymmetry

3.1. Introducing Supersymmetry

In the previous section we described the Standard Model, as the most successful theory of elementary particles and their interactions we currently have. In Sec. 2.3.2 we also mentioned that SM is not a fundamental theory and a theory beyond the Standard Model is needed. One of the most popular ideas on which a Standard Model extension could be built is the postulation of the existence of a new symmetry in the world of elementary particles, supersymmetry (SUSY). It in some sense unifies bosons (spin 1) and fermions (spin 1/2). Symbolically we can say $\boxed{Q\,|Boson\rangle = |fermion\rangle}$ and $\boxed{Q\,|fermion\rangle = |Boson\rangle}$, where Q is the SUSY generator described in the following section. SUSY predicts that each Standard Model particle has a supersymmetric partner, with all quantum numbers the same, but the spin. Their spin differs by $\frac{1}{2}$. To all known fermions, there exists a scalar superpartner and to all known bosons, there exists a fermionic superpartner. The names of the superpartners are made by adding a "s" in front of the SM fermion's name or adding an "ino" to the end of the SM boson's name. For example, the scalar superpartner of the *top* quark is called the *stop* quark and the fermionic partner of the *photon* is called the *photino*.

In the following sections we follow Lykken's Introduction to Supersymmetry[20] and Martin's A Supersymmetry Primer[21] to describe a supersymmetric extension of the Standard Model. We start from the definition of the SUSY algebra and introduce the supersymmetric generalization of scalar, chiral and gauge fields. Then the SUSY invariant Lagrangian is introduced and with the help of the SM fields and their superpartners the Minimal Supersymmetric Standard Model is constructed.

3.1.1. The SUSY Algebra

Supersymmetry postulates the existence of a superspace with four antisymmetric coordinates θ^α, $\overline{\theta}_{\dot{\alpha}}$, where $\alpha = 1, 2$ and $\dot{\alpha} = 1, 2$. Antisymmetric means they are Grassmann variables, *i.e.* they satisfy the following conditions:

$$\{\theta^\alpha, \theta^\beta\} = \{\overline{\theta}_{\dot{\alpha}}, \overline{\theta}_{\dot{\beta}}\} = \{\theta^\alpha, \overline{\theta}_{\dot{\beta}}\} = 0. \tag{3.1}$$

These coordinates are the superpartners of the usual space time coordinates x^μ. The differential analysis with these Grassmann variables can be found in [22]. The most important rules for differentiation and integration we show in Appendix C.

In general, it is possible to construct supersymmetry with an arbitrary number of generators. But it can be shown [21], that only SUSY with $N = 1$ generator can contain chiral fields in a 4-dimensional space time.

The SUSY algebra is generated by spinors[1] Q, $\overline{Q}$ and a scalar R. It is an extension of Poincaré space time symmetries (which are generated by M_{mn} and P_m). The complete $N = 1$ supersymmetry algebra in 4-dimensions is defined by the following relations[20]:

$$\{Q_\alpha, Q_\beta\} = \{\overline{Q}_{\dot{\alpha}}, \overline{Q}_{\dot{\beta}}\} = 0 \tag{3.2}$$

$$\{Q_\alpha, \overline{Q}_{\dot{\beta}}\} = 2\sigma^m_{\alpha\dot{\beta}} P_m \tag{3.3}$$

$$[Q_\alpha, P_m] = [\overline{Q}_{\dot{\alpha}}, P_m] = 0 \tag{3.4}$$

$$[Q_\alpha, M_{mn}] = \sigma_{mn\alpha}{}^{\beta} Q_\beta \tag{3.5}$$

$$[\overline{Q}^{\dot{\alpha}}, M_{mn}] = \bar{\sigma}^{\dot{\alpha}}_{mn\,\dot{\beta}} \overline{Q}^{\dot{\beta}} \tag{3.6}$$

$$[P_m, P_n] = 0 \tag{3.7}$$

$$[M_{mn}, P_p] = i(\eta_{np} P_m - \eta_{mp} P_n) \tag{3.8}$$

$$[M_{mn}, M_{pq}] = -i\left(\eta_{mp} M_{nq} - \eta_{mq} M_{np} - \eta_{np} M_{mq} + \eta_{nq} M_{mp}\right) \tag{3.9}$$

[1] We use the Weyl representation of Dirac matrices and the two-component Weyl spinors. Any general four-component Dirac spinor ψ is therefore split into two, two-component Weyl spinors ψ^α and $\bar{\psi}_{\dot{\alpha}}$ such that $\psi = \begin{pmatrix} \psi^\alpha \\ \bar{\psi}_{\dot{\alpha}} \end{pmatrix}$. The Weyl spinor representation of the Lorentz group is described in the Appendix D.

$$[Q_\alpha, R] = RQ_\alpha \tag{3.10}$$

$$[\overline{Q}_{\dot\alpha}, R] = -R\overline{Q}_{\dot\alpha} \tag{3.11}$$

$$[P_m, R] = [M_{mn}, R] = 0, \tag{3.12}$$

where η_{mn} is the flat metric tensor (see Appendix A), σ^m are the 4-dimensional sigma matrices and σ^{mn} are the SL(2,C) generators (see Appendix D).

In order to find a group element of a global SUSY transformation, we have to rewrite the anticommutators of (3.2) and (3.3) into commutators. It can be done by using two constant spinors θ and $\overline{\theta}$ whose components θ^α and $\overline{\theta}_{\dot\alpha}$ are Grassmann variables. Then, by using the summation convention from the Appendix D, we can rewrite (3.2) and (3.3) into

$$\begin{aligned} [\,\theta Q, \theta Q\,] &= [\,\overline{\theta}\,\overline{Q}, \overline{\theta}\,\overline{Q}\,] = 0 \\ [\,\theta Q, \overline{\theta}\,\overline{Q}\,] &= 2\theta\sigma^m\overline{\theta}P_m. \end{aligned} \tag{3.13}$$

This way we obtained an algebra, whose general group element is[2]:

$$\Omega(x, \theta, \overline{\theta}, \omega) = \mathrm{e}^{i[-x^m P_m + \theta Q + \overline{\theta}\,\overline{Q}]}\mathrm{e}^{-\frac{i}{2}\omega^{mn}M_{mn}}. \tag{3.14}$$

For pure superspace translations (3.14)

$$\Omega(0, \xi, \bar\xi, 0) = \mathrm{e}^{i[\xi Q + \bar\xi\,\overline{Q}]}. \tag{3.15}$$

It can be shown[20] that

$$\Omega(0, \xi, \bar\xi, 0)\Omega(x, \theta, \overline{\theta}, 0) = \Omega(x + i\theta\sigma\bar\xi - i\xi\sigma\overline{\theta}, \theta + \xi, \overline{\theta} + \bar\xi, 0). \tag{3.16}$$

Therefore the coordinate supershifts (supertranslations) are given by:

$$\begin{aligned} x^m &\longrightarrow x'^m = x^m + i\theta\sigma^m\bar\xi - i\xi\sigma^m\overline{\theta}, \\ \theta^\alpha &\longrightarrow \theta'^\alpha = \theta^\alpha + \xi^\alpha, \\ \overline{\theta}_{\dot\alpha} &\longrightarrow \overline{\theta}'_{\dot\alpha} = \overline{\theta}_{\dot\alpha} + \overline{\xi}_{\dot\alpha}, \end{aligned} \tag{3.17}$$

[2]Note that this group element gives the prescription to find how fields change under translations (x^m) and rotations(ω^{mn}) in ordinary commutative space and under translations (θ and $\overline{\theta}$) in superspace.

where ξ and $\bar{\xi}$ are infinitesimal Grassmann variables. In the next sections we identify the fields, superfields, on which the SUSY group acts.

3.1.2. Scalar Superfields

In analogy with the commutative scalar fields, we define a scalar superfield as a field $\Phi(x,\theta,\overline{\theta})$ which under supertranslations (3.17) does not change:

$$\Phi(x,\theta^{\alpha},\overline{\theta}_{\dot{\alpha}}) = \Phi'(x',\theta'^{\alpha},\overline{\theta}'_{\dot{\alpha}}). \tag{3.18}$$

The most general form(its Taylor expansion) of a scalar superfield is:

$$\begin{aligned}\Phi(x,\theta,\overline{\theta}) &= f(x) + \theta\phi(x) + \overline{\theta}\bar{\chi}(x) + \theta\theta m(x) + \overline{\theta\theta}n(x) \\ &+\theta\sigma^{m}\overline{\theta}v_{m}(x) + (\theta\theta)\overline{\theta}\bar{\lambda}(x) + (\overline{\theta\theta})\theta\psi(x) + (\theta\theta)(\overline{\theta\theta})d(x),\end{aligned} \tag{3.19}$$

where $\phi(x)$, $\bar{\chi}(x)$, $\bar{\lambda}(x)$, $\psi(x)$ are spinors, θ and $\overline{\theta}$ are Grassmann variables, $f(x)$, $m(x)$, $n(x)$, $d(x)$ are complex scalars and $v_m(x)$ is a vector[3].

3.1.3. Chiral Superfields

Extending the formalism of spinor bundles[23] to the 8-dimensional superspace, or following [20, 24], the 8 additional[4] (super) components D_{α}, $\overline{D}_{\dot{\alpha}}$ of the covariant derivative D have the following form:

$$D_{\alpha} = \partial_{\alpha} + i\sigma^{m}_{\alpha\dot{\beta}}\overline{\theta}^{\dot{\beta}}\partial_{m}, \qquad \overline{D}_{\dot{\alpha}} = \overline{\partial}_{\dot{\alpha}} + i\bar{\sigma}^{m}_{\dot{\alpha}\beta}\theta^{\beta}\partial_{m}. \tag{3.20}$$

Then we define the left and right chiral superfields Φ_L, Φ_R as scalar superfields which solve the following two equations:

$$\overline{D}_{\dot{\alpha}}\Phi_L = 0 \qquad D_{\alpha}\Phi_R = 0. \tag{3.21}$$

It can be shown[20] that the most general form of Φ_L (similarly for Φ_R) is given by:

$$\Phi_L(x^{m},\theta^{\alpha}) = A(x) + \sqrt{2}\theta\psi(x) + \theta\theta F(x)$$

[3]There are no higher terms in powers of θ since $\theta^2 = 0$

[4]I addition to the 4 commutative components $D_m = \partial_m$

$$+i\theta\sigma^m\overline{\theta}\partial_m A(x) + \frac{i}{\sqrt{2}}(\theta\theta)\partial_m\psi(x)\sigma^m\overline{\theta} - \tfrac{1}{4}(\theta\theta)(\overline{\theta\theta})\Box A(x), \tag{3.22}$$

where $A(y)$ and $F(y)$ are complex scalar fields, and $\psi(y)$ is a left handed Weyl spinor. Chiral superfields, especially their F components will be very important when we construct the Lagrangian of a SUSY gauge theory. Their transformation property under supertranslations is given by:

$$\delta_\xi F = -\sqrt{2}i\partial_m\psi\sigma^m\bar{\xi}. \tag{3.23}$$

It is worth to note that so far we have considered only global SUSY transformations where the θ and ξ parameters in the group elements given by (3.14) and (3.15) were constant spinors. Under this SUSY transformation, the chiral fields transform as follows:

$$\Phi_L \longrightarrow e^{i\xi Q}\Phi_L \qquad \Phi_R \longrightarrow e^{-i\bar{\xi}\overline{Q}}\Phi_R. \tag{3.24}$$

However, when one builds gauge theories, the symmetry transformations are required to be local. In order to preserve the gauge invariance of the Lagrangian, one had to introduce vector fields of gauge bosons. A similar philosophy applies in the case of superfields, as we will see in the next section.

3.1.4. Vector Superfields

A vector superfield V is defined by the relation

$$V(x,\theta,\overline{\theta}) = V^\dagger(x,\theta,\overline{\theta}). \tag{3.25}$$

This leads to the following Taylor form [25]:

$$\begin{aligned} V(x,\theta,\overline{\theta}) &= \left(1+\frac{1}{4}\theta\theta\overline{\theta\theta}\Box\right)C(x) + \left(i\theta + \frac{1}{2}\theta\theta\sigma^m\overline{\theta}\partial_m\right)\chi(x) \\ &+ \frac{i}{2}\theta\theta\left[M(x)+iN(x)\right] + \left(-i\overline{\theta} + \frac{1}{2}\overline{\theta\theta}\sigma^m\theta\partial_m\right)\overline{\chi}(x) \\ &- \frac{i}{2}\overline{\theta\theta}\left[M(x)-iN(x)\right] - \theta\sigma_m\overline{\theta}A^m(x) + i\theta\theta\overline{\theta\lambda}(x) \\ &- i\overline{\theta\theta}\theta\lambda(x) + \frac{1}{2}\theta\theta\overline{\theta\theta}D(x), \end{aligned} \tag{3.26}$$

where $C,\ M,\ N$ and D are real scalar fields, χ and λ are Weyl spinors, and A^m is a vector field.

To build the desired gauge theory, we would like to make the global transformations (3.24) local, but in such a way that the chirality conditions (3.21) will be preserved. It can be achieved by going from a constant ξ to a chiral superfield Λ, such that $\overline{D}_{\dot{\alpha}}\Lambda = 0$. The chiral and vector superfields will then transform under the local gauge transformations as

$$\Phi_L \longrightarrow e^{i\Lambda Q}\Phi_L \qquad \Phi_R \longrightarrow e^{-i\Lambda^\dagger \overline{Q}}\Phi_R \qquad e^{gV} \longrightarrow e^{-ig\Lambda^\dagger}e^{gV}e^{ig\Lambda}, \tag{3.27}$$

where g is a gauge coupling. As in ordinary quantum field theories we can choose a gauge without loss of generality. We will do the same here. **The Wess-Zumino gauge** is defined by choosing

$$\chi(x) = C(x) = M(x) = N(x) \equiv 0. \tag{3.28}$$

Then the vector superfield in W-Z gauge is:

$$V = -\theta\sigma_m\overline{\theta}A^m + i(\theta\theta)\overline{\theta}\bar{\lambda} - i(\overline{\theta\theta})\theta\lambda + \tfrac{1}{2}(\theta\theta)(\overline{\theta\theta})D. \tag{3.29}$$

The vector superfield contains a vector A^m, a spinor λ and a real scalar field D. In [26] one can find the variations of the components of a vector superfield (3.26) under SUSY transformation (3.17). As we will see, only the variation of the D component:

$$\delta_\xi D = -\xi\sigma^m\partial_m\overline{\lambda} + \bar{\xi}\sigma^m\partial_m\lambda \tag{3.30}$$

plays an important role in building the SUSY Lagrangian.

3.1.5. The Superfield Strength Term

In this section, we show the generalization of the commutative field strength tensor $F^{\mu\nu}$ to the superfield formalism.

Abelian case:

For any vector superfield V we define the superfield strengths W_α, $\overline{W}_{\dot{\alpha}}$ [24] by

$$W_\alpha = -\frac{1}{8}(\overline{DD})\mathrm{e}^{-2V}D_\alpha\mathrm{e}^{2V}, \qquad \overline{W}_{\dot{\alpha}} = \frac{1}{8}(DD)\mathrm{e}^{2V}\overline{D}_{\dot{\alpha}}\mathrm{e}^{-2V}. \tag{3.31}$$

It can be shown, that these are chiral superfields. Writing the vector superfield V in the W-Z gauge, and switching to $x^m \to x^m + i\theta\sigma^m\overline{\theta}$ coordinates, the Taylor expansions of the superfield strength read[20]:

$$W_\alpha = -i\lambda_\alpha(x) + \theta_\alpha D(x) - \frac{i}{2}(\sigma^m\bar{\sigma}^n\theta)_\alpha(\partial_m A_n - \partial_n A_m)(x) + (\theta\theta)\sigma^m_{\alpha\dot{\beta}}\partial_m\bar{\lambda}^{\dot{\beta}}(x) \quad (3.32)$$

Similarly for $\overline{W}_{\dot{\alpha}}$. The W_α field contains a spinor λ, a real scalar field D and the desired $F_{mn} \equiv \partial_m A_n - \partial_n A_m$.

Non-Abelian generalization:

Let us denote by T^a the generators of the Lie algebra for a non-Abelian gauge group. Writing V (the vector superfield) and Λ (the chiral superfield) in terms of their components we have

$$V = T^a V_a, \qquad \Lambda = T^a \Lambda_a \quad .$$

The definitions of W_α and $\overline{W}_{\dot{\alpha}}$ are still the same as in the Abelian case, but their resulting Taylor expansions in the W-Z gauge are different [20]:

$$W_\alpha = -i\lambda_\alpha(x) + \theta_\alpha D(x) - \sigma^{mn\beta}_\alpha\theta_\beta F_{mn}(x) + (\theta\theta)\sigma^m_{\alpha\dot{\beta}}\nabla_m\bar{\lambda}^{\dot{\beta}}(x), \quad (3.33)$$

where

$$F_{mn} = \partial_m A_n - \partial_n A_m + i[A_m, A_n], \quad \text{and} \quad \nabla_m\bar{\lambda}^{\dot{\beta}} = \partial_m\bar{\lambda}^{\dot{\beta}} + i[A_m, \bar{\lambda}^{\dot{\beta}}]. \quad (3.34)$$

The superfield strength now contains the "correct" field strength tensor F_{mn} and the known ∇_m connection of the Yang-Mills theories.

3.1.6. The Lagrangian of Supersymmetry

In the previous section we identified the main ingredients (scalar, chiral, and vector superfields and the super field strength) of a locally supersymmetric theory. The remaining task is to find a gauge and SUSY invariant action. Mathematically speaking, we are looking for an action S, such that $\delta_\xi S = 0$, or, equivalently, we are seeking a Lagrangian density $\mathcal{L}$ which transforms as a total derivative under gauge

and SUSY transformations. We have already seen some good candidate terms, such as the F component of a chiral superfield or the D component of a vector superfield. They both transform under SUSY transformation as total derivatives (see Eqs.(3.23) and (3.30)). Before writing down the explicit form of the Lagrangian density, it should be noted that for all chiral superfields Φ_L, Φ_R (shown in Eq.3.22), and for all vector superfields V (from Eq. 3.29)

$$\int d^2\theta \Phi_L = F, \qquad \int d^2\bar{\theta} \Phi_R = F^*, \qquad \int d^4\theta V = D, \tag{3.35}$$

where $d^2\theta$, $d^2\bar{\theta}$ and $d^4\theta$ are defined in Appendix C.

Kinetic terms:

It can be proven that a product of a right-handed and a left-handed chiral superfield is self conjugate, and is therefore a vector superfield. Using the Taylor expressions for Φ_L, the fact that $\Phi_L^\dagger = \Phi_R$ and the integral (3.35) we obtain:

$$\int d^4\theta \Phi_L \Phi_L^\dagger = FF^* - \phi \partial_\mu \partial^\mu \phi^* - i\overline{\psi}\sigma_\mu \partial^\mu \psi. \tag{3.36}$$

We see that this expression contains kinetic terms for the spinor ψ and the scalar ϕ but not F field. Based on this fact, we may conjecture that a chiral super field describes two propagating fields and one non propagating auxiliary field. Unfortunately, the product $\Phi_L \Phi_L^\dagger$ is not gauge invariant. In order to fix this problem, we consider instead of (3.36) the following term in W-Z gauge[20]:

$$\mathcal{L}_{kin} = \int d^4\theta \Phi_L^\dagger e^{2g'V} \Phi_L = \left|D_\mu \phi\right|^2 - i\overline{\psi}\sigma_\mu D^\mu \psi + g\phi^* D\phi + ig'\sqrt{2}\left(\phi^* \lambda\psi - \overline{\lambda\psi}\phi\right) + |F|^2, \tag{3.37}$$

where $D_\mu = \partial_\mu + ig' A_\mu^a T_a$ is the covariant derivative. Note that this time the Lagrangian is gauge invariant and is richer too. It contains not only kinetic terms, but also some interaction terms that will be described later.

Interaction terms:

Using the Taylor expansions for two left-handed chiral superfields it is not hard to show that their product is also a chiral left-handed superfield. Therefore, the product of any left-handed chiral superfields is a left-handed chiral superfield. The extraction

of the F component of the two and the three product using (3.35) yields to some interaction terms[21]:

$$\int d^2\theta \Phi_{1,L}\Phi_{2,L} = \phi_1 F_2 + \phi_2 F_1 - \psi_1\psi_2, \tag{3.38}$$

$$\int d^2\theta \Phi_{1,L}\Phi_{2,L}\Phi_{3,L} = \phi_1\phi_2 F_3 + \phi_1 F_2\phi_3 + \phi_1\phi_2 F_3 - \psi_1\phi_2\psi_3 - \phi_1\psi_2\psi_3 - \psi_1\psi_2\phi_3. \tag{3.39}$$

As the next step, we define the *superpotential* as a holomorphic function of left-handed chiral superfields. Due to renormalisibility conditions, the third power in Φ is the highest power which can still enter the superpotential:

$$f(\Phi_i) = \sum_i k_i\Phi_i + \frac{1}{2}\sum_{i,j} m_{ij}\Phi_i\Phi_j + \frac{1}{3}\sum_{i,j,k} g_{ijk}\Phi_i\Phi_j\Phi_k, \tag{3.40}$$

where Φ_i are left-handed chiral superfields and k_i, m_{ij} and g_{ijk} are constants with mass powers 0, 1 and 2 respectively. The F term (the actual contribution of fields to the SUSY Lagrangian) of the superpotential (3.40) can be extracted by evaluating the integral:

$$\mathcal{L}_{inter} \equiv \int d^2\theta f(\Phi_i) + h.c. \tag{3.41}$$

By noting that

$$\left(\frac{\partial^2 f(\Phi_i)}{\partial\Phi_j\partial\Phi_k}\right)_{\Phi_i=\phi_i,\Phi_j=\phi_j} = M^{ij} + y^{ijk}\phi_k \quad \text{and} \quad \left(\frac{\partial f(\Phi_i)}{\partial\Phi_j}\right)_{\Phi_j=\phi_j} = M^{ij}\phi_j + \frac{1}{2}y^{ijk}\phi_j\phi_k\,. \tag{3.42}$$

Eq.(3.41) can be rewritten in a more compact form:

$$\mathcal{L}_{inter} = \left[\sum_j \left(\frac{\partial f(\Phi_i)}{\partial\Phi_j}\right)_{\Phi_j=\phi_j} F_j - \frac{1}{2}\sum_{j,k}\left(\frac{\partial^2 f(\Phi_i)}{\partial\Phi_j\partial\Phi_k}\right)_{\Phi_i=\phi_i,\Phi_j=\phi_j}\psi_j\psi_k + h.c.\right]. \tag{3.43}$$

Now it is obvious that the F terms do not propagate, they are auxiliary fields and can be removed from the theory by using their equations of motion $\partial(\mathcal{L}_{kin}+\mathcal{L}_{inter})/\partial F_j = 0$, which result in the following constraints:

$$F_j = -\left[\frac{\partial f(\Phi_i)}{\partial\Phi_j}\right]^*_{\Phi_j=\phi_j}. \tag{3.44}$$

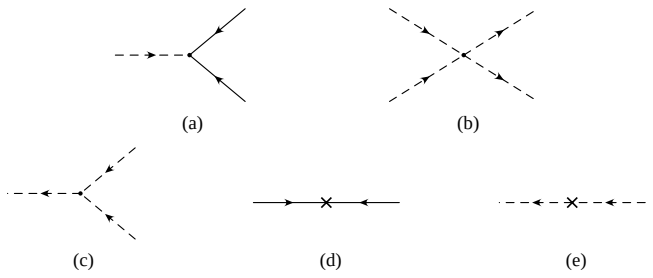

Figure 3.1. SUSY vertices from $\mathcal{L}_{inter}$: (a) scalar-fermion-fermion vertex (b) quartic scalar interaction vertex (c) cubic scalar vertex (d) fermion and (e) scalar mass diagrams.

After substituting the constraints back in to (3.43) we have the final form of the interaction term of the SUSY Lagrangian density:

$$\mathcal{L}_{inter} = -\frac{1}{2}\left[\sum_{j,k}\left(\frac{\partial^2 f(\Phi_i)}{\partial\Phi_j\partial\Phi_k}\right)_{\Phi_i=\phi_i,\Phi_j=\phi_j}\psi_j\psi_k + h.c.\right] - \sum_j\left|\frac{\partial f(\Phi_i)}{\partial\Phi_j}\right|^2_{\Phi_j=\phi_j}. \quad (3.45)$$

By plugging (3.42) into (3.45) we note that (i) the first term of (3.45) gives a mass M^{ii} to the fermions and introduces the Yukawa couplings, (ii) the second term gives the same mass M^{ii} to the scalars and also describes their mutual interactions and (iii) the relevant Feynman vertices are the ones shown on Fig. 3.1.

Gauge terms:

Since the superfield strength W_α and W^α are left handed chiral superfields, their product is again a left handed chiral superfield which suggests that its F component could be a good candidate for a Lagrangian entry. It can be shown, that the product $W^\alpha W_\alpha$ is gauge invariant under the **Abelian** gauge transformation and that $Tr(W^\alpha W_\alpha)$ is invariant under the **non-Abelian** gauge transformation. Therefore the gauge and SUSY invariant gauge term is defined by[20]:

$$\mathcal{L}_{gauge} \equiv \frac{1}{32g'^2}\int d^2\theta Tr(W_\alpha W^\alpha) \quad (3.46)$$

which yields:

$$\mathcal{L}_{gauge} = -\frac{1}{4}F^a_{\mu\nu}F^{\mu\nu}_a + \frac{1}{2}D_aD^a + \left(-\frac{i}{2}\lambda^a\sigma_\mu\partial^\mu\overline{\lambda}_a + \frac{1}{2}gf^{abc}\lambda_a\sigma_\mu A^\mu_b\overline{\lambda}_c + h.c.\right). \quad (3.47)$$

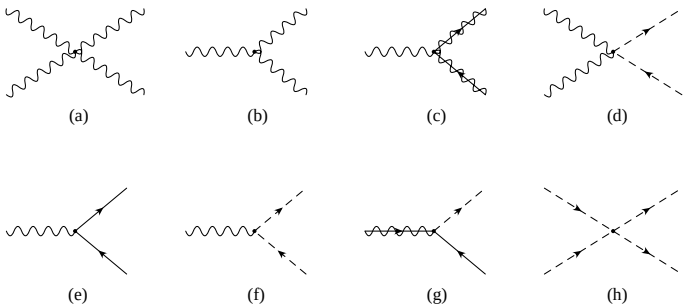

Figure 3.2. SUSY vertices from $\mathcal{L}_{gauge}$: (a,b) the gauge bosons vertices (c) coupling of gauginos (solid line overlayed with a squiggly line) to gauge bosons (d-f) coupling of gauge bosons to scalars (dashed line) and fermions (solid line) (g) gaugino coupling to a scalar and a fermion (h) scalar quartic vertex.

where f^{abc} are the structure constants of the gauge group. Here the involved fields were decomposed into the base T^a of the generators of the gauge group.

Notice that the D component of the superfield strength does not have a kinetic term, *i.e.* it is a non-propagating field and can be eliminated by its Euler-Lagrangian equations of motion $\partial(\mathcal{L}_{kin} + \mathcal{L}_{gauge})/\partial D^a = 0$, whose solutions are given by:

$$D_a = -g' \sum_{i,j} \phi_i^* T_a^{ij} \phi_j. \tag{3.48}$$

After eliminating the D term from (3.37) and from (3.47) we arrive with the following contribution to the Lagrangian:

$$\mathcal{L}_D = -\frac{1}{2} \sum_a \left| \sum_{i,j} g' \phi_i^* T_{ij}^a \phi_j \right|^2 . \tag{3.49}$$

The appropriate Feynman diagrams coming from $\mathcal{L}_{gauge}$ are shown on the Fig. 3.2. The following expression summarizes in a compact form the SUSY and gauge invariant Lagrangian density:

$$\begin{aligned}
\mathcal{L} &= \mathcal{L}_{kin} + \mathcal{L}_{inter} + \mathcal{L}_{gauge} \\
&= \left|D_\mu \phi\right|^2 - i\overline{\psi}\sigma_\mu D^\mu \psi + ig'\sqrt{2}\left(\phi^* \lambda\psi - \overline{\lambda\psi}\phi\right) \\
&- \left[\sum_{j,k} \left(\frac{\partial^2 f(\Phi_i)}{\partial\Phi_j \partial\Phi_k}\right)_{\Phi_i=\phi_i, \Phi_j=\phi_j} \psi_j \psi_k + h.c.\right]
\end{aligned}$$

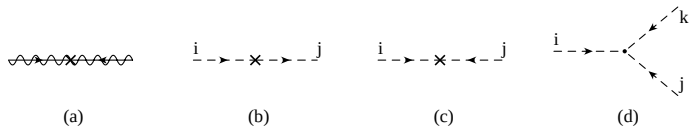

Figure 3.3. Vertices from the soft supersymmetry-breaking terms: (a) gaugino mass (b) and (c) are the scalar mass terms (d) is the cubic scalar interaction.

$$
\begin{aligned}
- & \sum_j \left| \frac{\partial f(\Phi_i)}{\partial \Phi_j} \right|^2_{\Phi_j=\phi_j} - \frac{1}{2} \sum_a \left| \sum_{i,j} g' \phi_i^* T_{ij}^a \phi_j \right|^2 \\
- & \frac{1}{4} F_{\mu\nu}^a F_a^{\mu\nu} + \left(-\frac{i}{2} \lambda^a \sigma_\mu \partial^\mu \overline{\lambda}_a + \frac{1}{2} g f^{abc} \lambda_a \sigma_\mu A_b^\mu \overline{\lambda}_c + h.c. \right).
\end{aligned}
\tag{3.50}
$$

3.1.7. SUSY Breaking

As we mentioned in the Sec.(3.1.6), the fermions ψ and their scalar partners ϕ have equal masses. Therefore in experiments, for example a scalar electron with the mass 0.5 MeV/c^2 should have been observed. Since there is no evidence of such a mass degeneracy between particles and their superpartners, SUSY can not be an exact symmetry at our energy scales *i.e.* SUSY has to be broken at or above the EWK scale. A complete description of such a breaking mechanism has not been yet constructed.

Throughout our search for SUSY, we will treat the SUSY breaking by the most widely used method. We add extra terms to the Lagrangian, which explicitly violate supersymmetry. This parameterization is called "**soft susy breaking**". The terms to be added have to satisfy certain requirements, such as still allowing the theory to cancel the quadratic divergences. In the work of Grisaru and Girardello [27] the possible soft SUSY breaking terms are listed: (1) $-\frac{1}{2} m_l \bar{\lambda}_l \lambda_l$; (2) $-m_{\phi_i}^2 \left|\phi_i\right|^2$; (3) $-B_{ij}\phi_i\phi_j + h.c.$; (4) $-A_{ijk}\phi_i\phi_j\phi_k + h.c.$, where ϕ, λ are scalar and gaugino fields respectively. The related Feynman diagrams to these soft terms are shown in Fig.3.3. With the addition of these terms to the SUSY Lagrangian, we also have to deal with the parameters that come along. We will study this issue in details in Sec.(3.2.4) for

Table 3.1
Chiral supermultiplets of the first family in MSSM.

Superfield Name	spin 0	spin 1/2	$SU(3)_C$, $SU(2)_L$, $U(1)_Y$
$\hat{Q}$	$(\widetilde{u}_L \;\; \widetilde{d}_L)$	$(u_L \;\; d_L)$	$(\,\mathbf{3},\,\mathbf{2}\,,\,\frac{1}{6})$
$\hat{\overline{U}}$	$\widetilde{u}^*_R$	$u^\dagger_R$	$(\,\overline{\mathbf{3}},\,\mathbf{1},\,-\frac{2}{3})$
$\hat{\overline{D}}$	$\widetilde{d}^*_R$	$d^\dagger_R$	$(\,\overline{\mathbf{3}},\,\mathbf{1},\,\frac{1}{3})$
$\hat{L}$	$(\widetilde{\nu} \;\; \widetilde{e}_L)$	$(\nu \;\; e_L)$	$(\,\mathbf{1},\,\mathbf{2}\,,\,-\frac{1}{2})$
$\hat{\overline{E}}$	$\widetilde{e}^*_R$	$e^\dagger_R$	$(\,\mathbf{1},\,\mathbf{1},\,1)$

the theory, called the Minimal Supersymmetric Standard Model (MSSM), a supersymmetric extension of the Standard Model.

3.2. The Minimal Supersymmetric Standard Model

In the following few sections we use the previously built general SUSY framework (superfields, SUSY Lagrangian, Feynman vertices and soft SUSY breaking terms) to supersymmetrize the Standard Model. The Minimal Supersymmetric Standard Model will be constructed[5].

3.2.1. Particle Content of the MSSM

Matter Sector:

Table 3.1 shows the first generation quarks, leptons and their superpartners entering the MSSM. The quark superfield $\hat{Q}$ consists of two $SU(2)_L$ isospin doublets

$$\begin{pmatrix} \widetilde{u}_L \\ \widetilde{d}_L \end{pmatrix}, \quad \begin{pmatrix} u \\ d \end{pmatrix}_L , \tag{3.51}$$

[5]As previously, Weyl spinors will be used. In Appendix E we show the chiral particle content of the SM in the two component Weyl spinor formalism.

Table 3.2
Supermultiplets of the Higgs sector in MSSM.

Superfield Names	spin 0	spin 1/2	$SU(3)_C$, $SU(2)_L$, $U(1)_Y$
$\hat{H}_u$	$(H_u^+ \quad H_u^0)$	$(\widetilde{H}_u^+ \quad \widetilde{H}_u^0)$	$(\mathbf{1}, \mathbf{2}, +\frac{1}{2})$
$\hat{H}_d$	$(H_d^0 \quad H_d^-)$	$(\widetilde{H}_d^0 \quad \widetilde{H}_d^-)$	$(\mathbf{1}, \mathbf{2}, -\frac{1}{2})$

where $\widetilde{u}_L,\ u_L$ $(T_3 = +1/2)$, and $\widetilde{d}_L,\ d_L$ $(T_3 = -1/2)$ are $SU(3)_C$ color triplets with hypercharge $Y = 1/6$. The other quark superfield $\hat{\overline{U}}$ $(\hat{\overline{D}})$ contains two "right handed" $SU(2)_L$ singlets $\widetilde{u}_R^*, u_R^\dagger$ $(\widetilde{d}_R^*, d_R^\dagger)$ with hypercharge $Y = -2/3$ $(Y = 1/3)$. They are $SU(3)_C$ color triplets. The leptonic superfield $\hat{L}$ is constructed out of two $SU(2)_L$ isospin doublets

$$\begin{pmatrix} \widetilde{\nu}_L \\ \widetilde{e}_L \end{pmatrix}, \quad \begin{pmatrix} \nu \\ e \end{pmatrix}_L, \tag{3.52}$$

where $\widetilde{\nu}_L,\ \nu_L$ $(T_3 = +1/2)$, and $\widetilde{e}_L,\ e_L$ $(T_3 = -1/2)$ are $SU(3)_C$ color singlets with hypercharge $Y = 1/6$. The other leptonic superfield $\hat{\overline{E}}$ contains two "right handed" $SU(2)_L$ singlets $\widetilde{e}_R^*, e_R^\dagger$ with hypercharge $Y = 1$. They are $SU(3)_C$ color singlets.

We relate these chiral superfields to the ones used in the general SUSY description in the previous section:

- superfield $\Phi_i \in \left\{\hat{Q},\ \hat{\overline{U}},\ \hat{\overline{D}},\ \hat{L},\ \hat{\overline{E}}\ +\ \text{other families}\right\}$;
- spinor $\psi_i \in \left\{ \begin{pmatrix} u \\ d \end{pmatrix}_L,\ u_R,\ d_R,\ \begin{pmatrix} \nu \\ e \end{pmatrix}_L,\ e_R +\ \text{other families} \right\}$;
- complex scalar $\phi_i \in \left\{ \begin{pmatrix} \widetilde{u}_L \\ \widetilde{d}_L \end{pmatrix},\ \widetilde{u}_R,\ \widetilde{d}_L,\ \begin{pmatrix} \widetilde{\nu}_L \\ \widetilde{e}_L \end{pmatrix},\ \widetilde{e}_R +\ \text{other families} \right\}$.

EWK symmetry breaking sector

Table 3.2 shows the fields of the Higgs sector of MSSM. Unlike in the SM we need two Higgs doublets in MSSM. There are two main reasons for that. The first one is the required **anomaly cancellations**[14]. The condition to cancel the triangle

gauge anomalies (in the normalization where $Q = T_3 + Y$) is $\mathrm{Tr}[T_3^2 Y] = 0$. The trace runs over all left handed Weyl spinor fields present in the theory. In the Standard Model, this condition is precisely fulfilled by the fermions and quarks. However in the MSSM, the superpartner of the SM scalar Higgs doublet is a left handed doublet (the higgsino) with $|Y| = 1/2$. Therefore it contributes to the trace shown above and breaks the anomaly free theory condition. This problem is solved if we introduce an additional[6] Higgs doublet, with an opposite hypercharge (see Tab.3.2). This way their contributions will cancel out. In the Tab.3.2 these Higgs doublets are denoted as H_d and H_u respectively. They contain H_u^+, H_d^0 ($T_3 = 1/2$) and H_u^0, H_d^- ($T_3 = -1/2$). The upper indices of H show their electric charges Q. The superpartners of H_d and H_u are the $SU(2)_L$ doublets denoted $\widetilde{H}_u$ and $\widetilde{H}_d$. The superfield containing H_u and $\tilde{H}_u$ doublets is denoted $\hat{H}_u$. Similarly for $\hat{H}_d$.

To draw the analogy between the chiral superfields introduced in the previous section, we have:

- superfield $\Phi_i \in \left\{\hat{H}_u,\ \hat{H}_d\right\}$;
- spinor $\psi_i \in \left\{\begin{pmatrix}\widetilde{H}_u^+\\ \widetilde{H}_u^0\end{pmatrix},\ \begin{pmatrix}\widetilde{H}_d^0\\ \widetilde{H}_d^-\end{pmatrix}\right\}$;
- complex scalar $\phi_i \in \left\{\begin{pmatrix}H_u^+\\ H_u^0\end{pmatrix},\ \begin{pmatrix}H_d^0\\ H_d^-\end{pmatrix}\right\}$

Gauge sector

Tab.(3.3) shows the SM gauge bosons and their MSSM fermionic superpartners. The superpartner of the $SU(3)_C$ octet, spin 1 gluon (g) is a spin 1/2, $SU(3)_C$ octet, the gluino ($\tilde{g}$). The electroweak gauge fields b_μ^1, b_μ^2, b_μ^3 and A_μ have their fermionic superpartners the $\widetilde{W}^+, \widetilde{W}^0, \widetilde{W}^-$ and $\widetilde{B}^0$, called *winos* and the *bino*.

[6]There is another reason for the need of two Higgs doublets. It will be shown that only the Higgs doublet with $Y = 1/2$ has the proper Yukawa coupling to give mass to u, c and t quarks and only the $Y = -1/2$ doublet can give masses to the d, s and b quarks in SUSY.

Table 3.3
Gauge supermultiplets in MSSM.

Names	spin 1/2	spin 1	$SU(3)_C$, $SU(2)_L$, $U(1)_Y$
gluino, gluon	$\widetilde{g}$	g	(**8**, **1** , 0)
winos, b^a fields	$\widetilde{W}^{\pm}$ $\widetilde{W}^0$	b^1, b^2, b^3	(**1**, **3** , 0)
bino, B boson	$\widetilde{B}^0$	A	(**1**, **1** , 0)

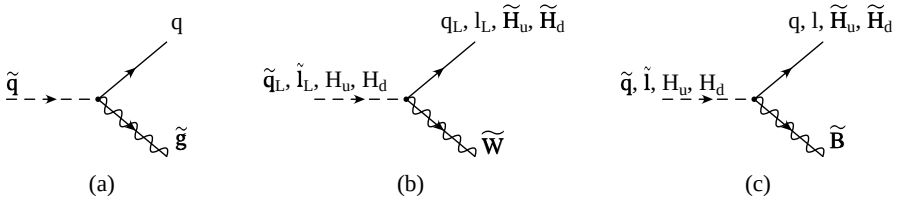

Figure 3.4. Gaugino vertices in MSSM: Couplings of the gluino, wino, and bino to various MSSM scalars and fermions.

3.2.2. The Lagrangian of the MSSM

Having defined the superfields entering the MSSM we can identify the MSSM superpotential (3.40):

$$f_{\rm MSSM} = \hat{\overline{U}}\mathbf{y_u}\hat{Q}\hat{H}_u - \hat{\overline{D}}\mathbf{y_d}\hat{Q}\hat{H}_d - \hat{\overline{E}}\mathbf{y_e}\hat{L}\hat{H}_d + \mu\hat{H}_u\hat{H}_d\,, \tag{3.53}$$

where the $\mathbf{y_u}, \mathbf{y_d}, \mathbf{y_e}$ are the Yukawa couplings[7]. The complete MSSM Lagrangian is built by plugging the superfields from Tabs. 3.1, Tab. 3.2, and 3.3 into (3.50) and is given in [28]. Fig. 3.4 presents various[8] MSSM vertices of couplings of gauginos to scalars and fermions. (These vertices all come from the general vertex shown on Fig. 3.2g.)

[7]Two examples of summation details: $\hat{\overline{U}}\mathbf{y_u}\hat{Q}\hat{H}_u = \hat{\overline{U}}^i_a\,(\mathbf{y_u})_i{}^j\,\hat{Q}^a_{j\alpha}\,(\hat{H}_u)_\beta\epsilon^{\alpha\beta}$, or, $\mu\hat{H}_u\hat{H}_d = \mu(\hat{H}_u)_\alpha(\hat{H}_d)_\beta\epsilon^{\alpha\beta}$, where $i,j = 1,2,3$ are the family indices, $a = 1,2,3$ is the $SU(3)_C$ color index for the triplet and $\alpha,\beta = 1,2$ are the isospin $SU(2)_L$ weak indices.

[8]The most relevant vertices to our search for the stop quark.

3.2.3. SUSY R-parity

As seen in Sec. 3.1.1, the SUSY extended Poincaré algebra also included an U(1) internal symmetry generator, R. The corresponding symmetry is called R-parity and the corresponding quantum number is denoted by R. To every MSSM particle we can define its R parity by the relation

$$R \equiv (-1)^{3B+L+2j}, \tag{3.54}$$

where B is the baryon number, L is the lepton number and j is the spin of the particle. SM particles have $R = +1$ and their superpartners have $R = -1$. So far, throughout the construction of the superpotential we always assumed that the R quantum number was conserved. This was an *ad hoc* assumption. One can imagine interaction terms in MSSM, where the R-parity is not conserved. The MSSM superpotential considered in the previous section is certainly not the most general one. It could contain gauge and SUSY invariant terms like

$$f_{\mathrm{R-breaking}} = \frac{1}{2}\hat{\bar{E}}\lambda\hat{L}\hat{L} + \hat{\bar{D}}\lambda'\hat{L}\hat{Q} + \mu'\hat{H}\hat{L} + \lambda''\hat{\bar{D}}\hat{\bar{D}}\hat{\bar{U}}.$$

It can be shown, that the first three terms can lead to processes that violate the lepton number conservation and that the last term allows the violation of the baryon number conservation. If R-parity was not conserved, we would observe effects like *f.e.* rapid proton decay.

For our purposes we assume that R-parity is conserved. This assumption has some important experimental consequences:

- The "lightest supersymmetric particle" (LSP) is unable to decay to nonsupersymmetric particles and is therefore stable.

- Every SUSY particle must decay into a final state containing an odd number of LSPs.

- In colliders, supersymmetric particles must be created in pairs.

3.2.4. SUSY Breaking in the MSSM

Plugging the MSSM superfields into the soft susy breaking terms given in section (3.1.7), we get the following most general gauge invariant and R-parity conserving soft SUSY breaking terms[21]:

$$\begin{aligned}
\mathcal{L}_{\text{soft}} \;=\; & -\frac{1}{2}\left(M_3\widetilde{g}\widetilde{g} + M_2\widetilde{W}\widetilde{W} + M_1\widetilde{B}\widetilde{B}\right) + h.c. \\
& - \left(\widetilde{\overline{u}}\,\mathbf{a_u}\,\widetilde{Q}H_u - \widetilde{\overline{d}}\,\mathbf{a_d}\,\widetilde{Q}H_d - \widetilde{\overline{e}}\,\mathbf{a_e}\,\widetilde{Q}H_d\right) + h.c. \\
& - \widetilde{Q}^{\dagger}\,\mathbf{m_Q^2}\,\widetilde{Q} - \widetilde{L}^{\dagger}\,\mathbf{m_L^2}\,\widetilde{L} - \widetilde{\overline{u}}\,\mathbf{m_{\overline{u}}^2}\,\widetilde{\overline{u}}^{\dagger} - \widetilde{\overline{d}}\,\mathbf{m_{\overline{d}}^2}\,\widetilde{\overline{d}}^{\dagger} - \widetilde{\overline{e}}\,\mathbf{m_{\overline{e}}^2}\,\widetilde{\overline{e}}^{\dagger} \\
& - m_{H_u}^2 H_u^* H_u - m_{H_d}^2 H_d^* H_d - (bH_uH_d + h.c.)\,. \qquad (3.55)
\end{aligned}$$

The notation is straightforward, but for completeness we list the entering field components explicitly in Appendix E. The M_i are the masses of gauginos (gluino, winos, bino). The trilinear couplings $\mathbf{a_u}$, $\mathbf{a_d}$, $\mathbf{a_e}$ are 3x3 matrices in the family space. Their dimension is the first power of mass. The $\mathbf{m^2}$'s are the squarks and sleptons masses. They are also 3x3 matrices in the family space and have the dimension of the mass squared. The $m_{H_u}^2$, $m_{H_d}^2$ are 2x2 isospin matrices and they have mass squared dimension. Similarly for the b matrix. *Notice*: that the 2 in the exponent of the mass parameters is the part of the name of the parameter, and it does not mean the second power. It turns out that by (3.55), we just introduced more than a hundred new parameters which do not have an analog in the Standard Model.

The number of parameters can be reduced by imposing certain experimental constraints, such as limits on flavor-changing neutral currents or CP violating terms [21]. We can also naturally assume that the SUSY is flavor blind which translates into diagonal mass matrices in the family space:

$$\mathbf{m_Q^2} = m_Q^2\mathbf{1}; \quad \mathbf{m_{\overline{u}}^2} = m_{\overline{u}}^2\mathbf{1}; \quad \mathbf{m_{\overline{d}}^2} = m_{\overline{d}}^2\mathbf{1}; \quad \mathbf{m_L^2} = m_L^2\mathbf{1}; \quad \mathbf{m_{\overline{e}}^2} = m_{\overline{e}}^2\mathbf{1}. \qquad (3.56)$$

We can make a further assumption, which will ensure that only the third family leptons (which have the largest Yukawa couplings) will get large soft terms by requiring:

$$\mathbf{a_u} = A_{u0}\,\mathbf{y_u}; \qquad \mathbf{a_d} = A_{d0}\,\mathbf{y_d}; \qquad \mathbf{a_e} = A_{e0}\,\mathbf{y_e}. \qquad (3.57)$$

3.2.5. Origin of the Soft Terms

One of the consequences of introducing soft breaking terms is that MSSM becomes an effective theory. It means that MSSM is not a fundamental theory and has to be extended in order to explain the origin of the soft terms.

Physicists introduced a sector, called "the hidden sector", where SUSY breaking happens and which has a very small coupling to the "visible sector" of the chiral superfields. There are few models describing how the hidden sector tells the visible sector about the fact that SUSY is broken. We focus on the **gravity mediated supersymmetry breaking** (GMSB) mechanism, whose basic idea is that the hidden sector communicates to the visible sector through *gravitational interaction*. Introducing gravity to the supersymmetric theories means, that the parameter ξ in the SUSY transformations (see Eqs.(3.17)) is no longer a global constant but is space-time dependent. Such a theory is called supergravity (SUGRA). Interaction propagates via a graviton (a spin 2 object) and its superpartner, the gravitino. Their couplings are proportional to $1/M_{Pl}$ and are very weak. For details see [21]. The most important result of SUGRA is that it can assume a "minimal " form of the Lagrangian (then we call it mSUGRA), where all the soft susy breaking terms ($\mathcal{L}_{soft}$) can be expressed in terms of **four** parameters:

$$m_{1/2} = f\frac{\langle F_S\rangle}{M_{Pl}}; \qquad m_0^2 = x\frac{|\langle F_S\rangle|^2}{M_{Pl}^2}; \qquad A_0 = \alpha\frac{\langle F_S\rangle}{M_{Pl}}; \qquad B_0 = \beta\frac{\langle F_S\rangle}{M_{Pl}}, \tag{3.58}$$

where F_S is the F-term of a chiral superfield $\hat{S}$ representing the hidden sector and $f,\ x,\ \alpha,\ \beta$ are free parameters. $\langle F_S\rangle$ is usually assumed to be around 10^{10} GeV [21]. By using Eqs.(3.56) and (3.57), the soft SUSY couplings of (3.55) can be written as:

$$M_3 = M_2 = M_1 = m_{1/2}; \tag{3.59}$$

$$\mathbf{m_Q^2} = \mathbf{m_{\bar{u}}^2} = \mathbf{m_{\bar{d}}^2} = \mathbf{m_L^2} = \mathbf{m_{\bar{e}}^2} = m_0^2\,\mathbf{1}; \quad m_{H_u}^2 = m_{H_d}^2 = m_0^2; \tag{3.60}$$

$$\mathbf{a_u} = A_0\mathbf{y_u}; \qquad \mathbf{a_d} = A_0\mathbf{y_d}; \qquad \mathbf{a_e} = A_0\mathbf{y_e}; \tag{3.61}$$

$$b = B_0\mu. \tag{3.62}$$

The renormalization group equations (RGE) give the values of the soft parameters at the electroweak scale allowing us to describe the whole mSUGRA spectrum in terms of only five parameters (in addition to the SM ones):

$$m_{1/2},\ m_0^2,\ A_0,\ B_0,\ \mu \tag{3.63}$$

Without loss of generality, some restrictions on the Higgs doublets entering MSSM can be imposed. It can be shown[21] that the charged components of the two higgs doublets do not receive VEV. Using this and collecting all the scalar neutral higgs terms (excluding the interaction terms) in the superpotential, we obtain[21]:

$$\begin{aligned}\mathcal{L}_{Higgs}(H_u^0, H_d^0) &= (|\mu|^2 + m_{H_u}^2)|H_u^0|^2 + (|\mu|^2 + m_{H_d}^2)|H_d^0|^2 - (b\, H_u^0 H_d^0 + c.c.) \\ &\quad + \frac{1}{8}(g^2 + g'^2)(|H_u^0|^2 - |H_d^0|^2)^2. \end{aligned} \tag{3.64}$$

This potential will have a minimum when $\partial\mathcal{L}_{Higgs}/\partial H_u^0 = \partial\mathcal{L}_{Higgs}/\partial {H_d}^0 = 0$, which translates into

$$b = \frac{1}{2}\left[\left(m_{H_d}^2 - m_{H_u}^2\right)\tan(2\beta) + M_Z^2 \sin(2\beta)\right]; \tag{3.65}$$

$$|\mu^2| = \frac{m_{H_u}^2 \sin^2\beta - m_{H_d}^2 \cos^2\beta}{\cos(2\beta)} - \frac{1}{2}M_Z^2, \tag{3.66}$$

where

$$\tan\beta \equiv \frac{\langle H_u^0 \rangle}{\langle H_d^0 \rangle}. \tag{3.67}$$

These VEV's are then related to the Z^0 boson mass similarly as in the SM case:

$$M_Z^2 = v^2 \frac{g^2 + g'^2}{2} \sim (91\mathrm{GeV}/c^2)^2, \quad \text{where} \quad v^2 \equiv \langle H_u^0 \rangle^2 + \langle H_d^0 \rangle^2. \tag{3.68}$$

Since $b = B_0\mu$, (3.65) and (3.66) allow us to replace b, and $|\mu^2|$ with $\tan\beta$, $sign(\mu)$ leaving the following five free mSUGRA parameters:

$$m_{1/2},\ m_0^2,\ A_0, \tan\beta,\ sign(\mu), \tag{3.69}$$

the common fermion and common scalar mass, the trilinear coupling, the ratio of the two Higgs's VEV's , and the $sign(\mu)$ respectively.

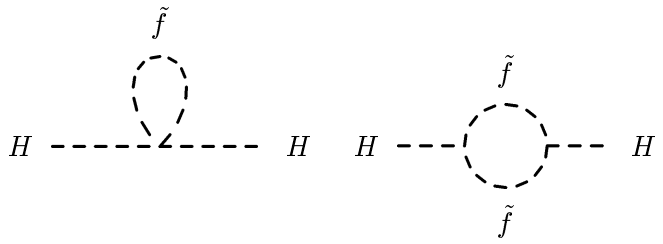

Figure 3.5. Sfermion loop corrections to the Higgs mass.

3.2.6. Cancellation of the Quadratic Divergences

In section (2.3.2), we showed the quadratically divergent Standard Model one loop Feynman diagrams contributing to the Higgs mass. For simplicity we focus on the fermion loop diagram shown on Fig. 2.1 when the fermion is the top quark.

In MSSM in the superpotential (3.53) we had a term $\hat{\overline{U}}\mathbf{y_u}\hat{Q}\hat{H}_u$. In the case of the third family its contribution to the interaction Lagrangian is [21]:

$$\mathcal{L}_{inter}(\tilde{t}, H_u) = \frac{1}{2}\tilde{\lambda}_f H_u^2 \left(\left|\tilde{t}_L\right|^2 + \left|\tilde{t}_R\right|^2\right) + v\tilde{\lambda}_f H_u \left(\left|\tilde{t}_L\right|^2 + \left|\tilde{t}_R\right|^2\right) + \left(\frac{\lambda_f}{\sqrt{2}} A_f H_u \tilde{t}_L \tilde{t}_R^* + h.c.\right) \tag{3.70}$$

This gives rise to diagrams shown on Fig.(3.5). Their contributions to the Higgs mass corrections [15] yield the following **quadratically** divergent term when k gets large:

$$-\tilde{\lambda}_f N(\tilde{t}) \int \frac{d^4k}{(2\pi)^4} \left[\frac{1}{k^2 - m_{\tilde{t}_L}^2} + \frac{1}{k^2 - m_{\tilde{t}_R}^2}\right], \tag{3.71}$$

where $N(\tilde{t}) = 3$. Denoting the high k cut-off by Λ, the total one loop corrections (2.22) due to top and stop quark to the Higgs mass can be written as [29]:

$$m_H^2 \sim m_0^2 + \lambda_t^2(\Lambda^2 + m_t^2) + \lambda_{\tilde{t}}(\Lambda^2 + m_{\tilde{t}_L}^2 + m_{\tilde{t}_R}^2). \tag{3.72}$$

Therefore, by choosing $\lambda_{\tilde{t}} = -\lambda_t^2$ we can eliminate the quadratic divergences and this **cancellation does not require equal stop and top masses**! Similarly all other quadratically divergent SM diagrams will receive an opposite sign MSSM cancelling diagram.

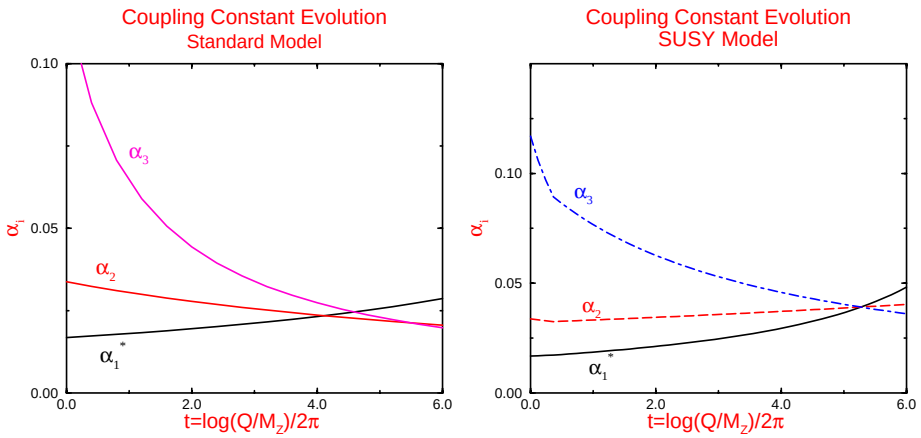

Figure 3.6. Evolution of the gauge coupling constants in the Standard Model and MSSM. $\alpha_1^* \equiv 5/3\alpha_1$ is the GUT gauge coupling. Adapted from [30].

3.2.7. Unification of the Coupling Constants

Besides the cancellation of the quadratic divergences, SUSY has another advantage. It unifies the SM gauge coupling constants at some energy scale $M_U \sim 0.01 M_{Pl}$. The unification of coupling constants is an important aspect of candidates (like the Grand Unified Theory (GUT)) for being the ultimate theory, because it reduces the number of free parameters entering the theory. A "theory of everything" should have very low number of free parameters, preferably none or one. Fig.(3.6) shows the energy dependence of the three gauge couplings in the SM and MSSM framework respectively. In MSSM all three coupling constants meet at a common energy scale $M_U \sim 10^{16}$ GeV$/c^2$.

4. MSSM Particles and Their Properties

The Minimal Supersymmetric Standard Model is a very good candidate for a theory beyond the Standard Model. As described in Sec. 3.2.6, it naturally solves some of the Higgs sector related problems of SM. The MSSM, however, gives no prediction of the values of physical masses of its particles. We will thus treat the unknown masses as free parameters in our search. Despite the limited knowledge of the SUSY breaking mechanism details, some useful relations within the EWK mass spectrum of MSSM can be deduced, and measurable physical effects can be predicted. These are the subject of the following few sections.

4.1. Neutralinos

4.1.1. Masses of Neutralinos

The neutral SM bosons and scalars have fermionic superpartners, the bino, the neutral wino, and the neutral higgsinos ($\widetilde{B}^0$, $\widetilde{W}^0$, $\widetilde{H}_d^0$, $\widetilde{H}_u^0$, see Tabs.3.2 and 3.3). These electroweak eigenstates mix to form mass eigenstates, the observable neutralinos ($\tilde{\chi}_i^0,\ i = 1, \ldots, 4$). Their masses in general depend on four parameters[21], the bino mass (M_1), the wino mass (M_2), the ratio of the VEV's of the two Higgs doublets ($\tan\beta$), and the coupling of the Higgs superfields in the MSSM Lagrangian (μ). We label the neutralinos, so that $\tilde{\chi}_1^0$ is the lightest mass eigenstate. If no light sleptons exist, then $\tilde{\chi}_1^0$ will be the lightest SUSY particle (LSP) and in that case it will be a good candidate for the cosmological dark matter. In this analysis we consider the lightest neutralino to be the LSP, therefore every SUSY particle will decay into it.

4.1.2. Decays of Neutralinos

Fig. 3.4(c) shows the vertex governing the interactions of neutralinos, enabling a variety of possible decays. First, the two body decays into lighter neutralinos, supersymmetric fermions, or lighter charginos would dominate if kinematically allowed. If not, the three-body diagrams (via off-shell virtual particles) become important.

$$\tilde{\chi}_i^0 \to Z^0 \tilde{\chi}_j^0, \quad h^0 \tilde{\chi}_j^0, \quad l\tilde{l}, \quad \nu\tilde{\nu}, \quad q\tilde{q}, \quad W\tilde{\chi}_j \tag{4.1}$$

$$\tilde{\chi}_i^0 \to f\bar{f}\tilde{\chi}_j^0, \quad \tilde{\chi}_i^0 \to ff'\tilde{\chi}_j, \tag{4.2}$$

where $i, j = 1, \ldots, 4$ and f and f' are fermionic particles from the same EWK doublet and $\widetilde{\chi}_j$ are the charginos (see next section). For more details and branching ratios see [28]. For us only the $\tilde{\chi}_1^0$ is relevant, which does not decay any further.

4.2. Charginos

4.2.1. Masses of Charginos

Similarly as for neutralinos, the charged weak eigenstates ($\widetilde{W}^+$, $\widetilde{W}^-$, $\widetilde{H}_u^+$, $\widetilde{H}_d^-$ listed in Tab.3.2 and 3.3) are not the physical mass eigenstates either. We label $\tilde{\chi}_1^\pm$ ($\tilde{\chi}_2^\pm$) the lighter (heavier) observable mass eigenstate. Its mass dependence on the SUSY parameters can be found in [21]. If one takes into account the Grand Unification (Sec. 3.2.7), some relations between the lighter chargino and the lightest neutralino masses exist[21].

- If $|\mu| > |M_2| \geq M_{Z^0}$ then $m_{\tilde{\chi}_1^\pm} \simeq 2m_{\tilde{\chi}_1^0}$
- If $|\mu| < |M_1|$ then $m_{\tilde{\chi}_1^\pm} \simeq m_{\tilde{\chi}_1^0} \simeq |\mu|$
- If $|\mu| \simeq |M_2|$ then the mass states are strongly mixed and the situation is more complicated.

4.2.2. Decays of Charginos

The interactions of charginos follow from vertices showed in Fig. 3.4(b) and 3.4(c). At first, the two body decays into lighter neutralinos, charginos or supersymmetric fermions would be preferred if kinematically possible. If not, the three body decays will dominate.

$$\tilde{\chi}_i^{\pm} \to W^{\pm}\tilde{\chi}_j^0, \quad Z^0\tilde{\chi}_1^{\pm}, \quad h^0\tilde{\chi}_1, \quad l\tilde{\nu}, \quad \nu\tilde{l}, \quad q\tilde{q}' \tag{4.3}$$

$$\tilde{\chi}_i^{\pm} \to ff'\tilde{\chi}_j^0, \quad \text{and} \quad \tilde{\chi}_2^{\pm} \to ff'\tilde{\chi}_1^{\pm}, \tag{4.4}$$

where $i, j = 1, 2$ and f and f' are fermions from the same $SU(2)_L$ doublet. For us the most relevant chargino is the lighter $\tilde{\chi}_1^{\pm}$. It decays to sneutrinos, since the other 2-body decays are kinematically not accessible.

4.3. The Stop Quark

4.3.1. The Stop Mass

The stop quark related terms of the SUSY Lagrangian are built in terms of weak eigenstates, $\tilde{t}_L$ and $\tilde{t}_R$. They mix to form the mass eigenstates $\tilde{t}_1$ and $\tilde{t}_2$. In order to find their physical masses we collect all the quadratic in stop terms in the SUSY Lagrangian. (1) the soft susy breaking terms (3.55) contribute with unmixed terms proportional to $m^2_{\tilde{t}_L}$ and $m^2_{\tilde{t}_R}$; (2) the $\left|\partial f/\partial \tilde{t}_R\right|^2$ and $\left|\partial f/\partial \tilde{t}_L\right|^2$ part of the interaction Lagrangian (3.45) contribute with unmixed terms proportional to m_t^2, where f is the MSSM superpotential; (3) the (squark)^2(Higgs)^2 parts of the D-term Lagrangian (3.49) contribute with unmixed terms proportional to $(T_3^{\tilde{t}} - Q_{\rm EM}^{\tilde{t}} \sin^2\theta_W)\cos 2\beta\, m_Z^2$, where $T_3^{\tilde{t}}$ and $Q_{\rm EM}^{\tilde{t}}$ are the third component of the weak isospin and the electric charge of the stops respectively; (4) the F-terms of the scalar potential contribute with mixed terms proportional to μy_t; (5) the soft trilinear terms (3.55) contribute with mixed stop terms proportional to a_t. By introducing $\Psi^T \equiv (\tilde{t}_L, \tilde{t}_R)$ and denoting the mixing

matrix $\mathbf{M^2_{stop}}$ we can summarize the above mentioned quadratic terms in a compact form

$$\mathcal{L}_{stop} = -\Psi^\dagger \mathbf{M^2_{stop}} \Psi, \tag{4.5}$$

where the mass matrix is given by[31][1]

$$\mathbf{M^2_{stop}} = \begin{pmatrix} m^2_{\tilde{t}_L} + m^2_t + (\frac{1}{2} - \frac{2}{3}\sin^2\theta_W)\cos 2\beta\, m^2_Z & m_t(A_t - \mu\cot\beta) \\ m_t(A_t - \mu\cot\beta) & m^2_{\tilde{t}_R} + m^2_t + \frac{2}{3}\sin^2\theta_W \cos 2\beta\, m^2_Z \end{pmatrix} \tag{4.6}$$

where $m^2_{\tilde{t}_L}$, $m^2_{\tilde{t}_R}$ are the soft SUSY breaking masses, A_t is the trilinear stop-Higgs coupling, μ is the Higgs superpotential coupling, $\tan\beta$ is the ratio of the VEV's of the two Higgs doublets and the rest are standard notations from the SM. We note that identical mass matrices can be extracted for superpartners ($\tilde{q}$) of all flavor quarks (q) by substituting $t \to q$ and $\tilde{t} \to \tilde{q}$ in (4.6). The mixing matrix (4.6) reveals, that the left-right mixing is negligible for other than the third family squarks, but can be substantial for the stop and sbottom quarks.

For our experimental stop quark search, we want to know what range of stop masses can be expected, particularly, if light stop masses can be expected. If for example we work in the framework of mSUGRA, first the parameters of (4.6) are calculated at the EWK scale[2] and then (4.6) is diagonalized. Given the large top quark mass, the $\widetilde{t}_L$ and $\widetilde{t}_R$ mixing leads to significant mass splitting between the two physical mass states ($\widetilde{t}_1$, $\widetilde{t}_2$) allowing us to consider $\widetilde{t}_1$ as being the lightest squark.

4.3.2. Scalar Top Quark Production

In our search for the stop quark, we assume that R-parity (see Sec. 3.2.3) is conserved. This then implies that the stop quarks are pair produced, because in the initial state (protons and antiprotons) there are no SUSY particles. Since there are gluon-scalar-scalar and gluon-gluon-scalar-scalar vertices in the SUSY Lagrangian

[1] In order to get exactly the form shown in [31], one has to rewrite $a_t = A_t y_t$, substitute for y_t the usual $\frac{gm_t}{2m_W \sin\beta}$ and use $m_W = g\frac{v}{2}$ relation.

[2] It is done by running the renormalization group evolution of the parameters from the GUT scale down to the EWK scale.

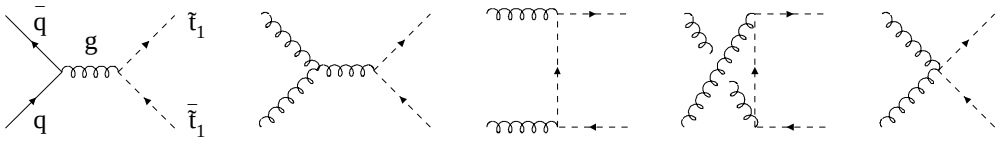

Figure 4.1. The lowest order Feynman diagrams showing quark–antiquark annihilation and gluon fusion for the production of pairs of stop particles.

(see terms in Fig. 3.2), we can deduce the Feynman diagrams contributing to the stop pair production[3]. The lowest order such diagrams[4] are shown in Fig. 4.1. The $\tilde{t}_1\bar{\tilde{t}}_1$ production cross sections[5] via quark-antiquark annihilation and the gluon-gluon fusion processes are given by[32]:

$$\hat{\sigma}_{LO}[q\bar{q} \to \tilde{t}_1\bar{\tilde{t}}_1] = \frac{\alpha_s^2\pi}{s}\frac{2}{27}\beta_1^3 \tag{4.7}$$

$$\begin{aligned}\hat{\sigma}_{LO}[gg \to \tilde{t}_1\bar{\tilde{t}}_1] &= \frac{\alpha_s^2\pi}{s}\beta_1\left(\frac{5}{48}+\frac{31m_{\tilde{t}_1}^2}{24s}\right) \\ &+ \frac{\alpha_s^2\pi}{s}\left(\frac{2m_{\tilde{t}_1}^2}{3s}+\frac{m_{\tilde{t}_1}^4}{6s^2}\right)\log\left(\frac{1-\beta_1}{1+\beta_1}\right)\end{aligned} \tag{4.8}$$

where $\sqrt{s}$ is the invariant center-of-mass energy of the collision and $\beta_1 = \sqrt{1-4m_{\tilde{t}_1}^2/s}$.

By looking at the (4.8) production cross section, naively one would conclude that for $m_{\tilde{t}} \ll \sqrt{s}$ the $q\bar{q}$ annihilation contributes with a weight equal to the gg fusion and that the cross section is approximately $m_{\tilde{t}}$ independent. It turns out to be more complicated, since we do not collide elementary partons like quarks or gluons, but we collide protons and antiprotons, which have complicated, internal structure. In order to properly calculate the stop production cross section from $p\bar{p}$ collisions, their parton distribution functions must be properly taking into account. At lower values of Q^2

[3]The production of $\tilde{t}_1\bar{\tilde{t}}_2$ is suppressed, because it can be produced with higher order diagrams only.
[4]There are other diagrams for squark production which are based on the exchange of a gluino or a neutralino. However their contributions are very small and we will not discuss them here.
[5]Same formulae hold for the $\tilde{t}_2\bar{\tilde{t}}_2$ productions.

(regions of lower stop masses)[6], the density of soft gluons in protons or antiprotons is very high therefore the cross section grows with falling stop mass and gluon-gluon fusion dominates. Whereas at higher Q^2 (higher stop mass regions), the density of valence quarks dominates, but it falls exponentially as the mass of the stops we try to produce, grows[7]. Therefore the stop production cross section falls exponentially with increasing stop mass. This can be seen in Fig. 4.2, which shows the total production cross section of $\tilde{t}_1\bar{\tilde{t}}_1$ (right axis) as a function of the stop mass (upper axis)[8]. The stop production cross section shown on Fig. 4.1 allows us to make a simple estimate of the possible stop mass reach in our search. For signal detection, we need at least 10 events left after all the selection cuts and all appropriate efficiencies are applied. This means that we need at least several hundred, to a thousand stop pairs to be produced in collisions. Given that the total amount of data available for analysis is 107 pb^{-1}, this means that we can reach to stop masses with a production cross section of order 10 pb. The largest stop mass in reach of our experiment, therefore is around 120 GeV/c^2 . This will have a strong influence on the possible stop decay scenarios discussed in the next section.

4.3.3. Lepton Leading Stop Decays

The possibility to experimentally observe a stop quark very much depends on its production rate and the kinematics of its decays. The production has been discussed in the previous section. Feynman vertices shown in Fig. 3.4 indicate the modes through which stop quarks can decay. The mass spectrum of MSSM then dictates the actually allowed stop decays. These modes then give rise to a variety of signatures for which we can search in the data.

---

[6]The Q characterizes the amount of transfered energy during the collisions. In the stop pair production it is approximately proportional to $2m_{\tilde{t}}$

[7]One needs higher x to produce heavier stops at constant $\sqrt{s}$. Variable x is the fraction of the proton's momentum the valance quark has.

[8]Similarly for the $\tilde{t}_2\bar{\tilde{t}}_2$ but with the left and lower axes

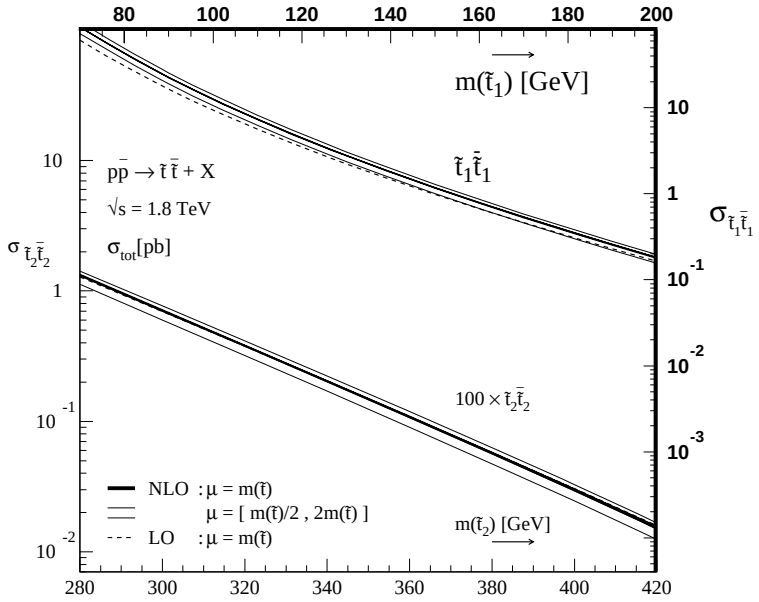

Figure 4.2. The total cross section for the production of stop pairs $\tilde{t}_1\bar{\tilde{t}}_1$ (right axis) at the Tevatron as a function of the stop masses (upper horizontal axis). The line thick-ness for the NLO curves represents the simultaneous variation of the gluino mass between 200 and 800 GeV and the variation of the mixing parameter $\sin(2\theta_{\tilde{t}})$ over its full range. μ is the renormalization scale parameter. CTEQ_4L structure function has been used. See [32]. For comparison we also show the $100 \times \sigma(\tilde{t}_2\bar{\tilde{t}}_2)$ (left axis) as the function of $m_{\tilde{t}_2}$ (lower horizontal axis).

Decays governed by strong interaction:

Due to the strong-ness of QCD, the two body decays to the top quark would dominate ($\widetilde{t} \to t\widetilde{g}$ governed by Fig. 3.4(a) or $\widetilde{t} \to t\tilde{\chi}_1^0$ governed by Fig. 3.4(c)). From the production cross section we estimated that our possible reach will be around $m_{\tilde{t}} = 120$ GeV/c^2 , which means these decays are kinematically not accessible (since $m_t = 175$ GeV/c^2)[9].

Decays governed by weak interaction:

With the analogy of the top quark decay $t \to bW^+$, the first EWK decays of the stop quark which come in mind are the $\widetilde{t} \to \widetilde{b}W^+$ and $\widetilde{t} \to b\widetilde{\chi}_1^+$. Indeed, these decays are

[9]Note that the same vertices could be responsible for the opposite process $t \to \tilde{t}\tilde{g}$. However, already existing strong experimental limits on the gluino mass close this possibility.

possible as indicated by the vertex shown on Fig. 3.4(b). The stop decays to squarks are not accessible since the stop is the lightest squark. If the stop decay to chargino is kinematically allowed, it dominates. However, given the strong existing limits on the $\widetilde{\chi}_1^+$ chargino mass[33] of 100 GeV/c^2 , this decay mode leaves CDF a very small window of opportunity to study the stop quark [10]. When the above 2-body decay mode is not allowed, the 3-body decay mode $\widetilde{t} \to bW^+\widetilde{\chi}_1^0$ would be the dominant decay if kinematically possible. But the existing mass limit on the lightest neutralino[34] forbids the light stop to decay to an on-shell[11] W and a neutralino. This then leads us to the 3-body decay into neutral (or charged) sleptons via a virtual chargino. The charged sleptons are considered to be heavy[35], but $\boxed{\tilde{t} \to\ b\widetilde{\nu}l}$ via $\tilde{t} \to b\widetilde{\chi}_1^{+*}$ which then decays $\widetilde{\chi}_1^{+*} \to l^+\widetilde{\nu}$ is still open if kinematically allowed. Given the existing mass limit (of $m_{\tilde{\nu}} \geq 45$ GeV/c^2) on the sneutrinos[13], we take this great opportunity to explore the stop quark. This is the subject of this thesis. The only other possible stop decay would be $\widetilde{t} \to c\widetilde{\chi}_1^0$. It is a flavor-changing decay. It would proceed via a higher order loop diagram where $\tilde{t} \to b\widetilde{\chi}_1^{+*}$ and the loop is closed by a virtual W^* exchange ($\widetilde{\chi}_1^{+*} \to W^{+*}\widetilde{\chi}_1^0$, $b \to W^{+*}c$), therefore it is highly suppressed[36].

[10] We remind here that our search is conducted through a dilepton signature. If the stop produced chargino further decays to a neutralino and W boson, which then decays leptonically, we encounter a substantial signal efficiency problem due to the low, 1/9 branching ratio of the leptonic W decay. This assumed a high wino content of the chargino. If the chargino has a high higgsino content, its decays to the third family leptons could be substantially increased opening a possibility to search for stop in the "di-τ" channel. Even if this above mentioned branching ratio suppression is somehow degraded, we still have a problem of the stop mass being too close to the chargino mass leaving very little room for the b-jet to be reconstructed and detected. The only way to improve or make possible the search considering a real chargino would be to consider higher stop masses, which of course brings along the rapid decrease of the production cross section and the Run 1 collected luminosity is not enough to regain sensitivity. If however, the chargino decays into sneutrino and a lepton, the branching ratio for this decay (into all three lepton flavors together) could be 100%, significantly increasing the possibility of stop detection.

[11] If not an on-shell W, than an off-shell one comes to mind. But then it would not be anymore a three body decay, but would turn into a four body decay highly suppressed due to the presence of two virtual particles.

5. Experimental Apparatus

The Fermi National Accelerator Laboratory (FNAL, Fermilab) is located in Batavia, near Chicago in Illinois, USA. Its accelerator complex accelerates protons and antiprotons and collides them at two collision points. On of them is surrounded by the Collider Detector at Fermilab (CDF) which provided data for this thesis. In the next sections we briefly describe the system of accelerators and the CDF detector.

5.1. Fermilab's Collider

The Fermilab collider is a hadron collider, that collides protons (p) with antiprotons ($\bar{p}$) at the center-of-mass energy $\sqrt{s} = 1.8$ TeV. The proton acceleration has several stages as shown on Fig. 5.1. The proton starts its journey as part of a hydrogen ion H^- and enters the **Cockcroft-Walton accelerator** where it receives 750 keV. Then it enters the **Linac**, (linear accelerator), which is about 150 m long. It consists of 9 electromagnetic cavities to which an oscillating high frequency electric field is applied. Inside the cavities there are metal drifting tubes. The timing is set in a way, that the H^- ions travel inside the drifting tubes while the polarity of the field is such, that it would slow them down and they get to gaps between the tubes when the polarity of the electric field enables their acceleration. The Linac accelerates the ions from 750 keV to 200 MeV (in 1992 upgraded to 400 MeV). After leaving the Linac, the H^- ions pass through a carbon foil, which "shaves" off the two electrons, leaving only the positive proton. The protons are then injected to a synchrotron, called the **Booster**. Here the protons are traveling around a circle in the magnetic field and are accelerated by electric field at various locations around the ring. They make about 20,000 rounds, until their energy exceeds 8 GeV. In order to be efficient, the Booster is designed to have 12 bunches of protons circling around at the same time. The next

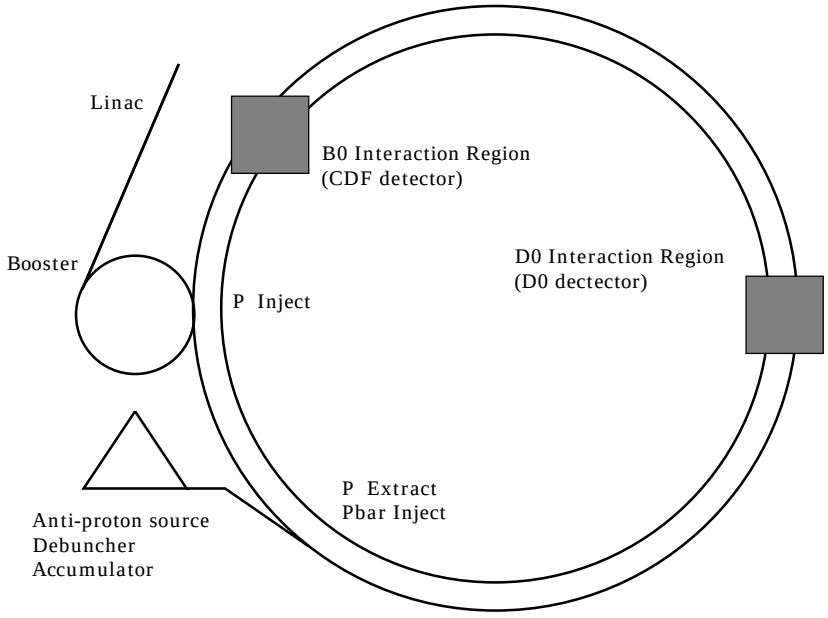

Figure 5.1. Fermilab's collider complex: Cockcroft-Walton (10 m, 750 keV), Linac (150 m, 200 MeV, in 1992 upgraded to 400 MeV), Booster (475 m, 8 GeV), Main Ring (6,283 m 150 GeV), Tevatron (6,283 m, 0.9 TeV)

part of the acceleration is done in the **Main ring**. It is a 6.3 km in circumference circle, containing about 1,000 conventional magnets which provide the magnetic field necessary to keep the protons in the circular path and to focus the diverging bunch. Six bunches of protons get accelerated to 150 GeV. Another six bunches leave the Main Ring earlier, with energies of 120 GeV. These are transported to a target area, and focused on a "sandwiched" copper-nickel-titanium target. The collisions with the target produce a wide range of secondary particles including 8 GeV antiprotons. These are selected and transported to the **Debuncher ring** where the bunches are reduced in size by a process known as stochastic cooling. The antiprotons are then transferred to the **Accumulator ring** for storage. When a sufficient number of them have been produced, the antiprotons are injected into the Main Ring and accelerated to 150 GeV. The final step in the acceleration of protons and antiprotons happens in the **Tevatron** where they are accelerated simultaneously in counterrotating beams

to energies of 0.9 TeV. The Tevatron is located in the same tunnel as the Main Ring and the magnetic field is provided by superconducting magnets. When the protons and antiprotons reach 0.9 TeV each, they collide at two of the four bunch crossing points named B0, C0, D0 and E0. The CDF experiment is located at the B0 point. The collision rate of protons and antiprotons is measured by the **instantaneous luminosity** ($\mathcal{L}$) defined by

$$\mathcal{L} = \frac{f_r n_{bunch} N_p N_{\bar{p}}}{A}, \tag{5.1}$$

where f_r is the bunch crossing rate (typically $1/3500\ ns^{-1}$), n_{bunch} is the number of bunches (typically 6), N_p ($N_{\bar{p}}$) is the number of protons (antiprotons) in the bunch (typically 2.32×10^{11} (5.5×10^{10})) and A is the effective cross sectional area of the beam overlap (around $5 \times 10^{-5}\ cm^2$). A typical instanteneous luminosity for Run 1A and Run 1B was $\mathcal{L} = 0.54 \times 10^{31}\ cm^{-2}/s$ and $\mathcal{L} = 1.6 \times 10^{31}\ cm^{-2}/s$ respectively. The Tevatron operates 24 hours a day except for some short periods of time allocated for maintenance. Therefore it is useful to define the integrated luminosity ($\int \mathcal{L}\mathrm{dt}$) as the measure of the number of collisions during a time period. Then the total number of events N expected from a process which has a total cross section σ is given by $N = \sigma \int \mathcal{L}\mathrm{dt}$.

5.2. The CDF Detector

The CDF detector was built to study the products of $p\bar{p}$ collisions. It is a forward backward and azimuthally symmetric device. It measures approximately 27 m from end-to-end and it is about 10 m high. CDF's coordinate system is defined as a right-handed coordinate system, with the positive z-axis pointing in the proton momentum direction, the x-axis is the horizontal direction, and the positive y-axis in the upward vertical direction. The origin is in the geometrical center of the detector. See Fig. 5.2.

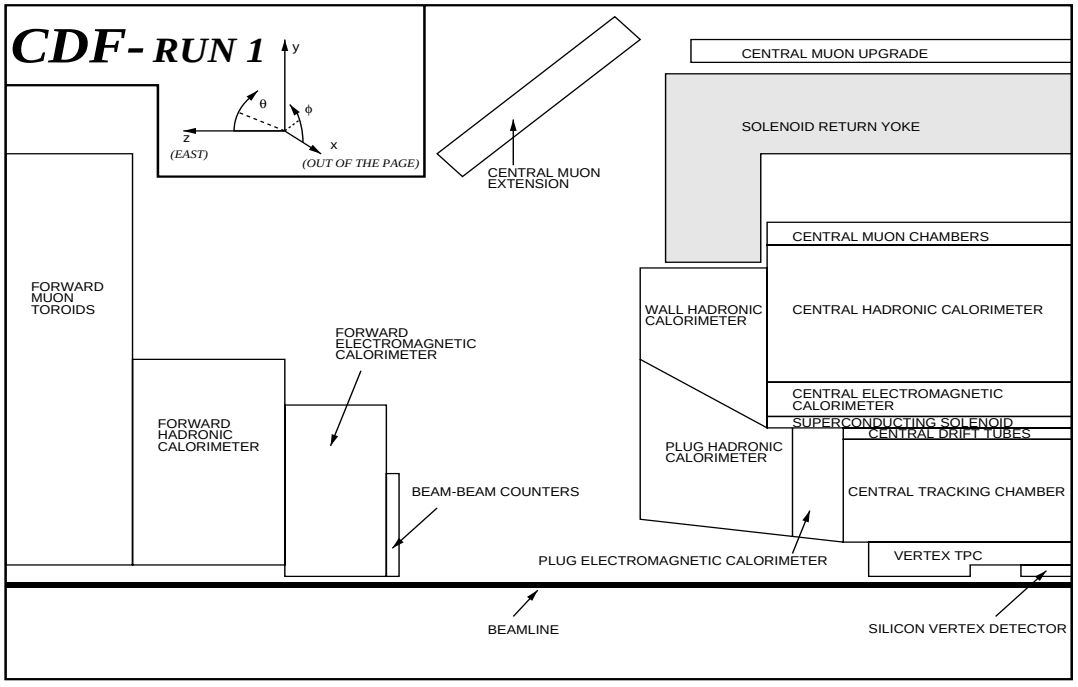

Figure 5.2. Side view cross section of quarter of the CDF detector. The interaction point is at the west end of the silicon vertex detector.

It turns out to be convenient to replace the polar angle θ by a variable η defined by

$$\eta \equiv -\ln(\tan(\frac{\theta}{2})),$$

which maps $\theta \in (0, \frac{\pi}{2})$ onto $(-\infty, 0)$ and $\theta \in (\frac{\pi}{2}, \pi)$ onto $(0, \infty)$. Variable η is called pseudorapidity because for high energy particles $\mathrm{p_T} \gg m$ (where m is the particle's rest mass) it gives a good approximation of the rapidity defined by

$$y = \frac{1}{2}\ln(\frac{E + p_z}{E - p_z}), \tag{5.2}$$

where E is the energy of the particle and p_z is the z-component of its momentum $\mathbf{p}$ and $\mathrm{p_T} = |\mathbf{p}|\sin\theta$. Since $\cosh^2\eta = 1 + \cot^2\theta$ and $\sinh^2\eta = \cot^2\theta$ we can rewrite (5.2) as

$$y = \frac{1}{2}\ln\left(\frac{\sqrt{\cosh^2\eta + \epsilon} + \sinh\eta}{\sqrt{\cosh^2\eta + \epsilon} - \sinh\eta}\right) = \eta - \frac{1}{2}\epsilon^2\tanh\eta + \mathcal{O}(\epsilon^4) \tag{5.3}$$

where $\epsilon = \frac{m}{\mathrm{p_T}}$ and we used the identity $\ln(\frac{1+x}{1-x}) = \mathrm{arctanh(x)}$. Therefore, if $\mathrm{p_T} \gg m$ then $y = \eta$.

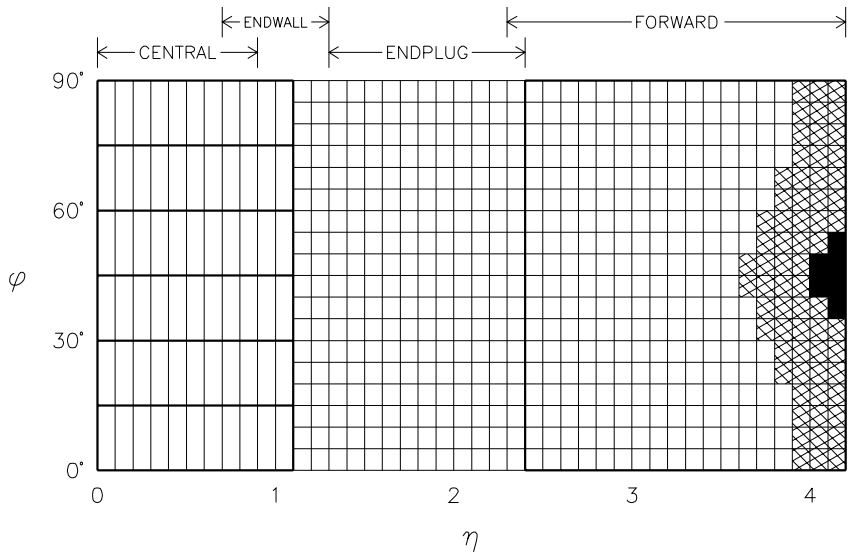

Figure 5.3. A calorimeter quadrant in $\eta - \phi$ coordinates. The electromagnetic calorimeters have coverage up to $\eta \leq 4.2$. The hatched cells have only partial hadronic coverage (due to the presence of magnets) and the black area has no coverage at all due to the beam pipe.

The detector was designed to be forward-backward and azimuthally symmetric, therefore the cylindrical coordinate system around the beam pipe is its natural coordinate system. Indeed, the $\rho = const.$ hyperplane then looks approximately as a Cartesian plane in (ϕ, η) variables as shown on Fig. 5.3.

The main parts of the detector are the beam-beam counters, tracking system, the solenoid, calorimeters and the muon chambers. The inner layers (see Fig. 5.2) of the detector are in a 1.4 T magnetic field produced by the solenoid, so the detector is able to distinguish the sign of the electric charge of particles.

5.2.1. Beam-Beam Counters

This part of the detector plays a crucial role for the experiment, because it measures the instantaneous luminosity. There are two planes of BBC perpendicular to the beam pipe positioned at $z = \pm 5.8$ m covering $3.2 < |\eta| < 5.9$. Each plane (See

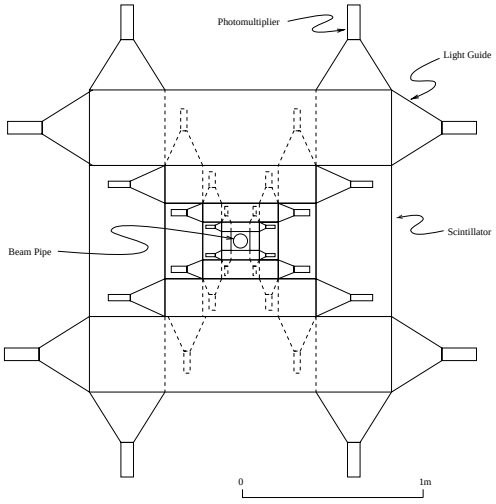

Figure 5.4. A schematic view of one set of Beam-Beam-Counters (BBC)

Fig. 5.4) consists 16 scintillator plates. Two phototubes, one at each end of the scintillator plate detect the light created when a charged particle crosses the counter. These counters record the rate of collisions. By monitoring the rate of hits in the BBC, dividing it by the BBC effective crossectional area, the instantaneous luminosity is calculated. BBC also serves as the minimum bias trigger. In order to activate this trigger, at least one of the scintillators **on both planes** has to have a hit within the 15 ns window centered on the beam crossing time.

5.2.2. Tracking System

SVX- Silicon Vertex Detector

The silicon microstrip vertex detector surrounds the beryllium beampipe with 4 layers, it covers $|\eta| < 1.0$ and has the geometrical acceptance around 60% (because its active length in z direction is 51 cm and the spread of the $p\bar{p}$ collisions is around $\sigma = 30$ cm). Its single hit resolution in the transverse plane (depends on the layer) is measured to be around 10 μm. Its impact parameter resolution for high momentum tracks

is measured to be around 17 μm. The inner most layer is placed at 2.86 cm and outermost layer is placed 7.87 cm from the beam line. Due to its strip geometry, SVX can provide only 2-D information in the $r-\phi$ plane. The silicon vertex detector is a very important source of information about displaced vertices, *f.e.* to resolve secondary vertices of b-quark decays (cτ= 500 μm).

VTX- Vertex Tracking Chamber

It covers $|\eta| < 3.25$ and provides (r-z) tracking information up to $\rho = 22$ cm from the beam line. VTX is made out of 8 octagonal modules divided into 8 separate wedges. The wires are in a mixture of 50% argon and 50% ethane gases. When a charged particle passes through, it ionizes the gas, the produced electrons cause a voltage drop on the sense wires and it is measured. Its resolution of the $p\bar{p}$ collision vertex in the z direction is 1 mm.

CTC- Central Tracking Chamber

The CTC surrounds SVX and VTX. Its angular coverage is $|\eta| < 1.5$ but the best momentum measurements are possible for $|\eta| < 1$. It is a cylindrical drift chamber, 2.76 m in radius and 3.2 m long. It is filled with a mixture of argon, ethane and ethanol. The CTC has 84 layers of sense wires grouped into 9 superlayers of two kinds and numbered from 0 to 8. (See Fig. 5.5.) The axial superlayers (0,2,4,6,8) have 12 wires parallel to the beam pipe, and the (1 and 5) stereo superlayers have 6 wires which are tilted by $+3^o$ with respect to the beam pipe and the 6 wires of superlayers 3 and 7 make -3^o angle with the beam pipe. The axial superlayers measure the tracks in r-ϕ plane, while the stereo superlayers provide also z information. The planes of the groups of 12 and 6 wires make a 45° angle with respect to the radial direction in order to compensate for the drift of ions caused by the 1.4 T magnetic field. The CTC measures the curvature of the tracks in order to determine the transverse momentum (p_T) of the tracks. The momentum resolution is given by $\delta p_T/p_T = 0.002 \times p_T$. If the information from the CTC is combined with the SVX, the resolution improves to $\delta p_T/p_T = 0.001 \times p_T$. The spatial resolution in the z direction is about 4 mm and in $\delta r\phi$ approximately 0.2 mm.

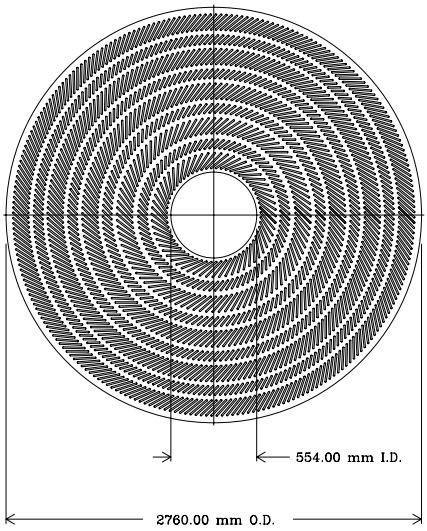

Figure 5.5. The Central Tracking Chamber-CTC. The layers of wires are shown on the picture.

5.2.3. Calorimetry

At CDF the energy of particles is measured by the shower sampling method. The calorimeters are made of two kinds of layers, the absorber material (with a high nuclear number Z), and the active read out material. As particles traverse through the absorber material, they lose energy and produce few daughter particles (called showers) which then interact with the active material. The scintillators "sample the shower". The showers penetrate through many layers and each time they are sampled by the active material until they are completely absorbed. The sum of the signal from the scintillators is proportional to the energy of the original particle. The energy of neutral particles can be measured in general only by determining the energy imbalance in the detector, however the photons are measurable in the electromagnetic calorimeters and neutral hadrons leave energy in the hadron calorimeters. The calorimeters are segmented in azimuth and pseudorapidity to form a projective "tower" geometry which points back to the nominal interaction point. There are three

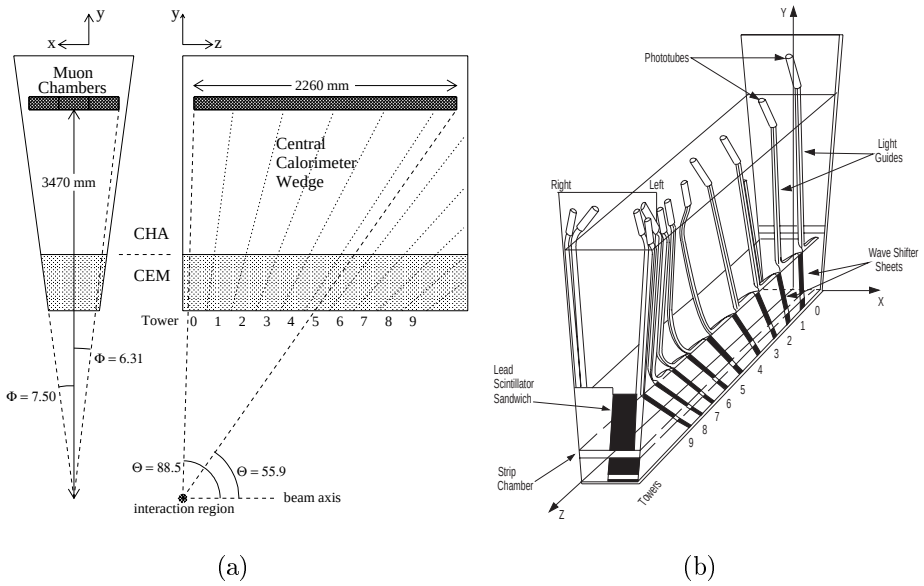

(a) (b)

Figure 5.6. The Central Electromagnetic Calorimeter(CEM): (a) one of the 24 wedges (b) wedge with the light gathering system.

calorimeter regions, central, plug and forward/backward, covering $\phi = (0, 2\pi)$ and $|\eta| < 4.2$. In our analysis we use the particles traversing the central region only. Each of the calorimeters have an EM part and a HAD part. The collision product meets the EM part first, which is used to measure the energy of electrons and photons, then the HAD part, which deals with the hadronic particles such as pions. The central calorimeter (see Fig. 5.6) is made up of 24 wedges and is placed around the beampipe, so one wedge covers 15° in ϕ. In the polar direction, one wedge is made out of 10 towers, all of them pointing to the center of the detector and each tower covers $\eta < 0.1$ (See Figs. 5.6). Towers 0-5 of CEM continue to CHA, towers 6-9 continue to CHA but share their ends with WHA. (See Fig. 5.2). The CEM uses polystyrene scintillator as the active read out material (31 layers each 5 mm thick) and lead as the absorber material (30 layers each 1/8 inch thick). The scintillator's light is collected through wavelength shifter bars on both sides of the wedge. The wavelength shifters transmit the light through acrylic light guides which are attached to photomultipliers located

at the rear end of each wedge (See Fig. 5.6). The fractional energy resolution for CEM is

$$\frac{\sigma(E)}{E} = \frac{13.5\%}{\sqrt{E_T/1GeV}}$$

There are proportional chambers embedded within the CEM, called the Shower Max Detector (**CES**) and the Pre-Shower Detector (**CPR**). (See Fig. 5.6). The CPR is located between the front face of the CEM and the surface of the solenoid. It gives information about early showers. CES, a gas wire chamber, is located at 6 radiation lengths within the CEM and reads out the transverse profile of the EM showers.

The CHA is located behind the CEM. It uses the same read out material as the CEM, but the absorber is steel. It contains 32 layers of 1.0 cm thick scintillators and 2.5 cm thick steel. The WHA has more steel, since for the same E_T the E of the particles which get to the WHA is greater. WHA is made out of 15 layers of 1.0 cm scintillators and 5.0 cm steel. The proportional resolution is given by

$$\frac{\sigma(E)}{E} = \frac{70\%}{\sqrt{E_T/1GeV}}$$

The above resolutions were measured by using test beams and the radioactive sources. The detailed description of CDF detector can be found in [37].

5.2.4. Muon Detection

Muons which get to the muon chambers usually have high p_T tracks in the CTC and very little energy deposited in the calorimeters. The central region is covered by 3 parts, the CMU, CMP and CMX (see Fig. 5.7). The **CMU** is a drift chamber built on the top of the CHA wedges. It is divided into 15° wedges in the azimuthal direction. In the polar direction it covers $|\eta| < 0.63$ but the active region is in fact smaller, namely only 84% of the solid angle due to the 2.4° gaps between the wedges. In addition to these gaps, there is a 1.5° gap at $\eta = 0$ between the arches. The CMU is divided into 16 drift cells made out of 4 layers and 4 towers. It provides 3-dimensional reconstruction of the tracks for muons which were able to get to the muon system, *i.e.* the muons with p_T at least 1.5 GeV since approximately 5 hadronic absorption lengths

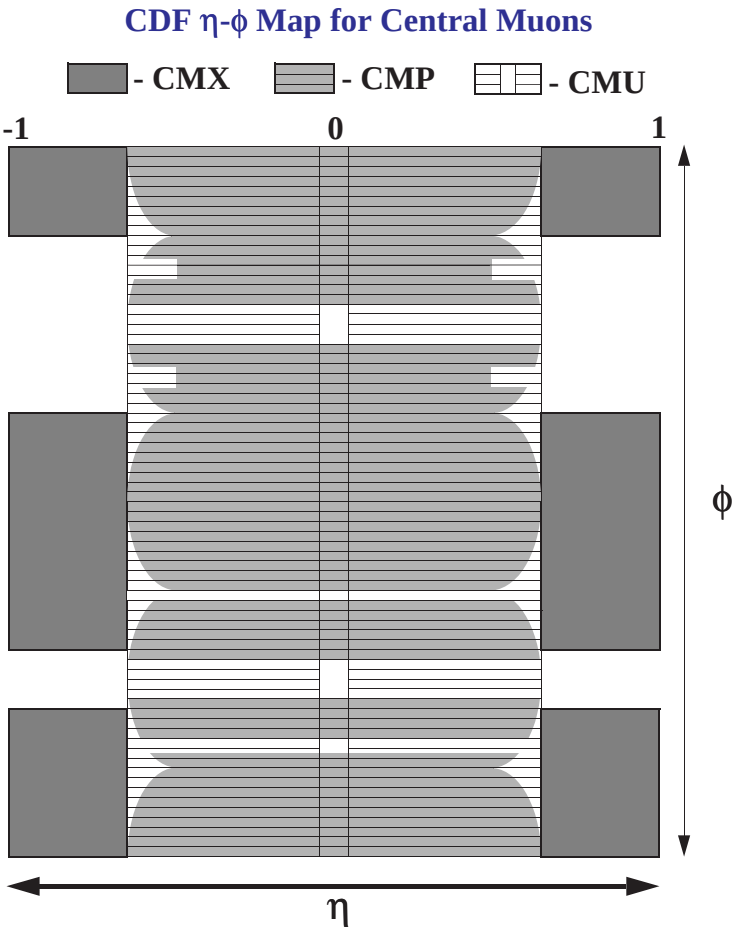

Figure 5.7. The $\eta - \phi$ muon coverage of the central region of the CDF detector.

of the central calorimeters separate the muon system from the interaction point. A mixture of argon and ethane fills the chambers. The anode wire pulses in each of the four layers are made as the muons traverse through them and leaves an ionization trail behind. The path of the muon in r-ϕ is deduced by measuring the time of arrival of each pulse. By off-setting the top two planes of the wires from the bottom two, one can resolve the left-right ambiguity. By measuring the pulse height at both ends of the anode wire the z-coordinate can be measured. The resolution in $r - \phi$ is 250 μm and 1.2 mm in z. The **CMP** sits on the 60 cm steel absorber behind the CMU. The purpose of the steel absorber is to absorb the "punch through's", hadrons leaving

from the CHA, which would fire the CMU. Muons which get to the CMP must have at least $p_T = 2.8$ GeV to penetrate all the intervening material. The steel reduces the punch-through rate by a factor of ~ 10. The CMP covers approximately 63% of its appropriate solid angle, so CMU and CMP together cover about 53% of the signal. The CMP detector is a wire chamber without scintillators for timing measurements. The next part, the **CMX** extends the CMU to the region $0.6 < |\eta| < 1.1$. It covers 71% of its possible solid angle due to cracks. It has 4 layers of proportional wire chambers for the track positioning, and scintillators for timing. The data from the forward region is not used in my analysis and the details of the forward muon systems as well as the previous parts can be found in [37].

5.2.5. Trigger System

The inelastic $p\bar{p}$ cross section at $\sqrt{s} = 1.8$ TeV is around 50 mb ($\sim 50 \times 10^{-27} cm^2$). Using a typical instantaneous luminosity $\mathcal{L} = 1.6 \times 10^{31} cm^{-2}/s$ we have about 800,000 inelastic collisions every second at CDF. We are limited by the existing storage media and we cannot record all these events. We need to make event preselections and write only the events that contain basic signatures of the physics, one is interested in. In order to do this, CDF uses three levels (L1, L2 and L3) of triggers with decreasing passing rate. Higher the level, less events it needs to examine but with greater details. In general, the trigers use the tower nature of the calorimeters and some tracking information coming either from the CMX chambers (see the previous section) or from a fast two-dimensional hardware tracker called the Central Fast Tracker (**CFT**). The trigger towers are 15° in ϕ direction and 0.2 in the polar direction η.

There is another factor that limits our data collecting capability. While the event information is read out by the detector electronics, the triggers cannot respond, even if there was a $p\bar{p}$ collision happening. Fortunately, most of the $p\bar{p}$ collisions are diffractive collisions only, and are of less interest than the deep inelasting collisions, which have small cross sections. So, one would say, there is not even the need to

record all the collisions. However, each collision has an equal probability to be an interesting one as well as not. Therefore it is necessary to process as many $p\bar{p}$ collisions as possible. At level 1 triggers, the decision to select or reject the event is made within 3.5 μs, and the rate[1] of events 280 kHz is reduced to about 2.5 kHz. Then the level two trigger further reduces this number to 20 Hz and the level 3 trigger reduces this number to about 5 to 8 Hz. The passing data is then written to storage media and later analyzed offline.

[1]Note that a bunch crossing is the definition of an event, therefore we can have more then one $p\bar{p}$ interaction in an event.

6. Search Strategy for the Scalar Top Quark

In this chapter we outline the overall strategy of the search for the lighter superpartner of the top quark in the CDF-collected dilepton data.

In Sec. 4.3 we started to study the stop quark in the framework of MSSM by calculating its pair production cross section. With the amount of data collected by CDF we expect a stop mass reach of 120 GeV/c^2 . We established that the 3-body stop decay shown below presents us the largest window of opportunity to search for the stop quark in our dilepton data.

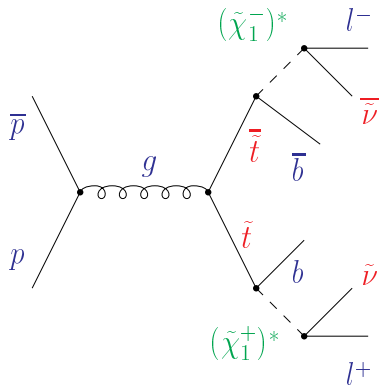

$$
\begin{aligned}
p\bar{p} &\rightarrow \tilde{t}\bar{\tilde{t}} \\
\tilde{t} &\rightarrow b\tilde{\chi}_1^{+*} \rightarrow bl^+\tilde{\nu}_l \\
\bar{\tilde{t}} &\rightarrow \bar{b}\tilde{\chi}_1^{-*} \rightarrow \bar{b}l^-\bar{\tilde{\nu}}_l
\end{aligned}
\qquad (6.1)
$$

Since it is the dominant decay mode, the sum of the decays into e, μ, and τ is 100%. The produced sneutrinos are escaping the detector undetected[1], giving rise to a substantial energy imbalance in the detector. Note that by considering the above path, another parameter entered our search: the sneutrino mass ($m_{\tilde{\nu}}$). Since there is no *a priory* reason to believe that different flavor sneutrinos would have different masses, we assume the sneutrinos to be degenerate.

[1] One could consider a further sneutrino decay $\tilde{\nu} \rightarrow \nu\tilde{\chi}_1^0$, where both the neutrino and the LSP escape the detector without leaving a trace. This however would not change anything from the detection point of view.

By examining the final state of the considered stop decay path, we conclude that the experimental signature by which the stop signal would manifest itself in the detector is the presence of:

- **two opposite-sign charged leptons**
- **b-quark jets**
- **significant missing energy in the event**

The considered decay path offers a rare (*i.e.* a relatively low-background) signature stop events which is, the presence of leptons in the final state. This will play a crucial role when we discuss various methods of extracting the stop signal from the large QCD background.

Our stop search follows the "blind analysis" technique and will proceed as follows:

1. We identify leptons, jets and missing energy in terms of measurable variables in the CDF detector.

2. From the CDF-collected data we select events containing two leptons, jets and considerable missing energy.

3. We identify known Standard Model processes that yield a signature similar to the stop signal.

4. We Monte Carlo generate and pass through detector simulation the stop signal events as well as the Standard Model background events.

5. We simulate non-prompt leptons and hadrons misidentified as leptons using non-stop-search CDF data samples.

6. On Monte Carlo events we develop methods to reduce the expected background while enhancing the expected stop signal.

7. After the desired signal to background ratio is achieved, we study the effect of the developed signal enhancing strategy on the CDF collected data and we search for the signal.

8. We study and estimate the statistical and systematic uncertainties on the expected signal and background.

9. We translate the number of observed events into a 95% confidence level (C.L.) upper limit on the number of signal events in our data sample.

10. We present the 95% C.L. excluded region in the $m_{\tilde{t}}$ vs $m_{\tilde{\nu}}$ parameter plane.

7. Reconstruction and Identification of Analysis Objects at CDF

7.1. Energy

Particles entering the calorimeters (see Sec.5.2.3) deposit energy, which is recognized as a signal by the calorimeter electronics. This signal is then converted to GeV units with the help of test beam runs and radioactive sources. There the detector towers are exposed to beams of particles of known energy. The calorimeter response is measured and the calibration conversion factors to GeV units are established. The $\eta - \phi$ coordinates of towers are represented by integer numbers IETA and IPHI. For the $\eta \leftrightarrow$ IETA correspondence see Tab. 7.1. Each IETA has 24 IPHI entries labeled 0-23 (corresponding to $\phi \in \{0°, 360°\}$. The IETA and IPHI values are then stored in an array, called TOWE bank. When real collision data were taken, TOWE receives the measured electromagnetic and hadronic energies of the towers, which are then accessed by various programs that need the energy measurements.

7.2. Tracks

The tracking chambers are placed in a magnetic field which permits measurement of track momenta via curvature. In the case of charged particles, the tracks show up as parts of helices with different curvatures starting at the interaction points. The neutral particles do not leave tracks. The reconstruction of tracks starts by taking the CTC axial superlayer hits and fitting them to a circle. This circle is then projected onto the CTC stereo superlayers and a 3-D fit of five parameters to a track-helix is performed. The five parameters used in this fit are:

Table 7.1
The $\eta \leftrightarrow$ IETA correspondence for the central calorimeters.

$\lvert\eta\rvert$	IETA	
	sign(η) = +	sign(η) = -
0.0000-0.1308	42	43
0.1308-0.2595	41	44
0.2959-0.3841	40	45
0.3841-0.5033	39	46
0.5033-0.6163	38	47
0.6163-0.7226	37	48
0.7226-0.8225	36	49
0.8225-0.9160	35	50
0.9160-1.0036	34	51
1.0036-1.1000	33	52

- the 2-D *curvature*, inversely proportional to the track's momentum
- the $\cot\theta$, where θ is the polar angle
- the *impact parameter* d_0 defined as the shortest distance of the track to the interaction vertex in the transverse plane (perpendicular to the $p\bar{p}$ beam)
- z_0, the z-coordinate of the closest point of the track to the interaction vertex
- ϕ_0 the azimuthal angle of the track at the point of the closest access to the interaction vertex.

Each CTC track is then extrapolated towards SVX and a search for additional hits is performed. If found, a new fit is performed and the track characteristics are recalculated.

7.3. Vertices

In the vertex finding procedure, the tracks reconstructed in the VTX detectors are used. A vertex is defined as the origin (meaning the closest approach to the beam

axis) of a VTX track. Usually there are several vertices per event. They are stored in an array called VTZV bank. The vertex which has the highest VTX hit occupancy is called the *event vertex* and is used to determine the θ coordinate of calorimeter towers. Also the transverse energy $\mathrm{E_T} = E \sin\theta$ of towers is calculated according to this vertex.

7.4. Electron Identification

When high energy electrons enter the electromagnetic calorimeter, they interact with the EM field around atomic nuclei and create e^+e^- pairs or photons. These secondary EM particles are also very energetic and thus each can produce e^+e^- pair, Compton electrons, and photons. This way a spray (shower) of charged particles is produced (until the parent particles get below a minimum showering threshold) and its characteristics can be used to determine that the original parent was an electron. The first step to identify electrons is to find electron showers in the EM calorimeter (electron showers are largely complete before the Had calorimeters). This is done by identifying clusters (in $\eta - \phi$ space) of electromagnetic energy.

7.4.1. Clustering

An electron cluster is defined by a seed tower (any tower that has more than 3 GeV of transverse energy) and shoulder towers (the towers nearby the seed tower which have at least 0.1 GeV of transverse energy). The clustering algorithm starts with a seed tower, and adds to its energy the energy of shoulder towers (if they exist) until the maximum cluster size is reached or no shoulder tower exist. The maximum cluster size is 3 towers in polar and 1 tower in azimuthal directions ($\Delta\eta \times \Delta\phi \sim 0.3 \times 15^\circ$) in the case of central electrons. This is done for each seed[1]. The cluster characterizing variable values are stored in an array: the CLSL bank. Each cluster is an *a-priori* electron candidate, but we have to be careful, because hadron showers also leave

[1]There are mechanisms developed to treat overlaping clusters. We do not discuss such details here.

traces of clustered EM energy. In order to decrease the chance of misidentification, quality cuts are imposed on various variables (identification variables) characterizing the found clusters of energy.

But first we list some geometrical requirements on the clusters.

7.4.2. Geometrical Requirements

In our analysis only electrons detected in the central region of the detector are considered. As we already mentioned, the central electromagnetic calorimeter covers the region with $|\eta| \leq 1.1$. The following requirements were developed in order to make sure that the candidate electrons were far from the boundaries of the detector, so their energies were well measured.

- Following the notation of Fig. 5.6, only towers 0 to 8 are allowed to be seed towers. There is one exception, the wedge which is around the chimney (a crack containing cables and pipes connected to the solenoid). This wedge has only 8 towers, towers 9 and 10 are missing. In this module, only towers numbered 0-6 can be seed towers.

- The crack at $\eta = 0$ where the two halves (east and west) of the detector meet are avoided by requiring that the z coordinate of the cluster is outside the interval $-9\ cm \leq z \leq 9\ cm$.

- The electron shower must be at least 3.2 cm away from the azimuthal boundary of a CEM wedge. Since the width of CEM wedges at the position where the shower detector is located is 48.5 cm, this means that the track must be located within 21 cm from the tower center in the azimuthal direction, a 13% geometrical inefficiency.

- There must be at least one, 3 dimensional track pointing to the electron cluster. This ensures that the particle went through a sufficient number of layers of the CTC, raising the quality of its detection.

All these requirements are commonly referred to as fiducial cuts and are done by a the FIDELE routine. After these fiducial cuts, 78.9% of the central region remains active.

7.4.3. Electron Identification Variables

The following variables define electrons in terms of measurable quantities at the CDF detector. Specific values to these variables will be assigned in Sec. 8, here we give their general description.

- The transverse energy E_T of the electron cluster.
- The transverse momentum p_T of the CTC track associated with the electron.
- The ratio E/P of the cluster energy to the track momentum. Due to bremsstrahlung, electrons often radiate soft photons. Since these photons tend to be narrowly collimated with the electron track, their energy usually gets deposited to the same EM cluster. Therefore the bremsstrahlung photons do not distort the electron's candidate energy measurement, but they tend to lower its measured momentum. Electrons from our hard scatterings have energies in the GeV scale which means they are ultra-relativistic. Therefore we expect $E \cong P$. When E/P is too small, it also indicates a possible mismeasurement of the electron's energy.
- The ratio E_{HAD}/E_{EM} of the hadronic energy and the electromagnetic energy of the cluster. This variable measures the leakage of energy from the EM calorimeter into the HAD calorimeter. Its cut value is usually set to slide with the energy of the electron candidate to allow for the greater average energy leakage for electrons with higher energies. It was designed to distinguish electrons (that should have very little hadronic energy) from jets (which should have mostly hadronic energy, but sometimes can have some EM energy as well) without rejecting too many electrons. The E_{EM} here means the total electromagnetic

energy of the cluster calculated as the sum of the EM energies of cluster towers. The E_{HAD} denotes the hadronic energy of the trigger tower (which is in fact a pair of scintillator towers) that is behind the cluster. In the case of electrons, one expects E_{HAD}/E_{EM} to have small values and for jets, one expects higher values. However, the E_{HAD}/E_{EM} finding algorithm uses the first listed HAD trigger tower behind the EM cluster and uses that hadronic energy. In some cases (when there are two trigger towers[2] very close to each other, one with lot of HAD energy, and one with a tiny amount of HAD energy), the algorithm can first encounter the trigger tower with very little HAD energy, and would miss the other one with a larger HAD energy if it existed. Then the E_{HAD}/E_{EM} is small and passes the electron identification cuts and what in fact is a jet can be identified as an electron.

- The ratio E_{3HAD}/E_{EM} was introduced in order to cure the possible problem described above. E_{EM} is the same as above, *i.e.* it is the EM energy of the cluster, but the E_{3HAD} is now taken to be the total hadronic energy of all of the towers present in the cluster.

- The lateral shower profile L_{shr}. It is a quantity that helps to take into account the fact that electron showers sometimes spread over more than one electromagnetic tower. It measures the lateral sharing of energy among adjacent cluster towers.

$$L_{shr} \equiv 0.14 \times \sum_i \frac{E_i^{adj} - E_i^{expect}}{\sqrt{0.14^2 \times E^{clust} + (\Delta E_i^{expect})^2}},$$

where the sum runs over the two towers adjacent to the seed tower in the same azimuthal wedge, E_i^{adj} is the energy deposited in the i-th adjacent tower, E_i^{expect} is the energy expected in that tower (based on the projected direction of the electron track), ΔE_i^{expect} is its uncertainty and E^{clust} is the energy of the cluster. All energies are in GeV. The E_i^{adj} is a function of several variables such as the energy of the seed tower, the z position and the angle of the electron shower

[2] two tower pairs, *i.e.* 4 towers total

(determined by the Central Strip Chamber CES), the event vertex and the shower parameterization obtained from the test beam data.

- The strip chamber profile comparison variable χ^2_{strip}. The CES provides a transverse profile of the electron shower at the expected shower maximum. The quantity χ^2_{strip} is the χ^2 of the comparison of the measured pulse height in z with the one expected from the test beam data. A small value of the χ^2_{strip} ensures that the electron candidate exhibits the same characteristics as its test beam counterpart.

- The track to shower matching variables Δx and Δz. When CTC tracks point towards EM clusters, we extrapolate them into CES. Then the obtained track position in CES and the actual CES position of the shower can be compared. This comparison is done in the $r-\phi$ plane and the Δx is obtained. Similarly the z positions are compared as well and the Δz is obtained. By requiring a good matching (small values of Δx and Δz) a background from overlaping neutral or charged hadrons can be significantly reduced.

- The tracking isolation ISO^{trk}. This variable is defined by

$$ISO^{trk} \equiv (\sum_{\Delta R<0.4} \mathrm{p_T}) - \mathrm{p_T}(electron), \tag{7.1}$$

  where the sum runs over all tracks present in the cone $\Delta R < 0.4$ (measured in the $\eta - \phi$ plane) around the track associated with the electron candidate whose $\mathrm{p_T}$ is denoted by $\mathrm{p_T}(electron)$. This variable has high values for jets (lot of tracks close to each other) and small values for electrons.

- The number of hits in the CTC, characterized by the "goodness" of the track. A good track associated with an electron candidate is a 3-D track that has at least six hits in the CTC, where at least 3 hits are in the axial superlayers and at least 2 hits in the stereo superlayers.

Figure 7.1(a) shows the distributions of some of the above quantities plotted for electron candidates found in the dilepton data sample.

7.4.4. Removal of Electrons Originated in Photon Conversions

Occasionally, when photons, present in the scattering process interact with the detector material, they create an electron positron pair. These electrons are removed from the search sample[38] by a routine called CONVERT2. It searches for a track with opposite sign to the track of the electron candidate. In the case of conversion electrons, their tracks are expected to be very close to each other at the point of conversion (where their helices coincide) in both $r-\phi$ space ($\Delta_{\text{separation}}(r,\phi) \leq 0.3$) and θ ($\delta(\cot\theta) \leq 0.06$) coordinate. Furthermore, the radial distribution R_c (defined as the distance from x=y=0 to the conversion point) was studied, and the material structures of the detector (beampipe, SVX, VTX ...) showed up as peaks. These tracks were removed with geometrical cuts on R_c. If the photon converts outside of the VTX then there is a deficit of wire hits along the direction pointing to the CTC track. Then it turns out to be powerful to put a cut on the expected vertex occupancy. If the occupancy is less then 20% of the expected one, the electron candidate is disregarded.

7.5. Muon Identification

Muons being heavy copies of electrons penetrate matter very easily. They are able to pass through the EM and Had calorimeters and leave tracks (besides in CTC) in the muon drift chambers- CMU, CMP and CMX. The location of the muon in the chamber is determined by the drift-chamber time-distance relation in the ϕ direction and by charge division in the z direction. An object considered as a muon must have aligned hits in both $r-\phi$ and $r-z$ planes on at least 3 separate layers. These hits form a so called "muon stub" which is then matched to the CTC tracks extrapolated to the muon chambers. These muons are then called Central Muons and are stored in an array called the CMUO bank. Their fiducial volume is given by the muon chamber coverage and extends to $|\eta| \leq 1.0$. As we have seen however, the muon chambers cover only approximately 53% of the central region, therefore we introduce an additional category of muons, called the Central Minimum Ionizing Particles (CMIO). These are

stored in an array called CMIO bank. CMIO tracks do not have a muon chamber hit, have limited calorimeter energy deposition, and are required to have $|\eta| \leq 1.2$ where η is measured from the detector origin.

7.5.1. Muon Identification Variables

The following variables are used to define muons in terms of measurable quantities at the CDF detector.

- The transverse momentum p_T of the CTC track associated with the muon.
- The energies E_{EM}, E_{HAD} deposited in the electromagnetic and hadron calorimeters. High p_T muons are not expected to deposit substantial energy in the electromagnetic calorimeter since it does not have enough interaction material. In the hadronic calorimeters the deposition is higher but still quite small in comparison to strongly interacting jets. We will therefore limit the E_{EM}, E_{HAD} from above to distinguish muons from jets.
- The impact parameter d_0 *i.e.* the distance of the closest approach of the reconstructed track to the beam line. It requires the muon to originate from the nominal interaction region. This variable helps to reduce muons from decays-in-flight or the cosmic muon background whose tracks can have arbitrarily large impact parameters.
- $|\Delta x|$ OR χ^2_s. $|\Delta x|$ is the distance in the $r-\phi$ plane between the extrapolated track and the stub segment in the appropriate muon chamber. χ^2_s measures the quality of the matching of the extrapolation of the CTC track and the track segment in the appropriate muon chamber. This variables are not applicable to CMIO's.
- The track quality, the "goodness", is identically defined as in case of electrons.
- The tracking isolation ISO^{trk} defined by Eq. 7.1.

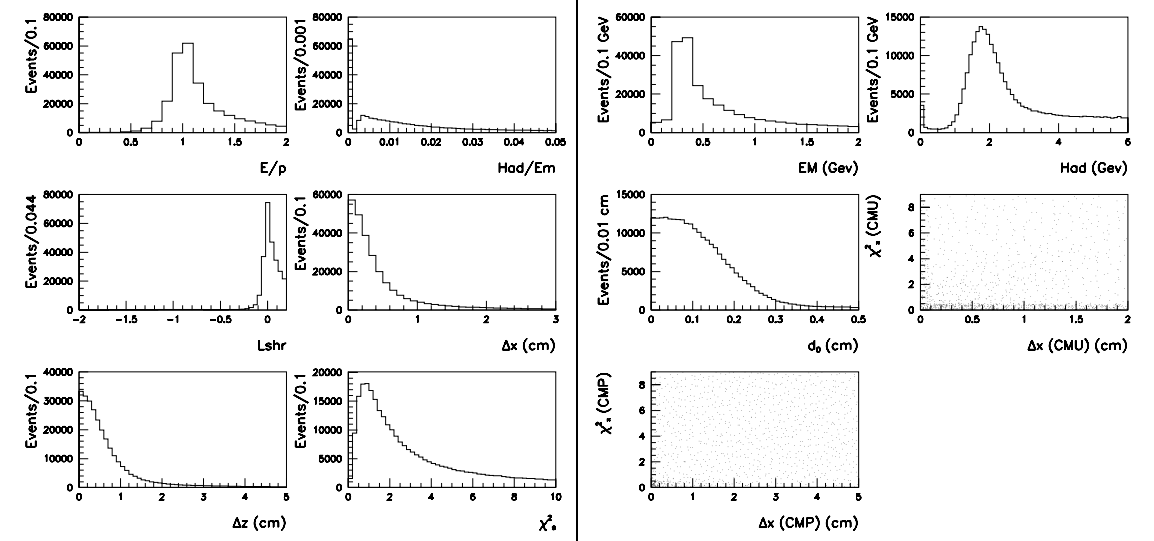

(a) Electron identification variables

(b) CMU or CMP identification variables

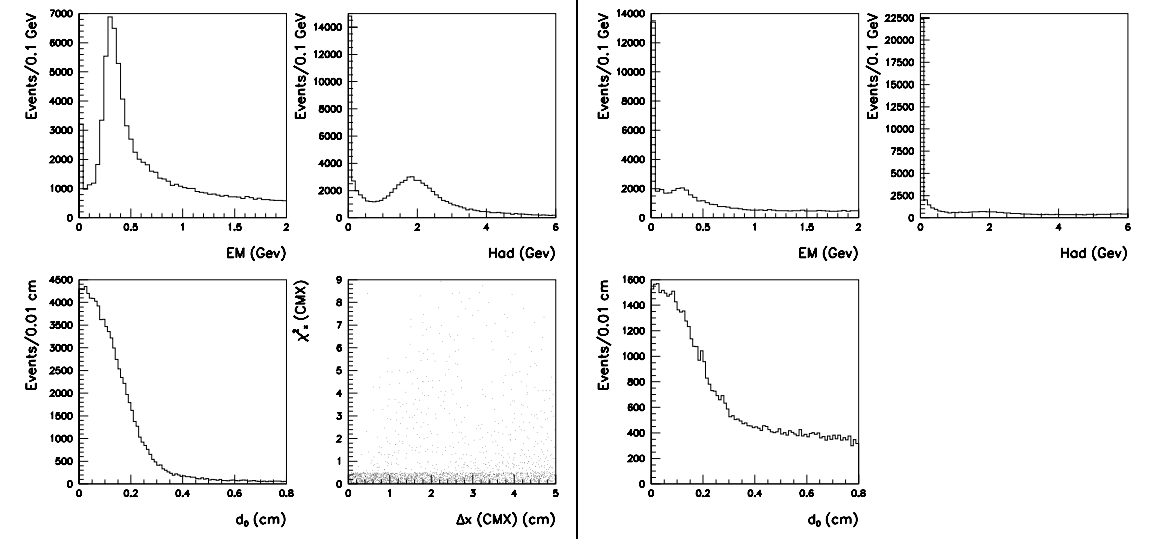

(c) CMX identification variables

(d) CMIO identification variables

Figure 7.1. Examples of the distributions of various electron and muon identification variables.

Figures 7.1(b)-7.1(d) show the distributions of some of the above variables used in the dilepton sample.

7.5.2. Cosmic Rays Removal

Cosmic rays (cosmics) constantly hitting the atmosphere create showers of particles which very often decay to muons leading to a flux of muons through our detector. These muons can leave a nearly straight track (mimicking a very energetic $\mu^+\mu^-$ pair) in the CTC with an arbitrary impact parameter depending on where the muon entered the detector. Therefore cosmics can be reduced by putting an upper limit on the impact parameter d_0. From the detector's point of view, the remaining cosmics manifest themselves as dimuon events with CTC tracks that are very much back-to-back. These events would have strange timing of their hits in the hadronic calorimeters. These times measured by the Time to Digital Converter (TDC) show a difference roughly equal to the speed-of-light transit time from one side of the calorimeter to the other. Therefore cosmic muons will be identified and eliminated by:

- placing cuts on the opening angles of the very back-to-back muon pairs
- asking for valid hadron TDC information on muons and a substantial time delay between the hits of the two muons in the hadronic calorimeter

7.6. Jet Reconstruction

During a hard hadron collision, quarks and gluons (partons) are produced. Since they carry color charge, they are subject to a very strong QCD force. Their broken color lines create quark-antiquark pairs from vacuum (and color line fragments correspond to quark-antiquark bound states, *i.e.* mesons) while they keep slowing down. This continues until the original partons slow down enough that they can also form colorless hadrons with some of quarks from the created $q\bar{q}$ pairs. Depending on the available energy, usually a large number of hadrons is formed. These hadrons are spatially close in direction to each other and form a spray (called a **jet**) of collimated particles in the direction of the original parton. The above-described process is called *fragmentation* or *hadronization*. It is governed by a *fragmentation function* $D_k^h(z)$,

which is defined as follows: Consider a fast parton k with energy E_k, producing among others, a hadron h with energy E_h. We denote z the fraction $z = E_h/E_k$. Then the probability of finding h in the range $(z, z + dz)$ is given by $D_k^h(z)dz$. The fragmentation function is assumed to be universal, independent of the scattering process. It is also an experimentally measurable variable. The detailed knowledge of $D_k^h(z)$ is necessary to be able properly simulate the jet productions at hadron colliders. For details, see [39].

After the jets get produced, they enter the EM and HAD calorimeters where they deposit energy. A jet "cone clustering" algorithm is then applied to identify the jets and then a jet energy correction algorithm is applied to correct these measured energies for various imperfections.

7.6.1. Jet Clustering

The jet finding algorithm at CDF is based on the tower nature of the calorimeters. At CDF the *fixed cone* algorithms [40] is applied. This algorithm starts with the definition of the cone size R in $\eta - \phi$ space by

$$R = \sqrt{(\Delta\eta)^2 + (\Delta\phi)^2}.$$

It is customary to choose cone sizes of $R = 0.4,\ 0.7$ or 1.0. Then a list of seed towers (towers with energies above a certain threshold E_T^{seed}) is made. A precluster of adjacent towers in the cone of R around the seed tower is made. Then the $\mathrm{E_T}$ weighted centroid of the cluster is found and a new cone of R is drawn around it and all towers containing more than 0.1 GeV energy are grouped together. The new centroid of these merged towers is calculated and a new cone is drawn centered around it. A new list of merged towers is then created. This process is repeated until the list of merged towers within the cone remains unchanged and no more pre clusters exist.

It could happen, that some jets overlap. If towers of one cluster are a subset of another bigger cluster, the cluster with the smaller E_T is dropped. If the overlap of the clusters is partial, an overlap variable f_0 is defined

$$f_0 = \frac{\sum E_T(common\ towers)}{\sum E_T(towers\ in\ the\ smaller\ E_T\ cluster)}.$$

If f_0 is larger then 0.75, the two clusters are combined into one. On the other hand, if the overlap function is smaller then 0.75, the two clusters are treated as separate jets. The common towers are divided between the the two clusters. Each common tower is assigned to the cluster to whose center it is closer. New centroids are recalculated for each cluster and the overlaping towers are redivided accordingly. This is repeated until the list of towers within the cluster does not change. Various jet describing variables are calculated for every cluster. Each EM or HAD tower in the cluster is assigned a massless 4-vector $q^i = (E^i_x, E^i_y, E^i_z, E^i)$ whose magnitude is the $i-th$ tower energy E^i and its 3-D vector points from the event vertex to the center of the $i-th$ tower. The 3-D components (E^i_x, E^i_y, E^i_z) of q^i are the projections of E^i onto the coordinate axis. We define the jet momentum $\vec{p} = (p_x, p_y, p_z)$, jet energy E, jet transverse energy E_T, jet azimuthal angle ϕ and the jets polar angle θ as:

$$p_x \equiv \sum_i E^i_x, \quad p_y \equiv \sum_i E^i_y, \quad p_z \equiv \sum_i E^i_z, \quad E \equiv \sum_i E^i \tag{7.2}$$

$$\phi \equiv \arctan\frac{p_y}{p_z}, \quad \theta \equiv \arcsin\frac{\sqrt{p_x^2+p_y^2}}{\sqrt{p_x^2+p_y^2+p_z^2}}, \quad E_T \equiv E\sin\theta, \tag{7.3}$$

where the sums run over the towers within the specified cone radius R.

7.6.2. Jet Corrections

The jet energy found in the previous section is not the initial energy of the produced parton as we would wish. The E is referred to as the "raw" or "uncorrected" jet energy E^{raw}. Experience shows, that the measured E of the jet is different then the actual energy of the quark or gluon for the following reasons:

- the hadron calorimeter response is not always linear in the whole range of measured energies. Test beam measurements show nonlinearities for low momentum particles;
- there might be particles that deposit their energy near the boundaries of the calorimeters
- some energy might be lost if part of the jet is outside the chosen jet cone
- if muons or neutrinos were part of the jets, they will not be detected and therefore their energies would not contribute to the jet energy.
- if some charged hadrons in the jet have low momentum, the solenoid field could prevent them getting to the calorimeters, so they do not contribute even if they were part of the jet.
- particles from the non-deep-inelastic process such as spectator quarks or gluons might contribute to the jet energy (so called underlying events).

We use the standard CDF's absolute jet correction method done by the "JTC96X" routine with NNDD[3] options. The corrections are usually around 30%. The jet energy "fixed" with these correction algorithms is referred to be the "corrected" jet energy E^{corr}.

7.6.3. Jet Identification Variables

In order to identify jets in our sample we use the following quantities:

- the corrected transverse energy E_T^{corr};
- the pseudorapidity η, which is measured from the the origin of the detector to the calorimeter cluster of the jet;

[3]no out-of-cone corrections, no-underlying-events corrections, default absolute and relative corrections

- the separation ΔR of the jet from leptons. Since the electrons are jets too, we have to make sure that the jet is not within a cone ΔR of an electron;
- the charge fraction (CF). The CF is defined as $CF \equiv \frac{\sum p_T^{jet}}{E_T^{jet}}$, where $\sum p_T^{jet}$ is the scalar sum of the transverse momenta of the CTC tracks associated with the jet, and E_T^{jet} is the corrected transverse energy of the jet.

7.7. Missing Transverse Energy Reconstruction

Due to missmeasurements or due to particles that escape the calorimeters undetected, such as neutrinos, the total detected energy in the calorimeters does not correspond to the energy sum of the proton and antiproton energies. In order to describe this energy imbalance, the variable $\not\!\!E_{\rm T}$, called the missing transverse energy[4] (imbalance of energy in the transverse plane) is introduced. The missing longitudinal energy is in most cases an irrelevant quantity since the protons not being elementary have partons with different boosts along the beam direction. We do not know their energies before the collision anyway and we cannot in any way measure the longitudinal energy which escapes from the detector at very large $|\eta|$.)

The "x-component" and the "y-component" of the missing energy are calculated with the help of the massless 4-vector $q^i = (E_x^i, E_y^i, E_z^i, E^i)$ introduced in Sec. 7.6.1.

$$\not\!\!E_{{\rm T}x} \equiv -\sum_{i=1}^{N_{towers}} E_x^i, \qquad \not\!\!E_{{\rm T}y} \equiv -\sum_{i=1}^{N_{towers}} E_y^i,$$

where the sum runs over all towers of the detector above threshold, where the tower energy threshold depends on which region of the detector the tower is in. Having defined $\not\!\!E_{{\rm T}x}$ and $\not\!\!E_{{\rm T}y}$ we can define the transverse missing energy variable $\not\!\!E_{\rm T}$ and its azimuthal angle $\phi_{\not\!\!E_{\rm T}}$ by

$$\not\!\!E_{\rm T} \equiv \sqrt{\not\!\!E_{{\rm T}x}^{\,2} + \not\!\!E_{{\rm T}y}^{\,2}}, \qquad \phi_{\not\!\!E_{\rm T}} \equiv \arctan\frac{\not\!\!E_{{\rm T}y}}{\not\!\!E_{{\rm T}x}}.$$

[4]Since $p\bar{p}$ have longitudinal momenta only, after their collision the momenta of the products must be balanced in the transverse plane.

The missing transverse energy discussed in this section is called the "raw " missing transverse energy.

7.7.1. Missing Transverse Energy Corrections

The raw $\not\!\!E_{\rm T}$ directly obtained from the vector sum of the energy is deposited in the calorimeter towers may be over or under-estimated due to the same reasons as the raw jet energy discussed in Sec. 7.6.2 needs corrections in addition to the effects we corrected the raw jet energy for, we will correct the raw missing transverse energy also for muons passing through the calorimeters with no or minimal energy deposit.

First we add to the raw $\not\!\!E_{\rm T}$ the corrections of the two jets of the event.

$$\begin{aligned} \not\!\!E_{{\rm T}x}^{\ CORR} &= \not\!\!E_{{\rm T}x}^{\ RAW} + \sum_{j=1}^{N}(E_x^{corr}(j^{th}jet) - E_x^{raw}(j^{th}jet)), \\ \not\!\!E_{{\rm T}y}^{\ CORR} &= \not\!\!E_{{\rm T}y}^{\ RAW} + \sum_{j=1}^{N}(E_y^{corr}(j^{th}jet) - E_y^{raw}(j^{th}jet)), \end{aligned} \tag{7.4}$$

where N is the number of jets in the event used for the analysis. If *e.g.* the k-th jet is missing for an event, the correction for that jet is missing as well.

The correction for muons is done by treating the muons as minimal ionizing particles, *i.e.* particles with tracks (therefore with measured $p_{\rm T}$) but minimal energy deposit. The correction of the $\not\!\!E_{\rm T}$ is then done by vectorial subtraction of the transverse momentum of the muon track from the raw missing transverse energy[5]. For completeness we vectorially add an amount of up to 2 GeV in the direction of the muon's track to the raw $\not\!\!E_{\rm T}$ in order to take into account the average energy deposited by muons in the calorimeters. Therefore we have

$$\begin{aligned} \not\!\!E_{{\rm T}x}^{\ CORR} &= \not\!\!E_{{\rm T}x}^{\ RAW} - \sum_{muons} {p_x}^{muon}\left(+\sum_{muons}\frac{p_x^{muon}}{|\mathbf{p_T}^{muon}|}\times 2\right) \\ \not\!\!E_{{\rm T}y}^{\ CORR} &= \not\!\!E_{{\rm T}y}^{\ RAW} - \sum_{muons} {p_y}^{muon}\left(+\sum_{muons}\frac{p_y^{muon}}{|\mathbf{p_T}^{muon}|}\times 2\right), \end{aligned} \tag{7.5}$$

[5]Keep in mind that the raw $\not\!\!E_{\rm T}$ is a negative number by definition

where the sum runs over all the muons in the event used for the analysis. From now when we refer to missing transverse energy, we mean the corrected $\not\!\!E_{\mathrm{T}}$.

8. Identification of Leptons, Jets and the Missing Transverse Energy.

8.1. Selection and Categorization of Leptons

The $\tilde{t} \to b\tilde{\nu}l$ decay channel leads to the presence of leptons in the events. In the CDF-collected data we only searched for electrons and muons, because during the data collection period we did not have τ triggers available[1]. The leptons are identified by using tracking, calorimeter and muon chamber information as described in detail in Sec. 7. Due to the presence of higher p_T single lepton triggers as well, we introduce a high(low) quality lepton, called the tight(loose) lepton by imposing specific cuts on the identification variables discussed in Sec. 7. The tight lepton ID cuts significantly lower the chance that a lepton is misidentified, but they lower the efficiency of selecting a lepton as well. The loose lepton's quality cuts act the opposite way. They are less stringent therefore a misidentification chance increases, but they lead to higher efficiency of the signal sample. To identify tight and loose leptons, we use an optimized set of cuts developed upon the experience built by previous dilepton analyses[41] done at CDF. Tab. 8.1 lists the identification cuts of electrons suited for our stop quark search. Two categories of electrons are defined, Tight Central Electron (TCE) and Loose Central electron (LCE)[2]. Note the E_T(TCE) $\geq$ 10 GeV and E_T(LCE) $\geq$ 6 GeV. In case an electron passes both tight and loose requirements, it is listed as TCE.

[1]Also, the tau-lepton identification is a difficult and complicated process with low resulting efficiencies not worth of the needed effort. When the produced τ leptons decay leptonically, such events could get to our search sample.

[2]We use only central electrons to avoid a possible increase in misidentification of electrons due to the insufficient tracking information in the plug region.

Table 8.1
Electron identification cuts used in the Run 1 stop search. The "hemcut" is defined as $0.055 + 0.045(E/100)$. It is designed to proportionally allow more energy of the electron candidate to leak into the hadronic calorimeter in case the electron has substantial energy E.

Name	Tight electron TCE	Loose electron LCE
Calorimeter	CEM	CEM
p_T (GeV/c)	> 5.0	> 3.0
E_T(GeV)	$>$ **10.0**	$>$ **6.0**
E/P	< 2.0	< 2.0
E_{HAD}/E_{EM}	< 0.05	$<$ hemcut
E_{3HAD}/E_{EM}	< 0.05	$<$ hemcut
L_{shr}	< 0.2	< 0.2
CTC-CES match $\Delta x(cm)$	< 3.0	< 3.0
CTC-CES match $\Delta z(cm)$	< 5.0	< 5.0
Strip χ^2	< 10.0	< 15
Good track	yes	yes
FIDELE	yes	yes
CONVERT2	pass	pass
$ISO^{trk}_{0.4}$ (GeV/c)	< 4	< 4

Tab. 8.2 categorizes the muon candidates by introducing the Tight Central Muon (TCM), Loose Central Muon (LCM), Loose eXtension Muon (LXM) and Loose CMIO Muon (LMI). Note the p_T(TCM) $\geq$ 10 GeV/c and that p_T(LCM, LXM) $\geq$ 6 GeV/c. The CMIO's are required to have p_T above 10 GeV/c to reduce their misidentification probability due to not having a muon chamber information available. As part of the cosmic muon contamination removal: (1) we required muons to have valid hadron TDC information available (2) we eliminated events with muon candidates that have a partner within the CMUO or CMIO banks that has valid HTDC information but is out of time ($\Delta t \geq 10ns$) (3) each muon candidate is also checked for the existence

Table 8.2
Muon identification cuts used for the Run 1 stop search. The "**or**" means that either the x coordinate matching or its χ^2 cut is applied. The cut on $\Delta HTDC$ and the back-to-backness is described in the text.

Name	Tight muon	Loose muon		
	TCM	LCM	LXM	LMI
Muon chamber	CMU/CMP	CMU/CMP	CMX	-
p_T (GeV/c)	**>10.0**	**> 6.0**	**> 6.0**	**> 10.0**
E_{EM} (GeV)	< 2.0	< 2.0	< 2.0	< 2.0
E_{HAD} (GeV)	< 6.0	< 6.0	< 6.0	< 6.0
Raw d_0 (cm)	< 0.5	< 0.5	< 0.5	< 0.5
d_0 (cm)	< 0.2	< 0.5	< 0.5	< 0.5
CTC-CMU match $\Delta x(cm)$	< 2.0	< 2.0	-	-
or CTC-CMU match χ^2	< 9.0	< 9.0	-	-
CTC- CMP match $\Delta x(cm)$	< 5.0	< 5.0	-	-
or CTC-CMP match χ^2	< 9.0	< 9.0	-	-
CTC-CMX match $\Delta x(cm)$	-	-	< 5.0	-
or CTC-CMX match χ^2	-	-	< 9.0	-
Good track	yes	yes	yes	yes
Valid HTDC	yes	yes	yes	yes
ΔHTDC(ns)	< 10	< 10	< 10	< 10
Not BacToBack	yes	yes	yes	yes
$ISO^{trk}_{0.4}$ (GeV/c)	< 4	< 4	< 4	< 4
Fiducial Check	yes	yes	yes	-

of a partner within the CMUO and CMIO banks that is very much back-to-back ($\Delta\phi(\mu_1,\mu_2) \leq 2^\circ$ and $\Delta\eta(\mu_1,\mu_2) \leq 0.2$). If such a partner was found, the event has been eliminated.

8.2. Dilepton Selection

First we scan over all lepton candidates in the event and we determine what category they belong to. If a candidate lepton is neither a tight or loose lepton it is rejected from further consideration. We find the most energetic tight lepton[3] and we call it the *first* lepton of the event. Then we take the most energetic lepton out of the remaining tight and loose leptons[4]. We check if it comes from the same vertex as the first lepton ($\Delta z(l_1, l_2) \leq 10.0$ cm). We also check if it is well separated from the first lepton ($\Delta R(l_1, l_2) \geq 0.4$ in the $\eta - \phi$ plane). If both of these requirements are met, we call this lepton the *second* lepton of the event. If an event does not have at least one first and at least one second lepton, it is rejected.

8.3. Jet Selection and the Missing Transverse Energy Cut

Previously, in Sec. 7.6 we listed the variables that identify jets. We also defined the missing transverse energy $\not\!\!E_T$ of an event. In our dilepton data we require the presence of at least one jet with energy $E_T \geq 15$ GeV detected in the central region of the detector. Tab. 8.3 lists the cuts placed on the jet identification variables. If no jet satisfying requirements in Tab. 8.3 is found, the event is disregarded. Similarly, we require that the event has $\not\!\!E_T \geq 15$ GeV. If the $\not\!\!E_T$ is smaller, the event is disregarded.

[3] If an event does not have a TCE or TCM, it is rejected.

[4] If there is none, the event is rejected.

Table 8.3
Jet identification cuts. The $|\eta|$ coordinate is measured from the origin of the detector.

	Central Jet
Uncorrected E_T (GeV)	> 10
Corrected E_T (GeV)	> 15
Detector $\|\eta\|$	< 1.1
Charge fraction	< 0.1
$\Delta R(l_1, jet)$ in $\eta - \phi$ plane	> 0.7
$\Delta R(l_2, jet)$ in $\eta - \phi$ plane	> 0.7

9. Data Samples

9.1. The Run 1A SUSY Dilepton Sample

During Run 1A, a set of about *3.7 million electron* and about *2.7 million muon* events were collected by online triggers and written to the *Inclusive electron* and *Inclusive muon* samples. These samples were created with rather low p_T lepton trigger thresholds. They contain a significant fraction of misidentified leptons. Such leptons are not of interest to us when searching for SUSY, we reduce their fraction by placing more stringent lepton identification cuts as listed in Appendix Tab. F.1. By applying the dilepton finding procedure described in Sec. 8, we create a general dilepton sample that has been used in previous SUSY searches. Note that the lepton p_T thresholds were $E_T(\text{TCE}) \geq 7.5$ GeV and $E_T(\text{LCE}) \geq 4.0$ GeV, $p_T(\text{TCM}) \geq 7.5$ GeV/c and $p_T(\text{LCM}) \geq 2.8$ GeV/c. **58,221 events** passed such a selection and they define the **Run 1A SUSY dilepton sample**[1]. These events make our Run 1A starting sample which we will use to search for the stop quark. The total integrated luminosity[42, 43] of this Run 1A sample is $\int \mathcal{L}dt = 18.6 \pm 0.7\ \text{pb}^{-1}$.

9.2. The Run 1B SUSY Dilepton Sample

During Run 1B, the *low* p_T *single electron*, the *low* p_T *single muon* and the *special SUSY dilepton* level 2 triggers passed events to the level 3 *Combined Exotic Dilepton* trigger[2]. A total of 3,270,488 events were collected and written to 8mm tapes[3] creating

[1] These events were written to tape RK5855 into z4*.stp1_3p files.

[2] The Combined Exotic Dilepton Trigger (COMBINED_EXOB_DIL) combined three stream B exotic triggers, EXOB_DIL_TOP*, EXOB_DIL_EWK* and EXOB_DIL_EXO*

[3] For the list of the tapes see [42].

the *Exotic Dilepton Dataset*[4]. Similarly, as in Run 1A, the CDF SUSY working group further decreased the misidentified lepton contamination of these events and selected the **Run 1B SUSY Dilepton Sample**. The dilepton finding procedure described in Sec.8 was applied but with lepton identification cuts listed in Appendix Tab. F.2. Note that the lepton p_T thresholds were $E_T(TCE) \geq 8$ GeV and $E_T(LCE) \geq 4.0$ GeV, $p_T(TCM) \geq 7.5$ GeV/c and $p_T(LCM) \geq 1.4$ GeV/c. This selection reduced the 3,270,488 events of the Exotic Dilepton Dataset to **457,478** events. These events constitute the **Run 1B SUSY Dilepton Sample**[5] which is the RUN 1B starting sample for our stop search. More details of this selection can be found in [44, 42]. The total integrated luminosity of this sample[42] is $\int \mathcal{L}dt = 88.62 \pm 3.6$ pb^{-1}.

9.3. Further Cleanup of the Search Data

It turns out that both Run 1A and Run 1B SUSY dilepton samples still contain a significant fraction of events that are clearly not candidates for being stop quark originated. In this section we describe further "cleanup" of our data in order to increase its purity.

We start applying the dilepton event selection described in Sec.8 with our more stringent stop search lepton identification cuts listed in Tab. 8.1 and Tab. 8.2. After this selection, each event contains an isolated tight lepton with $p_T \geq 10$ GeV and at least one isolated loose lepton with $p_T \geq 6$ GeV. These leptons are well separated from each other and were detected in the central region of the detector. Then we searched each event for the existence of a good quality vertex near the two leptons. A good vertex is a vertex of class of at least 10, and located within 60 cm of the origin. The vertex must also be within 10 cm of the mean of the z-coordinates of the two leptons. So far our dilepton sample still contains e^+e^- or $\mu^+\mu^-$ events that could originate

[4]Later we will see that into the Exotic Dilepton Dataset a small amount of events (called volunteers) passing some other L3 triggers (such as the low p_T muon or low p_T electron or some missing E_T triggers) infiltrated as well. We show the trigger spectrum of the search sample in Appendix E.

[5]These events were recorded on eight, 8 mm tapes RK8876, RK8895, RK8921, RK8880, RK8897, RK9198, RK8885, RK8899

from the J/Ψ, Υ or the Z boson. The sample still contains events with pairs of low p_T leptons from the cascade decays of heavy quarks (such as bottom or charm). Such events are not of interest in our search and we identify and remove them from the sample. This is done with the help of the invariant mass of the lepton pair. The low mass neutral resonances are addressed by removing all events whose first and second lepton has the same lepton flavor and $m(l_1, l_2) < 12$ GeV/c^2 , where the invariant mass is defined by the relation $m(l_1, l_2) = \sqrt{(E(l_1) + E(l_2))^2 - |\vec{p}(l_1) + \vec{p}(l_2)|^2}$. In case of the Z boson, we place a dilepton mass window cut $76 \leq m(l_1, l_2) \leq 106$ GeV/c^2 if the leptons have the same flavor. The leptons from cascade decays of heavy quarks usually form low dilepton mass pairs, and we address them by requiring $m(l_1, l_2) <$ 6 GeV/c^2 regardless of their flavor [6]. A total of 6,763 events passed our cleanup cuts. Tab. 9.1 summarizes the effect of the cleanup cuts on the Run 1A and Run 1B data.

9.3.1. Leptonic Triggers Yielding Data for Stop Search

The CDF data taking structure is such, that a number of lower level triggers select and pass data to higher level triggers. The events' leptons, jets or missing energy usually activate more than one trigger. It is then natural, that any data set contains events which could have been recored via multiple trigger paths. This makes it later more difficult (if not impossible) to properly correct the results of Monte Carlo simulations for efficiencies of data collecting triggers. In searches for new phenomena, it is crucial to be able to compare the seen data with already known (expected) Standard Model processes. Therefore, it is common to restrict ourselves to data passing only those triggers, whose efficiencies are well known[7]. Then the Monte Carlo simulations will be properly adjusted, compared to observed data and

[6] We place the dilepton mass cuts regardless of the electric charge sign of the entering pairs.

[7] Naturally, when searching for exotic physics, one does not want to exclude any data from consideration just because it came through a complicated trigger. But when no new phenomena exhibits itself in the data, comparison of theoretical predictions to data passing well understood trigger paths is necessary. Therefore in the actual stop search, we use the whole cleaned up sample, while for setting limits we restrict ourself to well simulated and understood trigger paths.

if necessary, upper limits on the number of events originated in new physics in the data can be set. Tables G.1-G.3 and Tabs. G.4-G.6 list the level 1, 2 and 3 triggers we require our data to have passed. Triggers of the same level are logically "`OR`"-ed. Triggers of different levels are logically "`AND`"-ed. This means, an event is kept if it passed at least one of the listed level 1 triggers and at least one of the level 2 triggers and at least one of the level 3 triggers.

For completeness we also show some other existing active triggers which also passed some data to the SUSY dilepton dataset. These data will be included in our search for the stop, but will not be included in the limit settings. The first row of the above mentioned tables shows the number of events passing the listed trigger. Then recursively, the i-th row indicates the number of events passing its listed trigger but not passing the trigger listed on the $(i-1)$-st row. For completeness also show the number of events that did not come through any of the listed triggers.

Table 9.1 summarizes the number of events that passed the "required" triggers of Tabs. G.1-G.3 and Tabs. G.4-G.6. Only approximately 15% of the total data came through triggers other than the ones marked as "required".

9.3.2. Data at Preselection: Two Leptons, Jets, and Missing E_T

The stop signal would manifest itself in the data not only by the presence of two opposite charge sign leptons, but also by having a jet (from a b or c quark) and significant missing energy. We apply the jet reconstruction and identification procedure described in Secs. 7.6 and 8.3 and we only keep events with at least one central jet with the cone 0.7. The jets are required to be well separated from leptons. Due to detector escaping sneutrinos in the stop events, we also require that each event contains at least 15 GeV corrected missing transverse energy. Tab. 9.1 shows the number of events still remaining in the data sample after the jet and missing energy cuts were applied. A total of 176 events passed these preselection cuts.

Table 9.1
Summary of Run 1A and Run 1B data events remaining in the search sample at the preselection stage.

Applied Cuts		Run 1A				Run 1B			
SUSY dilepton sample		58,221				457,478			
Stop search lept ID		2,187				11,108			
Cleanup Cuts	Good Vertex	2,090				10,425			
	$m(l_1, l_2) \geq 6$ GeV	2,039				10,158			
	$m(ee$ or $\mu\mu) \geq 12$ GeV	1,871				9,262			
	Z^0 removal	1,161				5,602			
Trigger Path		No		Yes		No		Yes	
		1,161		945		5,602		4,489	
At least 1 Jet		169		136		812		850	
$\not\!\!E_T \geq 15$ GeV		29		23		185		153	
		OS	LS	**OS**	LS	**OS**	LS	**OS**	LS
		27	2	**22**	1	**126**	59	**106**	47

10. Background Processes

The detection of the stop signal is based on searching for events which contain at least two opposite charge leptons, jets and a significant missing transverse energy. There are however also non-SUSY processes with a similar signature. Very often they lead to a significant amount of background from which the stop signal has to be extracted.

10.1. Standard Model Background

The main Standard Model processes mimicking the stop signal signature are:

- Heavy flavor production:
  - Production of $b\bar{b}$ and $c\bar{c}$ quarks (see Fig. 10.1) and their semileptonic decays.
  - $t\bar{t}$ production (see diagrams in Fig. 4.1 and substitute top instead of stop quarks) and their leptonic decays.
- Higher order Drell-Yan plus jets events (direct production of lepton pairs, see Fig. 10.2).
- Production of WW, WZ, ZZ (see Fig. 10.3) and their decays.

10.1.1. Heavy Flavor Production

The $t\bar{t}$ events look very similar to $\tilde{t}\bar{\tilde{t}}$ events. The electroweak decay of the top quark produces a b quark and an on-shell W boson, which can then decay to a lepton and a neutrino. Similarly for the $b\bar{b}$ or $c\bar{c}$ events with the leptons coming from the semileptonic decays of these quarks[1]. The jets are mostly from initial or final state

[1] The W boson is off-shell.

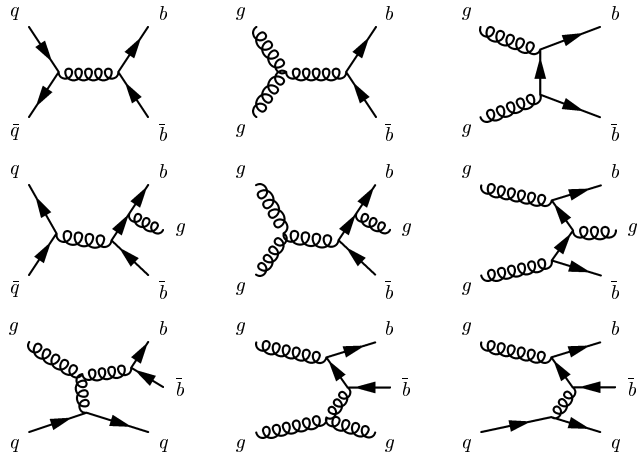

Figure 10.1. Leading, and some higher order $b\bar{b}$ plus jet productions diagrams. The $c\bar{c}$ production is obtained by replacing $b \to c$.

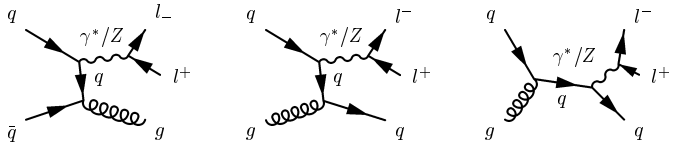

Figure 10.2. Some higher order Drell-Yan plus jet processes.

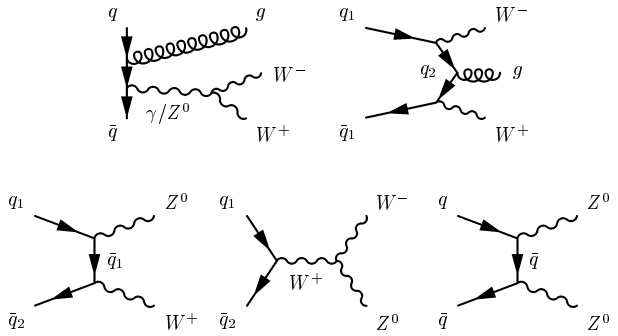

Figure 10.3. Some higher order weak diboson production diagrams.

radiation, and the missing energy is coming from the neutrinos of the semileptonic decays or mismeasurement of the jets' and leptons' energy. There are some significant difference between the heavy $t\bar{t}$ and the lighter $b\bar{b}$ and $c\bar{c}$ cases.

1. The $b\bar{b}$ or $c\bar{c}$ processes have a very high production cross section ($\sigma(b\bar{b}) \approx 10^6$ pb) while the top quark production cross section is quite small ($\sigma(t\bar{t}) \approx 5$ pb).

2. The directly produced b and c quarks (given their very small mass) have a very very large Lorentz boost which means that their semileptonic decay products are extremely well collimated along the parent quark momentum axis. The heavy t quarks are produced rather slow and their decay products can spread almost over the whole solid angle, which means they are highly separated from each other. The stop signal is similar to the top quark events in this sense. The stop decay products are also very well isolated. After placing a cut on the lepton isolation variable, the $b\bar{b}$ and $c\bar{c}$ events have very low passing efficiencies.

3. The last mentioned, but probably the biggest difference between the $b\bar{b}$ or $c\bar{c}$ and the $\bar{t}t$ decays is the amount of transfered energy during the decay. For example when a b quark decays, there is approximately 4.5 GeV available energy. When the t quark decays it releases at least 175 GeV. This difference very much affects the momentum of the produced leptons. In the case of the $b \to cl\bar{\nu}$ the c quark takes almost all the momentum, which means that it is extremely difficult to produce high momentum leptons via the semileptonic decays of b-quarks. The probability that a lepton with a given momentum is produced in the b decays is described by the fragmentation function. It has a steeply falling shape as the momentum of the lepton rises. In case of the top quark decay, it is the heavy real W which takes a huge part of the t quark's momentum. When the W decays, it leaves behind very energetic leptons and neutrinos. Therefore, the semileptonic b (or c) decay products are far less energetic than the ones coming from the t decays. Applying this to neutrinos, $b\bar{b}$ and $c\bar{c}$ events are expected to have very little missing transverse energy.

The combination of above leads us to the conclusion that the $b\bar{b}$ and $c\bar{c}$ will be less significant background than the $t\bar{t}$. Note also that the events coming from the stop signal are in general expected to contain softer leptons, and jets than the top quark events. This is because the considered stop masses in our search are significantly lower than the top mass. The sneutrinos of the stop decay generally take away substantial energy from the event leaving less available for the leptons and jets.

10.1.2. Drell-Yan Process

The Drell-Yan process is direct lepton-antilepton pair production. The proton's and antiproton's quark constituents annihilate into a photon γ or a Z^0 boson (both virtual or real) which then split into lepton-antilepton pair.

$$\bar{q}q \to \gamma \to l^+l^- \qquad \bar{q}q \to Z^0 \to l^+l^- \tag{10.1}$$

The leading order diagrams produce only two leptons. However, the higher order QCD processes shown on Fig. 10.2 can produce jets as well.

Mismeasured energies of jets and leptons or the escaping neutrinos from $\tau^{\pm}$ decays can cause an energy imbalance in the detector yielding Drell-Yan events with substantial missing transverse energy ($\not\!\!E_{\rm T}$).

10.1.3. Diboson Background

In the proton antiproton collisions, diboson pairs such as WW, WZ, ZZ are created. As shown in Fig. 10.3. In the case of WW pair production, higher order QCD processes add jets to the events, and the weak boson decays provide the leptons and the neutrinos. It is also possible to get two leptons and a jet from WZ production. The decay of the Z boson provides the two leptons and the hadronic decay of the W boson then gives the hadronic jets. The mismeasurement of the jet energies gives rise to the missing energy of the events. In ZZ production, the leptonic decay of one of the Z bosons and the hadronic decay of the other one provides the two-lepton

plus jets signature. The missing transverse energy could in principle come again from jet or lepton energy mismeasurements or neutrinos from W or Z decays or τ-lepton originated neutrinos.

In Sec. 11 we will give a quantitative estimate of the expected Standard Model background based on the Monte Carlo simulation technique.

10.2. Background from Misidentified Leptons

10.2.1. Overall Strategy

In the previous section we introduced the Standard Model predicted "prompt" lepton contributions to our dilepton search sample. By prompt leptons we mean central electrons or muons from Drell-Yan processes, or from $b\bar{b}$, $c\bar{c}$, $t\bar{t}$, WW,WZ, or ZZ decays. Every other object found in an event that passes the lepton identification cuts listed in Tab. 8.1 and Tab. 8.2 is classified as a non-prompt, misidentified, or fake lepton.

The searched dilepton sample has an asymmetric p_T requirement for the tight ($p_T \geq 10$ GeV) and loose ($p_T \geq 6$ GeV) lepton. The tracks of events have a steeply falling p_T spectrum as their momentum increases. This means that there are many fewer tracks above 10 GeV/c^2 to be misidentified as a lepton than tracks between 6 and 10 GeV/c^2 . Since the rate of misidentification does not rise steeply with rising p_T , the tight lepton is most likely to be a genuine lepton and the loose lepton has the greater chance to be the fake lepton.

Previous studies [45, 46, 47] estimated the lepton misidentification rates. These studies report both event and track-based fake rates. The event-based studies are useful to estimate an upper limit on the contribution of the misidentified leptons when it is expected to be small. However, their disadvantage is that no topological cuts involving misidentified leptons can be applied when the misidentification rate is considerable. When event-based fake rates are used, it is necessary to ensure that the

number of tracks per event of the sample to which the rates are applied is similar to the one on which the rates were determined.

For studies of events rich in tracks a more detailed approach, the track based approach, is necessary. We fully exploit the advantage of the track based approach to get the most detailed information on the misidentified lepton. Although supersymmetric processes are produced at high Q^2, the escaping lightest supersymmetric particles and neutrinos can make them look like processes at much lower Q^2, and thus difficult to distinguish from misidentified lepton events without using kinematic (topological) quantities.

In our track-based study, we do not only determine the probability that a track is misidentified as a lepton, but we go one step further: we simulate the behavior of misidentified leptons, and by using topological cuts we substantially lower their contribution to the dilepton sample. Our study of misidentified leptons has two parts:

1. **Determination of the momentum dependent probability (fake rate) i.e. the probability that a track of a certain p_T is misidentified as a lepton passing identification criteria.**

   In order to do this, we have to choose a data set from which we want to measure the misidentification rates. We can choose a data sample which has no significant contribution of prompt leptons; we can equally well choose a data sample where the prompt leptons can be easily identified and removed on an event-by-event basis; or we can choose a sample where the prompt lepton contribution can be factored out on a statistical basis.

   Then we want to determine the momentum dependent misidentification rates. In each momentum bin we determine the total number of tracks that potentially had a chance to be misidentified as leptons. We then count the fake lepton candidates which pass the given loose lepton IDs (Tab. 8.1 and Tab. 8.2). The

ratio of the number of found fake lepton candidates to the number of found tracks represents the probability that a track could be misidentified as a lepton.

2. **Application of the measured fake rates to tracks of the single lepton data sample in order to estimate the contribution of fakes to the dilepton stop search sample.**

   Each event of the single lepton sample is searched for a lepton passing the tight lepton cuts listed in Tab. 8.1 and Tab. 8.2. We then treat every additional track in the event not associated with any lepton candidate as a track which potentially could have faked a lepton. With each such track we associate a simulated lepton with properties passing the loose lepton ID cuts of Tab. 8.1 and Tab. 8.2. This will be our fake lepton. We obtain an "lepton plus a fake-lepton" event to which we assign a weight proportional to the fake rate[2] based on the p_T of the fake lepton's track. Such "lepton plus a fake-lepton" event is then passed through the analysis program and is considered as one of the backgrounds to our SUSY search.

Before we get too technical, let us spend a minute on the origin of the fakes.

10.2.2. Origin of Misidentified Leptons and Data Samples for Fake Rates Studies

Misidentified leptons could have both leptonic or non-leptonic origin as long as they pass the required loose lepton identification cuts.

- Misidentified leptons of non-leptonic origin:
  - Jets which deposit substantial energy in the EM calorimeter and have a stiff track associated with them can be identified as electrons.
  - Hadronic jets with late showers which leak out of the hadron calorimeter into the muon chambers can be identified as muons. (For example, punchthroughs of pions and kaons [48]).

[2]Scaled to the proper luminosity.

- Misidentified leptons of leptonic origin:
  - Non-prompt leptons (not originating in the hard scattering) such as decay in flight of kaons and pions to muons [49]
  - Prompt leptons coming from light quark and gluon jets

Several data samples can be chosen to extract the misidentification rates. For example:

- Samples with no significant prompt lepton contribution:
  - Minimum Bias (MinBias) Trigger Sample: Due to the large cross section of Minimum Bias events with respect to processes yielding leptons, the sample is essentially free of prompt leptons.
- Samples where prompt leptons can be removed on an event by event basis:
  - J/ψ sample: The leptons from J/ψ decays are excluded from consideration as fake candidates.
  - W, Z sample: Leptons from W and Z decays are excluded from the misidentified lepton search. In addition, the content of possible prompt leptons in the samples needs to be estimated and excluded before counting the fake candidates.
- Samples where prompt leptons can be removed on a statistical basis:
  - Jet samples: samples of events which passed a 20 GeV or 50 GeV jet trigger (see [50]). They are rich in statistics, and contain many tracks in each event. If a lepton is present, it is most likely a fake or has a heavy flavor quark origin, but due to large cross section of hadron processes contributing to these samples the prompt lepton contribution is very small. It is necessary to remove the trigger bias when choosing these samples to study the fake rates.

In the next section we describe the details of how we extract the lepton misidentification rates from the Minimum Bias Trigger Sample and from the Jet50 Sample.

10.2.3. Fake Leptons in the Minimum Bias and Jet50 Samples

Minimum Bias Sample

The Minimum Bias data set is a set of events triggered[3] by the beam-beam counters (BBC). Due to high production cross section (about 50 mb) and limited data storage possibilities, the triggers were heavily prescaled. The Minimum Bias data sample is therefore well suited for fake lepton studies We first estimate the number of prompt leptons expected from heavy flavor decays. The CDF published cross section of the MinBias events is about 50 mb [51]. The CDF published B cross section is of the order of 3μb [52]. The B decay branching ratio to leptons is about 20%. Similarly for the charm contribution. This allows us to estimate that the heavy flavor originating prompt leptons in MinBias is $\frac{2*0.2*3\mu b}{50{,}000\mu b}$. As we will see later, there are approximately 70,000 tracks in the sample which could have faked a loose lepton, therefore we estimate that less than one prompt lepton in the MinBias sample has a heavy flavor origin. In other words, due to the high Minimum Bias production cross section in comparison to the cross section of prompt lepton leading processes the Minimum Bias sample is essentially prompt lepton free. Therefore any lepton passing our loose central electron or loose central muon identification cuts (listed in Tab. 8.1 and Tab. 8.2) and found in the MinBias sample is categorized as a fake lepton. We define five categories of fake leptons. The CEM, CMU ONLY, CMP ONLY, CMU AND CMP, and CMX categories[4]. The p_T's of fake electrons and muons found in the MinBias sample are listed in Tabs. 10.1-10.5 and plotted on Figs. 10.4-10.8.

[3]Events are required to pass the YMON, YMON, OTHB_MIN_BIAS level 1, 2 and 3 triggers respectively and the runs must be recorded in the production manager database in order to be considered.
[4]In case of muons, the "ONLY" means that the muon hit only the listed chamber. The "AND" means the muon had a hit in both of the involved muon chambers.

Jet50 Sample

The Jet50 sample is a set of events[5] which contain at least one cluster with more than 50 GeV energy. Sometimes the choice of the triggers introduces some "bias" of the taken data. We do not want this bias to be propagated to our objects of interest. We remove any potential trigger bias by requiring that each event contains at least one additional cluster with energy of more than 50 GeV. We also remove any Z^0 +X and $W^{\pm}$+X events by using the mass window cuts of $76 \leq m(l_1, l_2) \leq 106$ GeV/c^2 and $40 \leq m_T(l, \not\!\!E_{\rm T}) \leq 100$ GeV respectively. The heavy flavor originated lepton contributions is estimated to be small based on the production cross section of events containing b or c quarks capable of creating a 50 GeV trigger cluster. The $b\bar{b}$ production cross section for b-quark momentum larger then 50 GeV/c is estimated to be less than 0.1 nb [53]. The total integrated luminosity of the Jet50 sample we used for studies of fakes is about 70 pb^{-1}. The Jet50 trigger had a 40 fold level 1 prescale applied when data were taken. The branching ratio of b decaying to leptons is about 20 %. Therefore, the inclusive number of leptons expected to contribute to the Jet 50 sample is about $\frac{100*70*0.2*0.5*0.25}{40} = 4$ events, where we further include a 50% efficiency for this lepton being above the 6 GeV/c threshold, and about 25% efficiency for the lepton being isolated. We obtained about 4 events of heavy flavor origin leptons contamining the ensemble of about 200 found fake leptons in the Jet50 sample. This is a small, $\approx$4% effect negligible with respect the total systematic uncertainties of the fake determination as we will see later. After the above cleanups, any lepton found passing our loose central electron and loose central muon identification cuts listed in Tab. 8.1 and Tab. 8.2 in the Jet50 sample will be categorized as a fake lepton. The p_T's of fake electrons and muons found in the Jet50 sample are listed in Tabs. 10.1-10.5 and plotted on Figs. 10.4-10.8.

[5]Events are required to pass the L1_4_PRESCALE, JET_50, QCDB_JET3_50 level 1, 2 and 3 triggers respectively and the runs must be recorded in the production manager database in order to be considered.

10.2.4. Track based Fake Rates

Having identified the fake leptons in the MinBias and Jet50 samples, we proceed to determine their fake rates. *We want to find the* p_T *dependent probability* $\mathcal{P}$*, that a track with a given* p_T *is misidentified as a loose lepton* (with ID listed in Tab. 8.1 and Tab. 8.2). In order to find these probabilities, we need to know the p_T distribution of all the tracks present in the event. Out of these, we count only the ones which point to the appropriate regions of the detector[6]. Tracks are required to be of good quality (as defined in Sec. 7.4.3) and above 3 GeV/c (5 GeV/c) threshold for electrons (muons). Figs. 10.4-10.8 show the p_T distribution of the central EM calorimeter tracks, and various muon chambers pointing tracks. Tabs. 10.1-10.5 show the content of the various p_T bins explicitly. The assigned error bars of the bin contents are the standard statistical $\sqrt{N}$ errors.

The fake rate $\mathcal{P}^i(p_T)$ for each of the previously mentioned five categories of loose leptons is then defined by:

$$\mathcal{P}^i_{\text{lepton}}(p_T) = \frac{N^i_{\text{lepton}}(p_T)}{N^i_{\text{tracks}}(p_T)},$$

where $\mathcal{P}^i_{\text{lepton}}(p_T)$ is the probability that a track with a p_T from the i-th p_T bin fakes a lepton (with lepton ID's defined in Tab. 8.1 and Tab. 8.2), $N^i_{\text{lepton}}(p_T)$ is the number of fake leptons found with p_T in the i-th p_T bin, and $N^i_{\text{tracks}}(p_T)$ is the number of tracks with p_T in the i-th p_T bin.

Figs. 10.4-10.8 show the fake rates found from the MinBias and Jet50 samples. Tabs. 10.1-10.5 contain the lepton misidentification probabilities plotted in the above mentioned figures. In each p_T bin, the uncertainties on the fake rates were calculated by adding in quadrature the statistical uncertainties $\frac{\sqrt{N}}{N}$ of the number of fakes and the number of tracks. The 1-sigma uncertainty band is shown in the fake rate figures as well. We conclude that within the statistical uncertainties the fake rates of CEM, CMU and CMP, and CMX leptons found in the two samples agree very well.

[6]For example if a track points to the plug region it will not be counted as a possible track able to fake a central electron. But if it points to a region covered by both CEM and CMU, it will be counted as able to fake both a loose central electron and a loose central muon.

Table 10.1
Fake CEM objects passing the loose electron ID cuts (see Tab. 8.1), tracks pointing to CEM calorimeters and the electron fake rates from Jet50 and MinBias samples. This is a table version of Fig. 10.4.

	Minimum Bias Sample			Jet50 Sample		
p_T (GeV/c)	Fake CEM t	CEM pointing tracks	CEM Fake Rate x1000	Fake CEM t	CEM pointing tracks	CEM Fake Rate x1000
3-4	1± 1.0	38,743± 197	0 .0 ± 0.0	11± 3.3	47,674± 218	0 .2 ± 0.07
4-5	4± 2.0	9,593± 98	0.4 ± 0.2	15± 3.9	20,346± 142	0 .7 ± 0.2
5-6	5± 2.2	2,906 ± 54	1.7 ± 0.8	38± 6.2	10,683± 103	3.6 ± 0.6
6-7	5 ± 2.2	1,068± 33	4.7 ± 2.1	26± 5.1	6,193± 79	4.2 ± 0.8
7-8	3 ± 1.7	464 ± 22	4.3 ± 3.0	20± 4.5	3,939± 63	5.1 ± 1.1
8-9	3± 1.7	483 ± 22	6.3 ± 3.6	18± 4.2	2,810± 53	6.4± 1.5
9-10	3± 1.7	483 ± 22	6.3 ± 3.6	9 ± 3.0	1,948± 44	4.6± 1.5
10-11	3± 1.7	483 ± 22	6.3 ± 3.6	8 ± 2.8	1,504± 39	5.3± 1.9
≥ 11	3± 2.8	483 ± 22	6.3 ± 3.6	33± 5.7	7,578± 87	4.4± 0.8

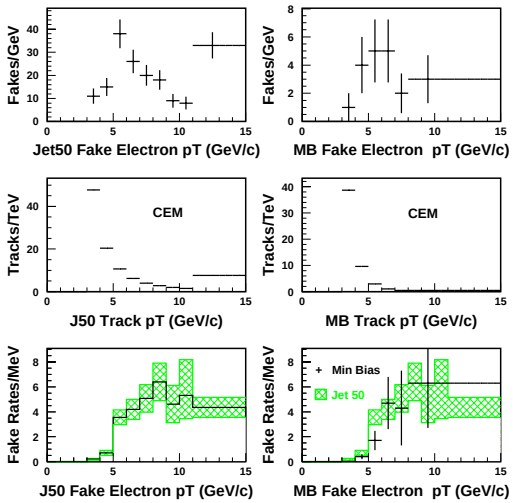

Figure 10.4. The p_T of fake CEM objects, tracks pointing to CEM calorimeters, and electron fake rates from Jet50 (left) and MinBias samples (right). The lowest right picture also compares the MinBias fake rates with the Jet50 ones.

Table 10.2
Fake CMU .AND. CMP objects (hitting both the CMU and CMP chambers and passing the loose muon ID cuts, see Tab. 8.2), tracks pointing to both CMU and CMP chambers, and muon fake rates from Jet50 and MinBias samples. This is a table version of Fig. 10.5.

	Minimum Bias Sample			Jet50 Sample		
p_T (GeV/c)	Fake LCMU	CMU/CMP pointing tracks	LCMU Fake Rate x1000	Fake LCMU	CMU/CMP pointing tracks	LCMU Fake Rate x1000
5-6	7± 2.6	922 ± 30	7.6 ± 2.8	26± 5.1	3,099± 56	8.4 ± 1.6
6-7	4 ± 2.0	341± 18	11.7± 5.9	12± 3.5	1,720± 41	7.0 ± 2.0
7-8	2 ± 1.4	281 ± 17	7.1 ± 5.0	6 ± 2.4	1,104± 33	5.4 ± 2.2
8-9	2± 1.4	281 ± 17	7.1 ± 5.0	6 ± 2.4	771± 28	7.8± 3.1
9-10	2± 1.4	281 ± 17	7.1 ± 5.0	6 ± 2.4	540± 23	11.1± 4.4
10-11	2± 1.4	281 ± 17	7.1 ± 5.0	6 ± 2.4	465± 22	12.9± 5.2
≥ 11	2± 1.4	281 ± 17	7.1 ± 5.0	6 ± 2.4	2,217± 47	2.7± 1.1

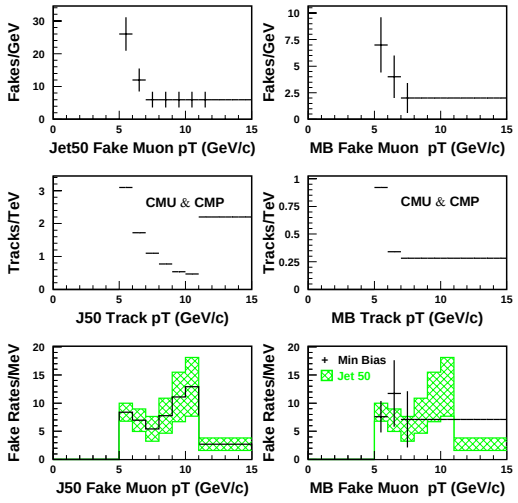

Figure 10.5. The p_T distribution of fake CMU .AND. CMP objects, tracks pointing to CMU and CMP chambers, and the muon fake rates from Jet50 (left) and MinBias samples (right). The lowest right picture also compares the MinBias fake rates with the Jet50 ones.

Table 10.3
Fake CMX objects (passing the loose muon ID cuts, see Tab. 8.2), tracks pointing to CMX chamber, and CMX muon fake rates from Jet50 and MinBias samples. This is a table version of Fig. 10.6.

	Minimum Bias Sample			Jet50 Sample		
p_T (GeV/c)	Fake LCMX	CMX pointing tracks	LCMX Fake Rate x1000	Fake LCMX	CMX pointing tracks	LCMX Fake Rate x1000
5-6	9± 3.0	585 ± 24	15.4 ± 5.1	32± 5.7	2,221± 47	14.4 ± 2.6
6-7	4 ± 2.0	405± 20	9.9 ± 5.0	15± 3.9	1,297± 36	11.6± 3.0
7-8	4 ± 2.0	405 ± 20	9.9 ± 5.0	9± 3.0	854± 29	10.5 ± 3.5
8-9	4± 2.0	405 ± 20	9.9 ± 5.0	4± 2.0	588± 24	6.8± 3.4
9-10	4± 2.0	405 ± 20	9.9 ± 5.0	4 ± 2.0	424± 21	9.4± 4.7
10-11	4± 2.0	405 ± 20	9.9 ± 5.0	4 ± 2.0	312 ± 18	12.8± 6.4
$\geq$ 11	4± 2.0	405 ± 20	9.9 ± 5.0	6± 2.4	1,542± 39	3.9± 1.6

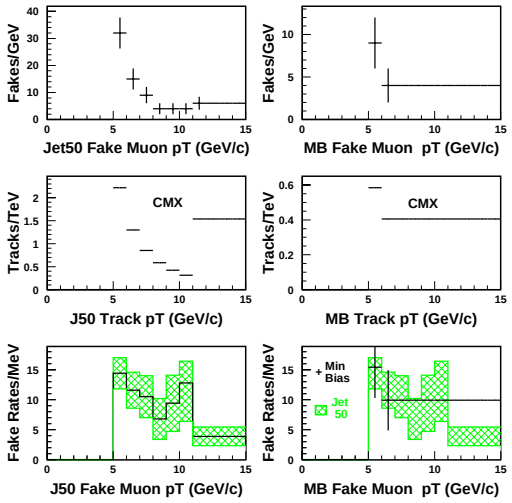

Figure 10.6. The p_T distribution of fake CMX objects, tracks pointing to CMX, and muon fake rates from Jet50 (left) and MinBias samples (right). The lowest right picture also compares the MinBias fake rates with the Jet50 ones.

Table 10.4
Fake CMU objects (objects having only CMU chamber hits and passing the loose muon ID cuts, see Tab. 8.2), tracks pointing to CMU chambers only, and muon fake rates from Jet50 and MinBias samples. This is a table version of Fig. 10.7.

	Minimum Bias Sample			Jet50 Sample		
p_T (GeV/c)	Fake LCMU	CMU pointing tracks	LCMU Fake Rate x1000	Fake LCMU	CMU pointing tracks	LCMU Fake Rate x1000
5-6	31± 5.6	358 ± 19	86 ± 16	58± 7.6	1,297± 36	45 ± 6
6-7	12± 3.5	157± 13	76 ± 22	34± 5.8	805± 28	42 ± 7
7-8	4 ± 2.0	49 ± 7.0	82 ± 41	16± 4.0	426± 21	38 ± 9
8-9	3± 1.7	68 ± 8.2	44 ± 25	18± 4.2	382± 20	47 ± 11
9-10	3± 1.7	68 ± 8.2	44 ± 25	10± 3.2	218± 15	46 ± 15
10-11	3± 1.7	68 ± 8.2	44 ± 25	7 ± 2.6	184 ± 14	38 ± 14
≥ 11	3± 1.7	68 ± 8.2	44 ± 25	10± 3.2	889± 30	11 ± 3.6

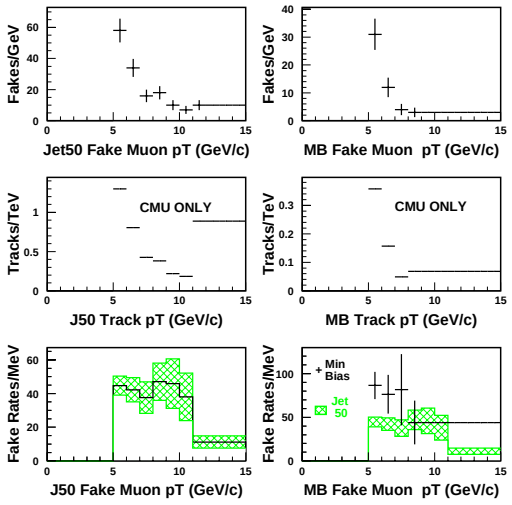

Figure 10.7. The p_T distribution of fake CMU-only objects, tracks pointing to CMU-only chambers, and the muon fake rates from Jet50 (left) and MinBias samples (right). The lowest right picture also compares the MinBias fake rates with the Jet50 ones.

Table 10.5
Fake CMP-only objects (objects having only CMP chamber hits and passing the loose muon ID cuts, see Tab. 8.2), tracks pointing to CMP-only chambers, and the muon fake rates from Jet50 and MinBias samples. This is a table version of Fig. 10.8

	Minimum Bias Sample			Jet50 Sample		
p_T (GeV/c)	Fake LCMP	CMP pointing tracks	LCMP Fake Rate x1000	Fake LCMP	CMP pointing tracks	LCMP Fake Rate x1000
5-6	9± 3.0	286 ± 17	31 ± 10	7± 2.6	942 ± 30	7.4 ± 2.8
≥ 7	2± 1.4	169 ± 13	12 ± 8	5± 2.2	2,245± 47	2.2± 1.0

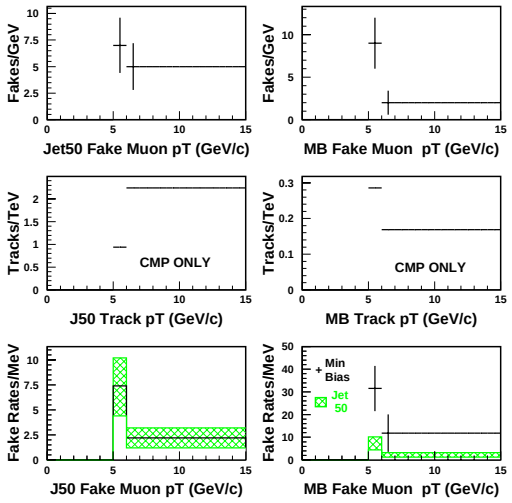

Figure 10.8. The p_T distribution of fake CMP-only objects, tracks pointing to CMP-only chambers, and the muon fake rates from Jet50 (left) and MinBias samples (right). The lowest right picture also compares the MinBias fake rates with the Jet50 ones.

10.2.5. Creating the Lepton Plus Fake-Lepton Sample

In the previous section we studied the probability that a track of a certain p_T is misidentified as a loose lepton. The results of MinBias and Jet50 samples agree within the statistical uncertainties. Since the Jet50 sample has higher overall statistics and covers a larger p_T region, we will use the Jet 50 fake rates. As discussed in Sec. 10.2.1, the next step in estimating the fake lepton contribution to our dilepton data sample is to create a *lepton plus fake-lepton sample*. We start with a total of $\int \mathcal{L}dt = 13.3$ pb^{-1} events of the low p_T single electron and single muon samples. We use runs which belong to both electron and muon samples. We identify events which contain at least one tight lepton (Tab. 8.1 and Tab. 8.2). We further select only events if they have a good track of $p_T \geq 3$ GeV/c pointing to CEM calorimeter or a good track of $p_T \geq 5$ GeV/c pointing to one of the muon chambers. This track must not be associated with any existing lepton in the event. We also make sure that each such a track is originated at the same vertex as the tight lepton ($\Delta z \leq 10cm$) and is well separated from it ($\Delta R > 0.4$ in the $\eta - \phi$ plane). We found a total of **368,570** good tracks with $p_T \geq 3$ GeV/c pointing to the CEM region and **86,716** tracks with $p_T \geq 5$ GeV/c pointing to the CMU, CMP, or CMX chambers. With each such track we associate an electron or a muon that passes our loose lepton identification cuts[7] listed in Tab. 8.1 and Tab. 8.2. This way each lepton passing the tight lepton ID cuts receives a "fake-lepton" partner passing the loose lepton ID cuts. Together they form a "lepton plus fake-lepton event". Such an event is then assigned a weight that is a product of two

[7]The tricky part is to properly associate the E_T of the "would be fake" electron, since the track to which we are assigning the electron bank has only the p_T information. The solution is to use the shape of the distribution of the energy over momentum variable (E/P) of electrons believed to be mostly misidentified. The best fit to our needs would be the low momentum inclusive single electron events. We randomly picked $\approx 100,000$ such events containing at least one electron passing our loose electron ID's listed in Tab. 8.1. On Fig. 10.9 we plot their normalized-to-unity E/P distribution. As the next step we use the FUNLUX CERN library to generate random numbers on the 0.0 to 2.0 interval according to the E/P shape. These random numbers then represent the E/P values and we use them to calculate the most likely deposited E_T from a track with a given p_T ($E_T = p_T * E/P$). Fig. 10.9 shows (as a cross-check) the distribution of the generated random numbers representing the E/P variable. This is in a very good agreement with the original distribution. Note: There are electrons with $E_T \geq 5$ GeV but with $p_T \leq 5$ GeV in real data. In order to accommodate this fact in our fake simulations, we keep generating the E/P values for a given p_T track until its $p_T * E/P$ exceeds the 5 GeV value.

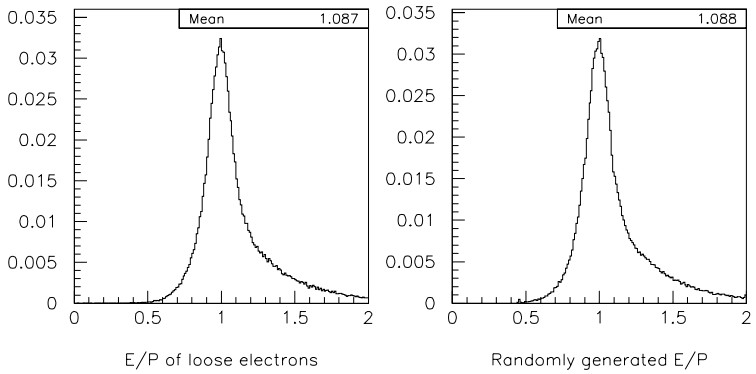

Figure 10.9. The left figure shows the distribution of E/P variable of loose fake electrons from data. The right figure shows the result of the random number generation according to the data distribution shown left.

factors: (1) a scale factor to scale the used integrated luminosity of $\int \mathcal{L}dt = 13.3$ pb^{-1} to the luminosity of the search data sample, (2) a factor corresponding to the fake rate that is based on the p_T of the track and the type of the lepton we are assigning to this track (Tabs. 10.1-10.5). These "lepton plus fake-lepton" events then compose our lepton plus misidentified lepton sample[8]. They are then further analyzed the same way as the other types of background events or the data events themselves.

10.2.6. Fakes at Preselection: Two Leptons, Jets, and Missing E_T

We treat the 'lepton plus fake-lepton" background events exactly the same way as the data events. We apply our dilepton searching algorithm (Sec. 9.3.2), and then we identify jets and require missing transverse energy. Tab. 10.6 summarizes the number of lepton plus a fake-lepton events contributing to the dilepton data sample. A total of 29 events is expected in our search data sample due to misidentified leptons.

[8]For example consider N single lepton events where each contains a lepton passing our tight lepton ID cuts. If each such an event contained two tracks above 5 GeV/c, the created lepton plus fake-lepton sample would have N lepton plus a fake-electron and N lepton plus fake-muon entries. Each such an entry (besides the luminosity scaling) would then receive a weight proportional to the electron or muon misidentification probabilities (Tabs. 10.1-10.5) based on the track's p_T

Table 10.6
Contribution of misidentified leptons to Run 1A and Run 1B search data sample (see Tab. 9.1) at preselection stage.

		Run 1A		Run 1B	
	Stop search lept ID	145		683	
Cleanup Cuts	Good Vertex	138		648	
	$m(l_1, l_2) \geq 6$ GeV	132		620	
	$m(ee,$ or $\mu\mu) \geq 12$ GeV	126		590	
	Z^0 removal	124		583	
	Trigger Path	119		561	
	1 central jet	22		104	
		5		24	
	$\not\!\!E_{\rm T} \geq 15$ GeV	**OS**	LS	**OS**	LS
		2.9	2.2	**13.6**	10.3

11. Monte Carlo Simulations

In search for new phenomena, we look for deviations of observed data from the predictions of the Standard Model. Therefore, it is crucial to know the number of expected signal and signal mimicking background events in the given amount of collected data. It can be calculated from the production cross section of contributing processes and decay branching ratios of the involved particles. However, it is an impossible task to predict the exact values of the kinematic variables characterizing the collision products. Instead, a statistical approach is taken. We use the Monte Carlo technique to obtain a large ensemble of events of various physics processes of interest. From those events we then determine the expected distributions of variables describing the final state of the collision products. The Monte Carlo technique has two stages. The first step is the use of the ISAJET[54] Monte Carlo generator to *generate* large numbers of events (signal and background) of $p\bar{p}$ collisions at $\sqrt{s}$= 1.8 TeV. These events contain detailed information about the collision products and their decays. Each involved particle is characterized by a set of recorded variables, such as the particle's flavor, charge, energy, momentum components *etc.* Also each particle's history (the parent particle's variables) is preserved. The event generator, however, does not take into account various possible detector effects (such as for example energy resolutions of calorimeters). These issues are addressed by a second step, the detector *simulation.* In CDF this is done by the QFL' software. It takes the ISAJET generated events and smears the values of all measurable variables. This smearing is based on the actual detector's performance (which was determined by test beam runs and tuned up by numerous calibrations). After generation and detector simulation of events, we end up with the same set of variables describing a Monte Carlo event as those variables describing collision data. This means that the same methods and software programs can be used to analyze data and Monte Carlo events.

11.1. Efficiency Corrections Applied to Simulated Events

Although QFL's performs a very realistic detector simulation, some specific details of the detector are not completely simulated, thus small corrections, called efficiency corrections still need to be applied to the Monte Carlo events.

11.1.1. Trigger Efficiencies

The lepton triggers responsible for collecting our collision data have various efficiencies which often depend on the momentum of the lepton. This means that when we compare data with Monte Carlo events, not all the MC generated leptons should be counted, even if they satisfy the appropriate lepton identification cuts. The MC results must be corrected for the efficiencies of the triggers. Furthermore, some of the triggers were prescaled due to a high volume of passing data. These prescale factors must be reflected in the trigger efficiency variable as well. In our analysis, we used the same triggers as previous lepton analyses[55] did. The trigger efficiencies (simulated via parameterized turn-on curves as a function of the lepton p_T) of the most important triggers for our dilepton searches (marked as required in Tabs. G.1-G.6) were taken from[55] and references therein. The trigger efficiency corrections of the MC events are determined on an event-by-event basis. We examine each lepton of the event to determine which level 1, level 2 and level 3 triggers it could have most likely activated. Since events usually contain more than one lepton, sometimes there were several possible triggers that could have been activated by events. The efficiency values found for different lepton species within one event, if applicable, are logically "OR"-ed together[1] and this number represents the efficiency(probability) of the event passing this particular trigger level. The efficiencies of different trigger levels are multiplied together and the result represents the total efficiency (probability) that this MC event would have entered the dilepton dataset had it occured in the real

[1]If trigger a and b have ϵ_a and ϵ_b efficiencies, then trigger "a.OR.b" has $\epsilon_a + \epsilon_b - \epsilon_a\epsilon_b$ efficiency.

collision. The statistical weight of each MC event is then multiplied by the trigger efficiency yielding a new weight for the event.

To illustrate the magnitude of these corrections, the typical electron (muon) trigger efficiency is $87.3^{+3.8}_{-4.9}$ % (87.1 ± 2.9 %). See [55]. The quoted uncertainties will be discussed later.

11.1.2. Lepton Identification and Tracking Isolation Efficiencies

Lepton identification (including conversion electron removal, cosmic muon rejection and "good track finding") has its efficiency as well. It reflects the fraction of positively identified leptons. This efficiency is usually different for Monte Carlo and for data events. It is a consequence of the performance of the detector simulation. It tends to overestimate the identification efficiencies due to not having included some subtle detector effects and aging of the detector in its simulation process. These are small effects and are therefore left to be handled by lepton ID efficiency corrections. Each category of leptons receives its own correction factor. We apply the same lepton ID's as previous lepton based analyses and we quote their results of efficiency studies[56]. In tab. 11.1 we summarize the correction factors we apply to MC events. Both the first and the second leptons of each event receive their correction factors. The weight of a Monte Carlo event is then corrected by the product of the tight and loose lepton correction factors.

There were data taking periods in Run 1, when the instantaneous luminosity was high and multiple interactions occured. They affect the isolation of leptons and are not included in the MC, but are handled by applying correction factors (the ratio of MC and data lepton isolation efficiency) to MC events. We adopt the results of previous dilepton analyses[57] that studied the isolation efficiencies of leptons. Tab. 11.2 lists the correction factors we applied (for both tight and loose lepton of the event) to the weight of the signal and background Monte Carlo events.

Table 11.1
Correction factors applied to weights of Monte Carlo events. These correction factors adjust the Monte Carlo lepton identification efficiencies to the ones measured from test data.

	Correction Factors	
Lepton Cathegory	Run 1A	Run 1B
TCE	0.951	0.944
LCE	0.953	0.954
TCM	0.924	0.951
LCM	0.925	0.960
LCX	0.962	0.97
LCI	1.05	1.04

Table 11.2
Correction factors applied to weights of Monte Carlo events. These correction factors adjust the Monte Carlo lepton tracking isolation efficiencies to the ones measured from test data.

Lepton	Correction Factors
Electron	0.996
Muon	0.998

11.2. SUSY Signal Monte Carlo

We use ISAJET with CTEQ-3 [58] parton disribution function (PDF) to generate stop events and to describe the stop quark decay. The ISAJET reported cross section is then corrected to PROSPINO's [59], next-to-leading order results shown in Tab. 11.3. The generated events underwent the full CDF detector simulation done by QFL'.

In order to reduce the statistical uncertainties, we have generated approximatelly 20 to 35 times larger stop signal samples than we would expect in our actual data. This means that the stop signal events will have a weight factor of approximately 0.05

Table 11.3
Next-to-leading order $\tilde{t}$ production cross sections by PROSPINO[59], with CTEQ4M[58].

$m_{\tilde{t}}$ (GeV/c^2)	$\sigma(\tilde{t}\bar{\tilde{t}})$, NLO σ (pb)
80	43.91
90	23.09
95	17.10
100	12.85
105	9.766
110	7.472
115	5.793
120	4.525
125	3.558
130	2.820

by which they would contribute to the searched dilepton sample[2]. Tabs. H.1 summarizes the number of generated events and expected events in $\int \mathcal{L}\mathrm{dt} = 107$ pb^{-1} together with their generated integrated luminosities for various stop and sneutrino mass combinations. None of the above mentioned efficiency corrections, nor any event preselections have been applied yet[3].

11.3. Standard Model Background MC

The background events have been generated with ISAJET with structure functions CTEQ-2, CTEQ-3 [58], MRSD0' [60], GRV_94 [61] and GRV. The generated events went through QFL', the full detector simulation program.

[2]This weight factor is then corrected for the various efficiency corrections factors described in the previous sections.

[3]The last two columns of this table showing the number of expected stop signal events after all selection cuts were applied will be discussed in Sec. 13.

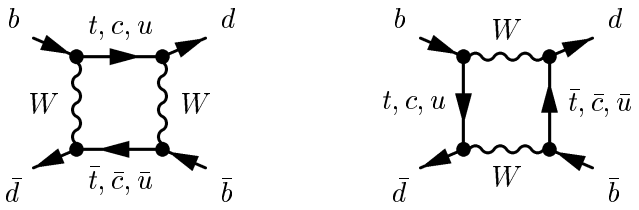

Figure 11.1. Feynman diagrams of $B^0 - \bar{B}^0$ mixing phenomena.

$b\bar{b}$, $c\bar{c}$

The $b\bar{b}$, $c\bar{c}$ yielding processes were generated through the mechanisms shown in Fig.10.1, namely (1) direct production, (2) initial state gluon splitting and (3) final state gluon splitting. When the b-quarks are produced, they quickly hadronize into B mesons, which can decay semileptonically. The B^0 mesons can turn into a $\bar{B}^0$ meson (and vice versa) via the known phenomena of mixing, leading to a lepton of opposite sign to that expected from the MC generator. (see Fig. 11.1). This then means that some of the produced leptons could actually flip their signs if the B meson underwent mixing. The $B^0 - \bar{B}^0$ mixing is not been included into the ISAJET generator, therefore the number of events N_{OS} (N_{LS}) with opposite (like) sign di-leptons must be re-calculated by the use of the mixing parameter χ:

$$\begin{aligned} N_{OS} &= ((1-\chi)^2 + \chi^2) N_{OS}^{ISAJET} + 2\chi(1-\chi) N_{LS}^{ISAJET} \\ N_{LS} &= 2\chi(1-\chi) N_{OS}^{ISAJET} + ((1-\chi)^2 + \chi^2) N_{LS}^{ISAJET} \end{aligned} \tag{11.1}$$

where N_{OS}^{ISAJET}, N_{LS}^{ISAJET} are the number of opposite and like sign events reported by ISAJET and $\chi = 0.118 \pm 0.008 \pm 0.020$ is the CDF measured[62] averaged mixing parameter. After plugging in the χ, we obtain

$$\begin{aligned} N_{OS} &= (0.792 \pm 0.044) N_{OS}^{ISAJET} + (0.208 \pm 0.044) N_{LS}^{ISAJET} \\ N_{LS} &= (0.208 \pm 0.044) N_{OS}^{ISAJET} + (0.792 \pm 0.044) N_{LS}^{ISAJET} \end{aligned} \tag{11.2}$$

Drell-Yan

The Drell-Yan plus jet events have been generated through mechanisms shown on

Fig. 10.2 We have generated a sample more than 20 times larger than our search data sample. The high mass Drell-Yan events (where Z^0 is the mediator) were compared to the $Z^0 \rightarrow e^+e^-$ and $Z^0 \rightarrow \mu^+\mu^-$ CDF datasets. The ISAJET cross section with the leptonic branching ratios enfolded ($\sigma.Br(Z^0 \rightarrow l^+l^-)$) was corrected for the CDF published measurement ($\sigma.Br(Z^0 \rightarrow \mu^+\mu^-) = 233 \pm 18$ pb) [63]. Distributions of various kinematic variables were found to agree with the CDF Z^0 datasets. The low mass Drell-Yan events (where γ^* is the mediator) were generated with $5 \leq q_T(\gamma^*) \leq 500$ GeV/c and with the $5 \leq m(\gamma^*) \leq 500$ GeV/c^2 , where $q_T(\gamma^*)$ and $m(\gamma^*)$ are the transverse momentum and invariant mass of the mediator. The ISAJET cross section has been corrected to the CDF measured value of 259 ± 57 pb for $11 \leq m_{\gamma^*,Z^0} \leq 60$ GeV/c^2 and $|y_{\gamma^*,Z^0}| \leq 1$ [64]

$t\bar{t}$

This type of background is expected to play a significant role, especially for large stop-sneutrino mass differences. To minimize the statistical uncertainties, we created a sample approximately 220 times larger than the size of the search data. The ISAJET cross section has been corrected to agree with the CDF published value of 6.5±1.7 pb[65].

WW, WZ, ZZ

In case of electroweak boson pair productions, the ISAJET cross sections have been scaled to the next-to-leading order calculations of $\sigma_{NLO}(WW) = 9.53$ pb, $\sigma_{NLO}(WZ) = 1.33$ pb and $\sigma_{NLO}(ZZ) = 1.08$ pb [66, 67, 68]. The production mechanism diagrams are shown on Fig. 10.3.

11.4. Stop Signal and SM Background at Preselection: Dileptons, Jets, Missing E_T

Tab. 11.4 shows the expected stop signal (for a nominal point $m_{\tilde{t}} = 100$ GeV/c^2 , $m_{\tilde{\nu}} = 75$ GeV/c^2) and Standard Model background in Run 1A and Run 1B luminosities. It also shows the effect of the inclusion of the trigger efficiencies, and of all other

Table 11.4
Expected Run 1A and Run 1B stop signal (for a nominal point $m_{\tilde{t}} = 100$ GeV/c^2 , $m_{\tilde{\nu}} = 75$ GeV/c^2) and expected Run 1A and Run 1B Standard Model background at the preselection stage.

	Signal		Background							
Run 1A			$b\bar{b}, c\bar{c}$		Drel-Yan		$t\bar{t}$		WW,WZ,ZZ	
Lept ID										
Cleanup, 1 jet	5.06		14.4		11.24		1.97		0.84	
$\not\!\!E_T \geq 15$ GeV										
Trigger Effic.	4.7		12.3		10.4		1.94		0.81	
	4.18		10.92		9.37		1.75		0.74	
All Effic.	OS	LS	OS	LS	OS	LS	OS	LS	OS	LS
	4.00	0.18	7.95	2.97	9.30	0.07	1.65	0.10	0.66	0.08

	Signal		Background							
Run 1B			$b\bar{b}, c\bar{c}$		Drel-Yan		$t\bar{t}$		WW,WZ ZZ	
Lept ID										
Cleanup, 1 jet	23.42		64.78		52.11		9.26		3.93	
$\not\!\!E_T \geq 15$ GeV										
Trigger Effic.	19.42		48.91		43.21		8.29		3.48	
	19.42		48.91		43.21		8.29		3.48	
All Effic.	OS	LS	OS	LS	OS	LS	OS	LS	OS	LS
	18.56	0.86	35.51	13.4	42.88	0.33	7.83	0.46	3.15	0.33

efficiencies discussed at the beginning of this chapter. Note that the Run 1a expectations were obtained from Monte Carlo samples generated for Run 1B, but scaling them to Run 1A luminosity and using the proper Run 1A trigger, lepton identification and lepton isolation efficiencies. A total of 23.6 signal and 126.6 background events are expected at this stage.

12. Comparison of Observed Data with Expected Background

The stop signal would manifest itself in the dilepton data by the presence of two opposite charge energetic leptons, jets and substantial missing transverse energy in the events. Tab. 12.1 shows the Run 1A and Run 1B (opposite plus like sign) events as well as the opposite and like sign event breakdown at the preselection stage. The expected signal and background events are also assigned statistical and systematic uncertainties which we will discuss in detail in Sec. 14. The acceptance[1] of the signal at this stage is $\mathcal{A} = 2.5\%$. The number of expected background events agrees very well with the number of observed events both in Run 1A and Run 1B, as well as in the opposite and like sign channels.

Figs. 12.1 and 12.2 show the distributions of four key variables of the stop signature, namely the p_T of the first and second leptons, the missing transverse energy and the number of jets with $E_T \geq 15$ GeV found in the central region of the detector. In those figures we compare the Standard Model expectations (fake leptons included) with observed data. The p_T distributions of the leptons show that both high and low p_T lepton sources agree well with the observed data. The observed $\not\!\!E_T$ agrees at both low $\not\!\!E_T$, where detector effects dominate, and high $\not\!\!E_T$, where neutrinos from W and Z bosons determine the spectrum. We also remark that the parton shower Monte Carlo describes well the observed jet multiplicity.

Given the low (13:100) signal to background ratio, at this stage it is impossible to decide if any of the observed data is stop quark originated. In the next section we address this issue in a more detailed way.

[1]The acceptance $\mathcal{A}$ is defined as the ratio of the number of expected signal events after selection cuts have been applied and the number of produced signal events in the $p\bar{p}$ collisions.

Table 12.1

Comparison of the expected background and stop signal (assuming $m_{\tilde{t}} = 100$ GeV/c^2 and $m_{\tilde{\nu}} = 75$ GeV/c^2) with the observed data in Run 1A of $\int Ldt = 18.6\ pb^{-1}$, and Run 1B of $\int Ldt = 88.6\ pb^{-1}$. Both the opposite and like sign events are included. The lower table compares the opposite and like sign events in the whole Run 1 of $\int Ldt = 107\ pb^{-1}$. Two isolated leptons of $p_T \geq 6$ GeV/c and $p_T \geq 10$ GeV/c, $\not\!\!E_T \geq 15$ GeV and a jet of $E_T \geq 15$ GeV were required at the preselection stage. For more details see Tab. 9.1 and Tab. 11.4.

Source	**Run 1A**			**Run 1B**		
	N	± Stat.	± Syst.	N	± Stat.	± Syst.
Drell-Yan	9.4	± 0.3	± 2.4	43.2	± 1.6	± 11.3
$b\bar{b}$,$c\bar{c}$	10.9	± 0.6	± 6.6	48.9	± 2.8	± 31.1
$t\bar{t}$	1.75	± 0.04	± 0.51	8.3	± 0.2	± 2.4
WW,WZ,ZZ	0.74	± 0.05	± 0.03	3.5	± 0.2	± 0.8
Misidentified Leptons	5.0	± 0.3	± 0.9	23.8	± 1.5	± 4.3
Total Background	27.8	± 0.8	± 9.2	127.7	± 3.5	± 43.5
Observed Data	23			153		
Expected $\tilde{t}\bar{\tilde{t}}$	4.2	± 0.2	± 1.5	19.4	± 0.8	± 6.9

Source	**Opposite Sign**			**Like Sign**		
	N	± Stat.	± Syst.	N	± Stat.	± Syst.
Drell-Yan	52.2	± 1.8	± 13.6	0.4	± 0.2	± 0.3
$b\bar{b}$,$c\bar{c}$	43.5	± 2.4	± 32.0	16.4	± 2.5	± 17.4
$t\bar{t}$	9.5	± 0.2	± 2.9	0.57	± 0.06	± 0.16
WW,WZ,ZZ	3.8	± 0.3	± 0.9	0.40	± 0.08	± 0.06
Misidentified Leptons	16.3	± 1.4	± 4.2	12.4	± 1.1	± 3.2
Total Background	125.2	± 3.4	± 46.6	30.1	± 2.7	± 18.2
Observed Data	128			48		
Expected $\tilde{t}\bar{\tilde{t}}$	22.6	± 0.9	± 8.4	1.0	± 0.2	± 0.4

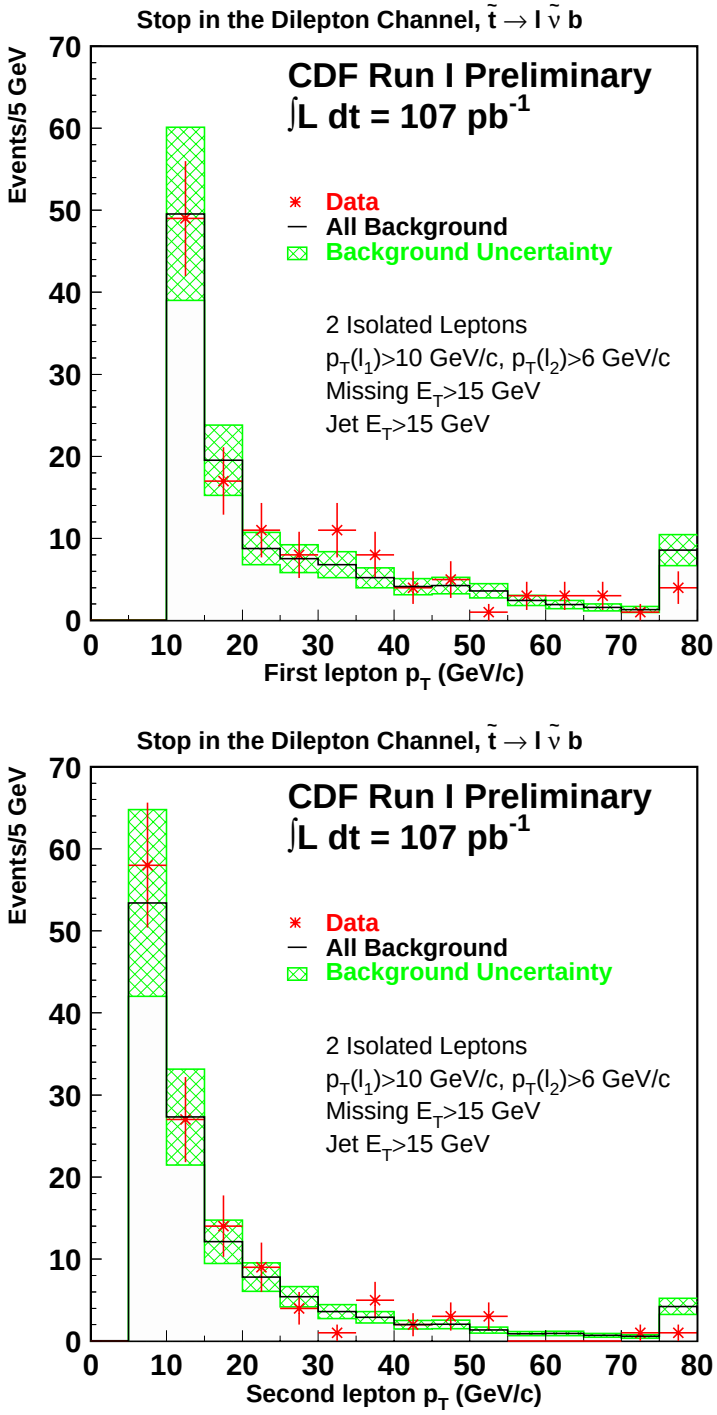

Figure 12.1. Comparison of the distributions of the first and second lepton momenta of Run 1 opposite sign data with expected background. Listed preselection cuts were applied. The hatched band is the total uncertainties on the background. The last high bin contains the overflows.

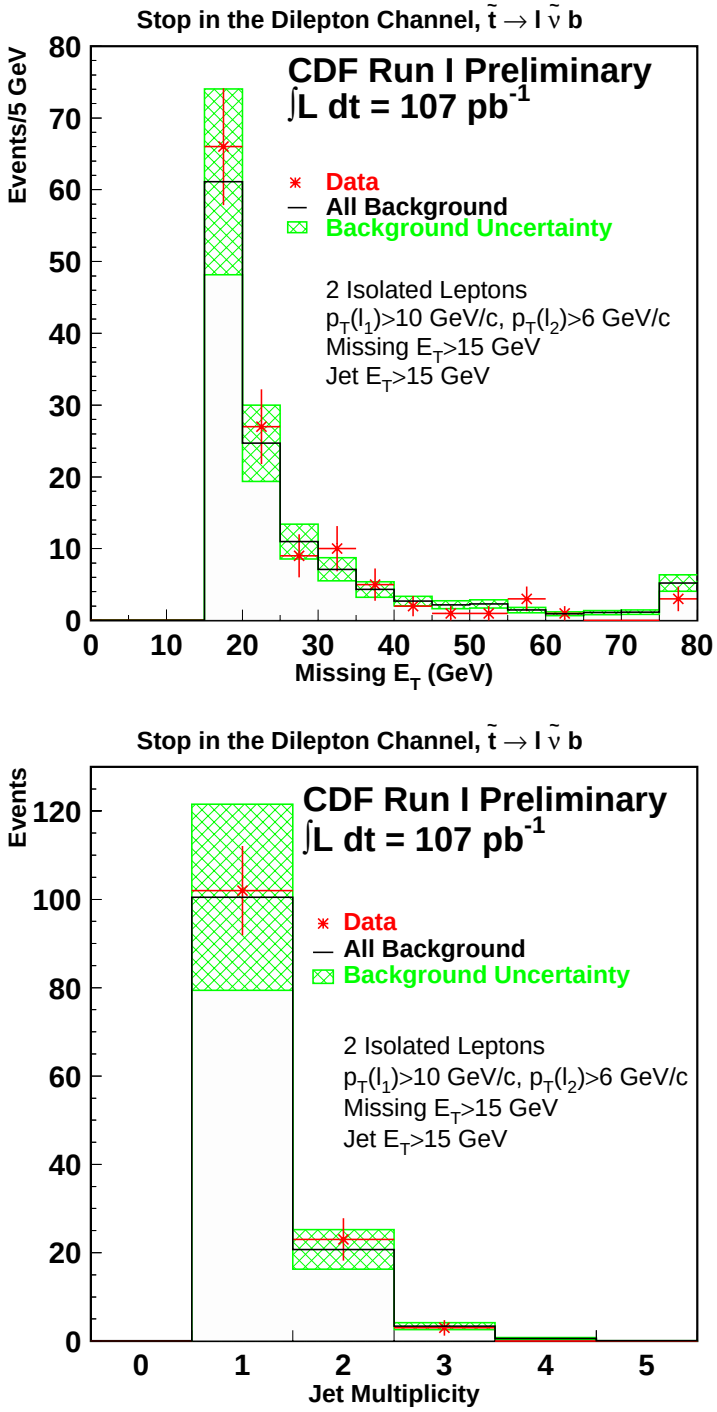

Figure 12.2. Comparison the missing transverse energy and the jet multiplicity distribution of Run 1 data with expected background. Opposite sign dilepton events after the listed preselection cuts are shown. The hatched bands are the total uncertainties on the background. The last high bin contains the overflows.

13. Analysis Cuts: Enhancing Signal, Reducing Background

Tab. 12.1 indicates that the possible SUSY signal of about 23 events is hidden in a substantial number of 176 background events. From this signal to background ratio it is clear that at the preselection level it is impossible to draw any conclusion about the presence (or lack) of the stop signal in our sample. In this section we study various kinematic variables, and we develop a set of cuts[1] on these variables, which will distinguish the stop signal from the background in a statistically significant manner. We define the *efficiency* of a cut by the ratio of the number of events passing the cut to the number of tested events. The aim is to use cuts with high efficiencies when applied on signal, but yielding low efficiencies when applied on background events. We want to get to a kinematic region that is stop enhanced, and has very small background. The reason for this is to minimize the possible effect of the rather large systematic uncertainties in the backgrounds. We evaluate the cut quality with the $\frac{\mathrm{S}}{\sqrt{\mathrm{B}}}$ variable, where S (B) stands for the number of signal (background) events passing a given cut. We use such cuts, that maximize the $\frac{\mathrm{S}}{\sqrt{\mathrm{B}}}$ variable. We tune our cuts on the opposite sign events (OS), but show their effect on both the OS and like sign (LS) events.

13.1. Missing Transverse Energy

Table 12.1 shows that the largest background contributors to the dilepton search sample at the preselection level are the $b\bar{b}$, $c\bar{c}$ and Drell-Yan events. They contribute more than 70 % of the total background. A promising way to reduce their contribution could be the use of the missing energy variable. As we argued in Sec. 10, the signal

[1] A cut is a testing operator ($\mathcal{O}$) acting on a given variable (A) testing it against a given value (V). The event is passed to further processing if the result of the test is positive. Otherwise the event is discarded. For example if A=$\not{E}_{\mathrm{T}}$, $\mathcal{O} \in \{>\}$ and V=30 GeV, then the event is kept if $\not{E}_{\mathrm{T}} > 30$ GeV.

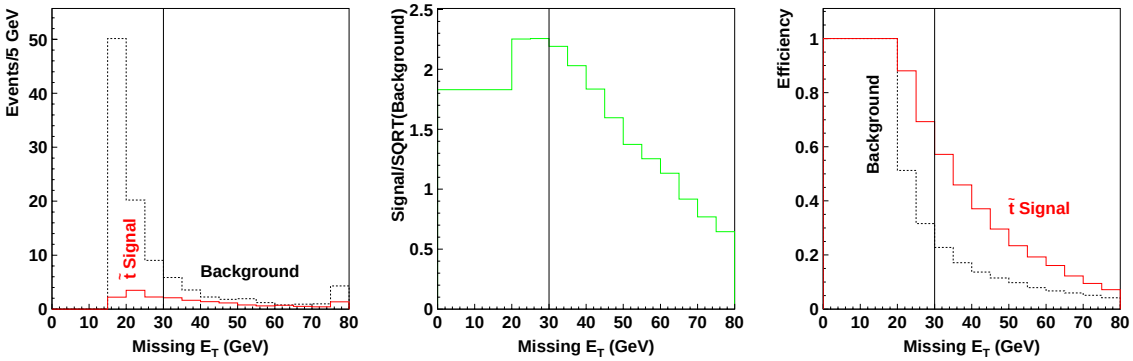

Figure 13.1. Comparison of the distributions of the missing transverse energy of the expected background with the stop signal in Run 1B. The last high bin contains the overflows. Also shown the $S/\sqrt{B}$ variable and the efficiency as a function of the placed missing transverse energy cut ($\not\!\!E_T < X$ GeV). Opposite sign events passing L_i, $i \in \{1, \ldots, 5\}$ preselection cuts (see Tab. 13.9) are shown.

events should exhibit a large value of energy imbalance in the detector, whereas the $b\bar{b}$, $c\bar{c}$ and Drell-Yan events do not. Fig. 13.1 showing the $\not\!\!E_T$ distribution of signal and background confirms this. We also show the $\frac{S}{\sqrt{B}}$ and the efficiencies of $\not\!\!E_T \geq X$ cut for various cut values X shown on the horizontal axis. As a result of these graphs, we choose the optimal value for X, and place the cut (listed as L_6 in Tab. 13.9) at:

$$\boxed{\not\!\!E_T \geq 30 \text{ GeV}}$$

Table 13.1 shows the number of expected background and signal events after placing the above mentioned cut. The $b\bar{b}$,$c\bar{c}$ and Drell-Yan contribution dropped by 85% while about 60% of the signal passed. In Fig. 13.2 we confirm that the applied $\not\!\!E_T \geq$ 30 GeV cut stays optimal even after placing the other analysis cuts.

Table 13.1
Expected signal (assuming $m_{\tilde{t}} = 100$ GeV/c^2 and $m_{\tilde{\nu}} = 75$ GeV/c^2) and background events passing L_i, $i \in \{1, \ldots, 5\}$ and $\not\!\!E_T \geq 30$ GeV cuts in Run 1 (see Tab. 13.9). At this stage $\mathcal{A} = 1.4\%$ and $S/\sqrt{B} = 2.3$.

Source	**Opposite Sign** N	**Like Sign** N
Drell-Yan	11.03	0.07
$b\bar{b}$,$c\bar{c}$	2.97	1.46
$t\bar{t}$	8.57	0.49
WW,WZ,ZZ	2.84	0.26
Misidentified Leptons	3.25	2.04
Total Background	28.66	4.32
Expected $\tilde{t}\bar{\tilde{t}}$	12.88	0.39

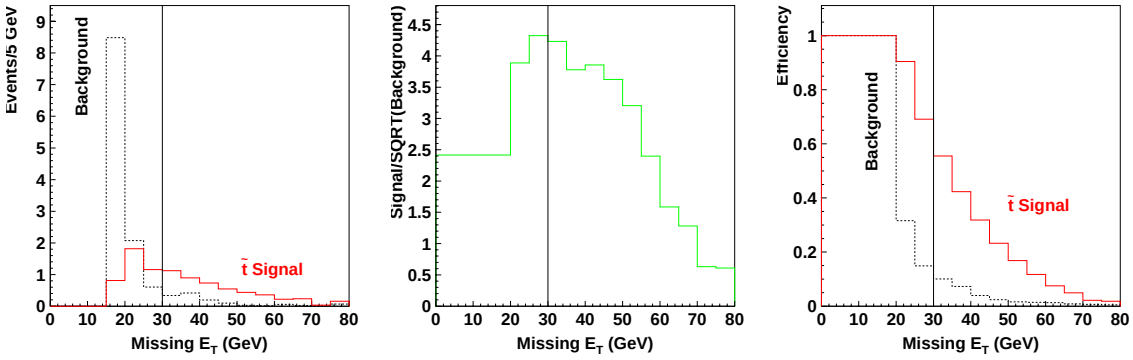

Figure 13.2. Comparison of the expected background and stop signal ($m_{\tilde{t}} = 100$ GeV/c^2 and $m_{\tilde{\nu}} = 75$ GeV/c^2) in Run 1B. All L_i, $i \in \{1, \ldots, 13\}$ cuts were applied except the $\not\!\!E_T \geq 30$ GeV cut (see Tab. 13.9).

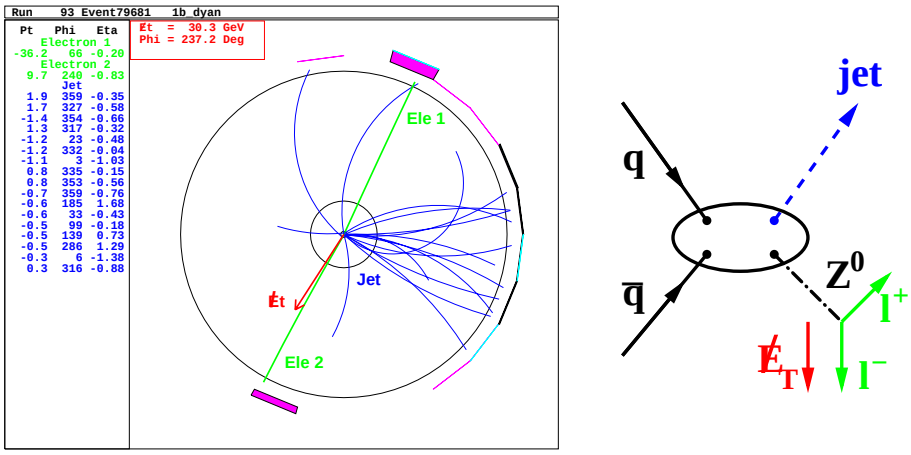

Figure 13.3. Example of a mismeasured lepton (Ele 2) in a Drell-Yan Monte Carlo event $q\bar{q} \rightarrow Z^0 \rightarrow e^+e^-$. The mismeasurement is most likely due to energy leakage to uninstrumented region between two EM calorimeter wedges.

13.2. Collimation of the Missing Transverse Energy with the Leptons

Tab. 13.1 shows that after the $\not\!\!E_T$ cut, about 33% of the background are Drell-Yan events and they dominate it. This is not surprising, because there are Drell-Yan events where τ leptons were produced and their leptonic decays yield neutrinos which escape detection giving rise to significant $\not\!\!E_T$ that they pass the $\not\!\!E_T$ cut. Also the mismeasurement of the leptonic energies can cause energy misbalance in the detector. In such a case the missing energy is aligned with the mismeasured lepton. As an example, in Fig. 13.3, we examine one of the Drell-Yan events (simulated by Monte Carlo) that passes the $\not\!\!E_T \geq 30$ GeV cut. It shows the production of a gluonic jet (Jet) and a photon γ or virtual Z boson which then decays to an energetic pair of electrons (Ele 1 and Ele 2). The energies of Ele 1 and of the Jet are well measured. Ele 2 was generated with $E_T^{GENE}(Ele2) = 45$ GeV, but it was measured having $E_T^{MEASUR}(Ele2) = 10$ GeV, most likely because part of its energy leaked out between two calorimeter wedges (as the event display also suggests). Since all the

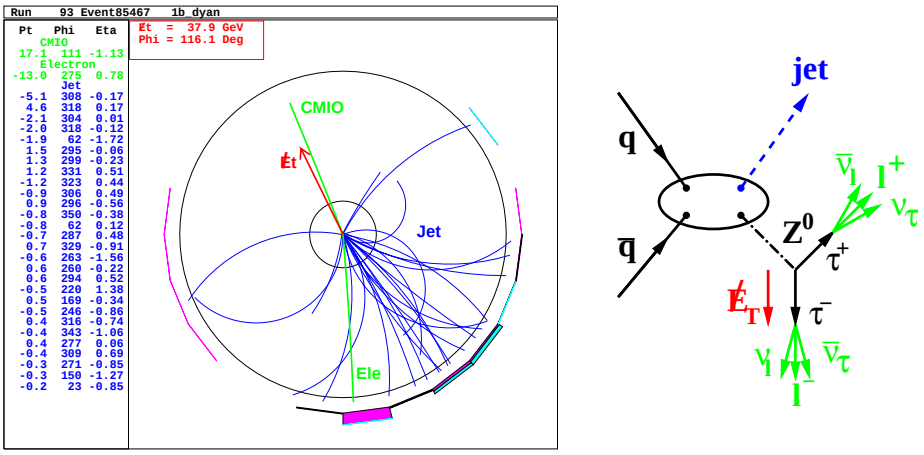

Figure 13.4. Example of a $q\bar{q} \to Z^0 \to \tau^+\tau^- \to \mu^+\bar{\nu}_\tau\nu_\mu e^-\nu_\tau\bar{\nu}_e$ Drell-Yan Monte Carlo event. One of the tau leptons decays to a muon (CMIO) and two very energetic neutrinos which give rise to missing transverse energy aligned with the CMIO.

other objects were well measured, the missing transverse energy (represented by the arrow) is aligned with the direction of the mismeasured electron.

Drell-Yan processes can create $\tau^+\tau^-$ lepton pairs as well. When these τ's decay leptonically, it can happen that the neutrinos from one of the taus takes a substantial fraction of the τ's energy. Given the high boost of the taus, their decay products are narrowly collimated along the direction of the parent tau. This means that the missing transverse energy is aligned with one of the leptons of the event. See Fig. 13.4 as an example. The virtual Z^0 decays into two τ leptons. One tau produces an electron, and soft neutrinos of approximately 4 GeV. The other tau decays to a muon which is not found in the muon chambers but is found as a CMIO object. It is accompanied by two neutrinos of transverse energy of 11 and 26.4 GeV resulting in a total of $\not\!\!E_{\rm T} = 37.4$ GeV in the direction of the CMIO.

For the stop signal, the missing transverse energy is mostly due heavy sneutrinos escaping the detector. Therefore the $\not\!\!E_{\rm T}$ is not collimated with the leptons. This

opens the possibility of using the opening angle between the $\not\!\!E_{\rm T}$ and the leptons to reduce the Drell-Yan background.

Figure 13.5 shows the comparison of the opening angles between the $\not\!\!E_{\rm T}$ and the leptons ($\Delta\phi(l_1, \not\!\!E_{\rm T})$, $\Delta\phi(l_2, \not\!\!E_{\rm T})$) for the stop signal, Drell-Yan events, and for all of the expected background. We also examine the dependence of the $\frac{\rm S}{\sqrt{\rm B}}$ variable and of the cut efficiency on the value X of the placed opening angle cuts[2] $\Delta\phi(l_1, \not\!\!E_{\rm T}) \geq X^\circ$ and $\Delta\phi(l_2, \not\!\!E_{\rm T}) \geq X^\circ$. We chose the optimal value of X as 30° and we use that for the cut, (listed as $\rm L_7$ in Tab. 13.9), and used in Tab. 13.2:

$$\boxed{\Delta\phi(\text{low lept}, \not\!\!E_{\rm T}) \geq 30^\circ \text{ .AND. } \Delta\phi(\text{high lept}, \not\!\!E_{\rm T}) \geq 30^\circ}$$

Table 13.2 shows the number of remaining signal and background events after the above cut has been applied together with the previous cuts $\rm L_{\it i}$, $i \in \{1, \ldots, 6\}$. About 50% of the background has been rejected, while as much as 70% of signal passed the cuts. In Fig. 13.6 we also show that the opening angle cuts remain optimal even after all the analysis cuts $\rm L_{\it i}$, $i \in \{1, \ldots, 13\}$ have been applied.

[2]Since there is no reason to believe in different collimation of $\not\!\!E_{\rm T}$ with the tight and loose leptons, we place the same angular requirement on both of them.

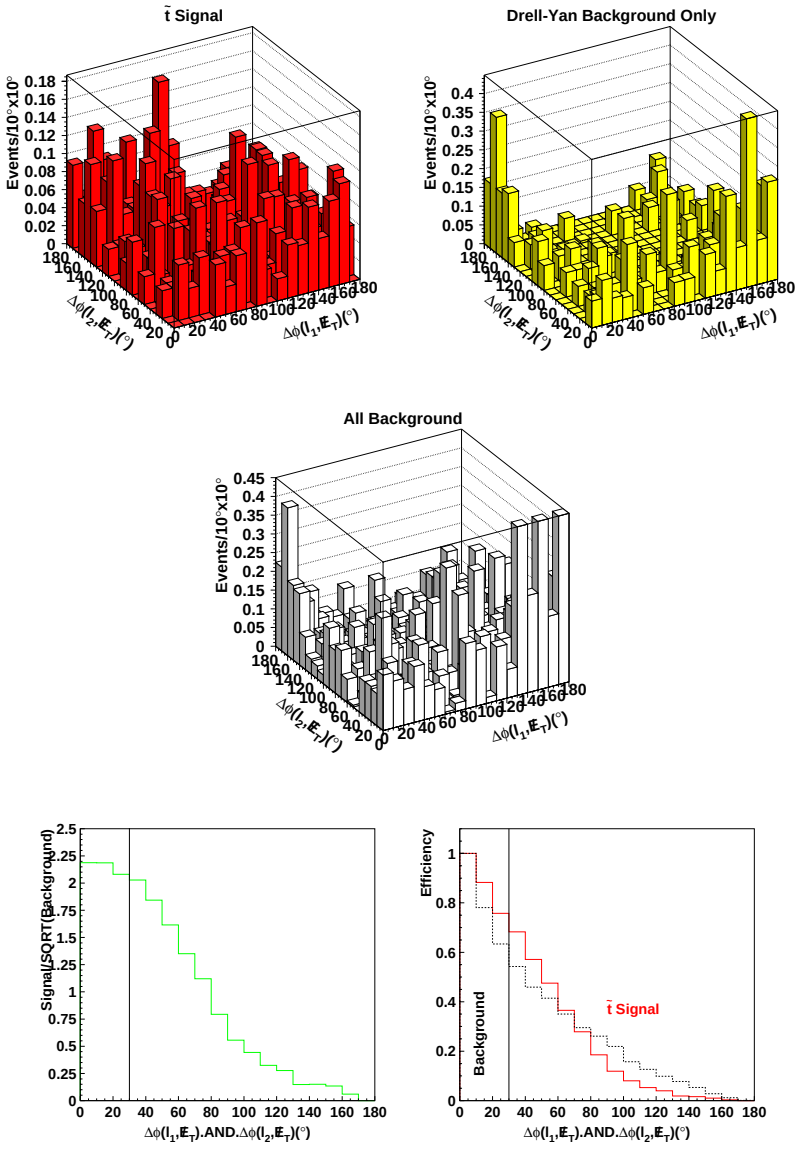

Figure 13.5. The distribution of the opening angle between the missing transverse energy and the leptons shown for the stop signal, Drell-Yan and all background events in Run 1B. We also show the behavior of the $S/\sqrt{B}$ variable and of the efficiency as a function of placed $\Delta\phi(l_1, \not{E}_T) \geq X^\circ$ and $\Delta\phi(l_2, \not{E}_T) \geq X^\circ$ cuts. Opposite sign events passing L_i, $i \in \{1, \ldots, 6\}$ cuts are shown (see Tab. 13.9).

Table 13.2
Expected signal (assuming $m_{\tilde{t}} = 100$ GeV/c^2 and $m_{\tilde{\nu}} = 75$ GeV/c^2) and background events passing $\mathrm{L}_i,\ i \in \{1, \ldots, 6\}$ as well as $\Delta\phi(l_1, \not\!\!E_{\mathrm{T}}) \geq 30^\circ$ and $\Delta\phi(l_2, \not\!\!E_{\mathrm{T}}) \geq 30^\circ$ cuts in Run 1 (see Tab. 13.9). At this stage $\mathcal{A} = 1.0\%$ and $S/\sqrt{B} = 2.2$.

Source	**Opposite Sign** N	**Like Sign** N
Drell-Yan	3.11	0.00
$b\bar{b}$,$c\bar{c}$	0.40	0.16
$t\bar{t}$	6.89	0.40
WW,WZ,ZZ	2.21	0.23
Misidentified Leptons	2.46	1.24
Total Background	15.51	2.03
Expected $\tilde{t}\bar{\tilde{t}}$	8.80	0.30

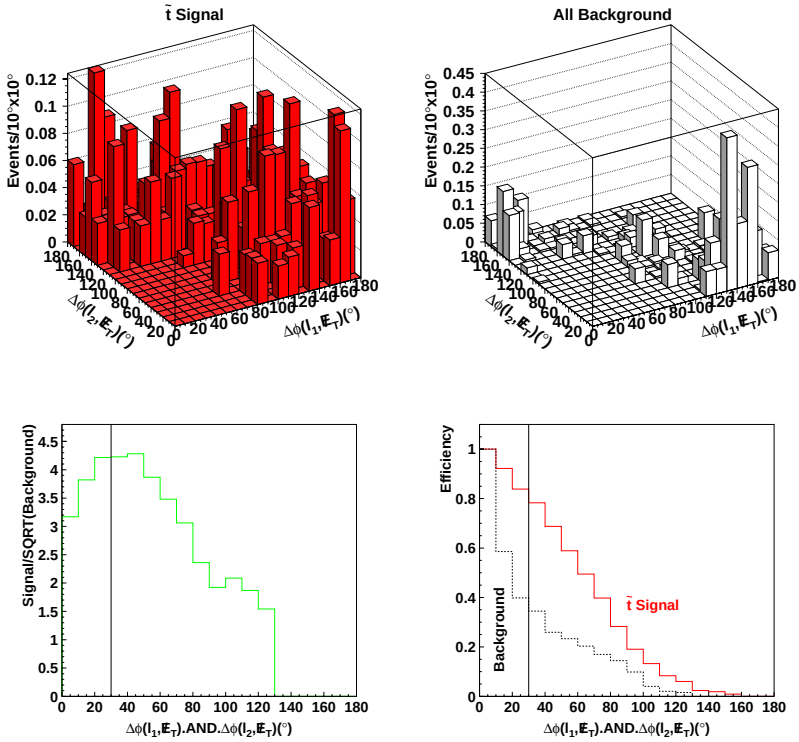

Figure 13.6. The distribution of the opening angle between the missing transverse energy and the leptons shown for the stop signal, and all background events. We also show the behavior of the $S/\sqrt{B}$ variable and of the efficiency as a function of placed $\Delta\phi(l^1, \not{E}_T) \geq X^\circ$ and $\Delta\phi(l^2, \not{E}_T) \geq X^\circ$ cuts. Opposite sign events passing all analysis cuts L_i, $i \in \{1, \ldots, 13\}$ except L_7 (cut on the shown variables) have been applied (see Tab. 13.9).

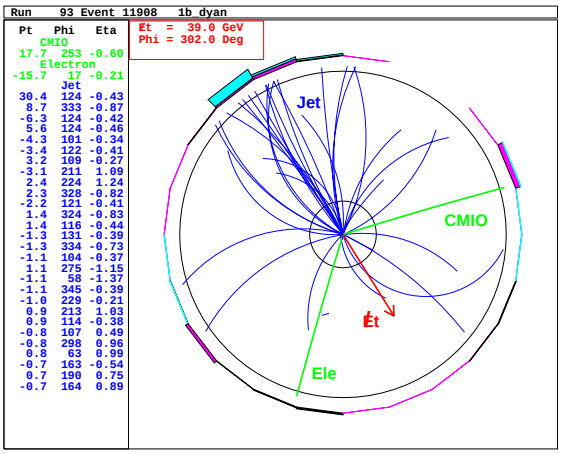

Figure 13.7. Example of a $q\bar{q} \rightarrow Z^0 \rightarrow \tau^+\tau^- \rightarrow \mu^+\bar{\nu}_\tau\nu_\mu e^-\nu_\tau\bar{\nu}_e$ Drell-Yan Monte Carlo event when both tau decays produce energetic neutrinos which give rise to missing E_T aligned with the dilepton system.

13.3. Collimation of Missing Transverse Energy with the Dilepton System

As Tab. 13.2 indicates, we still have a significant number (3) of Drell-Yan events left. This is because we have not dealt with events, where both of the leptons were significantly mismeasured, or, in case of the ditau Drell-Yan production, if both of the taus decay to energetic neutrinos.

When the two energetic Drell-Yan leptons have a small dilepton mass, it indicates that they were produced back-to-back. After the previous cuts (L_7), the $\not\!\!E_T$ cannot be close to either of the leptons. It still could, however, be aligned with the vector of the dilepton system (vector sum of the loose and tight lepton). As an example, see Fig. 13.7, where we show a $q\bar{q} \rightarrow Z^0 \rightarrow \tau^+\tau^-$ event, where one tau lepton decays to an electron with momentum components $p_x = 17\ GeV/c$, $p_y = 5\ GeV/c$ and two neutrinos with a total of $p_x^\nu = 35\ GeV/c$, $p_y^\nu = 10\ GeV/c$. The other tau lepton decays to a muon with $P_x = -17\ GeV/c$, $P_y = -5\ GeV/c$ and two neutrinos with a total of $P_x^\nu = 9\ GeV/c$, $P_y^\nu = 26\ GeV/c$. This then means that the dilepton system has 12 GeV transverse energy and the opening angle between missing energy and the

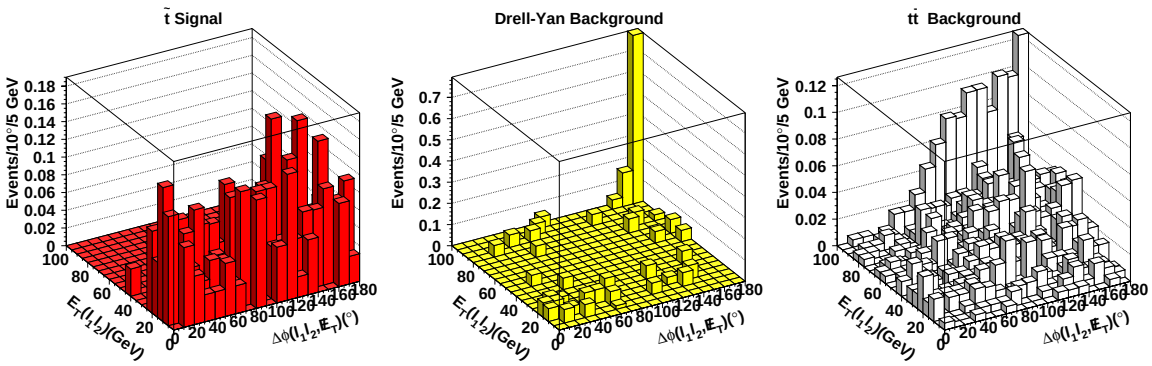

Figure 13.8. Distribution of the dilepton system energy versus opening angle between the dilepton system and the missing energy shown for the expected stop signal, Drell-Yan and $t\bar{t}$ background. Opposite sign events passing L_i, $i \in \{1, \ldots, 7\}$ cuts are shown. The high E_T and high opening angle cluster on the Drell-Yan plot are events whose jet energy has been mismeasured.

dilepton system is very small ($\Delta\phi(l_1 l_2, \not{E}_T) \approx 1°$). The middle picture of Figure 13.8 shows a cluster of such Drell-Yan events. No such correlation is expected for the stop signal and this will be used to further discriminate it from background events.

Tab. 13.2 indicates that the $t\bar{t}$ events are the dominant background at this stage of cuts. They are expected to have very energetic leptons (from heavy electroweak boson decays) with no angular correlation. Therefore the dilepton energy is expected to be rather high in comparison to the dilepton energy of stop events as can be seen in Fig. 13.8. How soft the leptons from the stop decays are, depends on the mass gap ($\Delta(m_{\tilde{t}}, m_{\tilde{\nu}}) = m_{\tilde{t}} - m_{\tilde{\nu}}$) between the stop and the sneutrino. For small mass gaps, the dilepton energy is quite small, and we will use this fact to discriminate the stop signal from the $t\bar{t}$ background. Figures 13.9 and 13.10 compare the expected stop and expected background distributions of: the dilepton energy, and the opening angle between the dilepton system and the missing energy; respectively.

We can substantially reduce the remaining background by placing the cuts listed as L_8 and L_9 in Tab. 13.9:

$$\boxed{\mathrm{E_T}(l_1 l_2) \leq 30 \text{ GeV .AND. } \Delta\phi(l_1 l_2, \not\!\!\mathrm{E}_\mathrm{T}) \geq 30^\circ}$$

Table 13.3 compares the number of expected signal and background events after the above cuts have been placed in addition to all previous analysis cuts $\mathrm{L}_i,\ i \in \{1, \ldots, 7\}$. Almost 75% of the background has been rejected while about 75% of the signal passes. Figures 13.11 and 13.12 show that the cuts remain optimal even when all the other analysis cuts among $\mathrm{L}_i,\ i \in \{1, \ldots, 13\}$ are made.

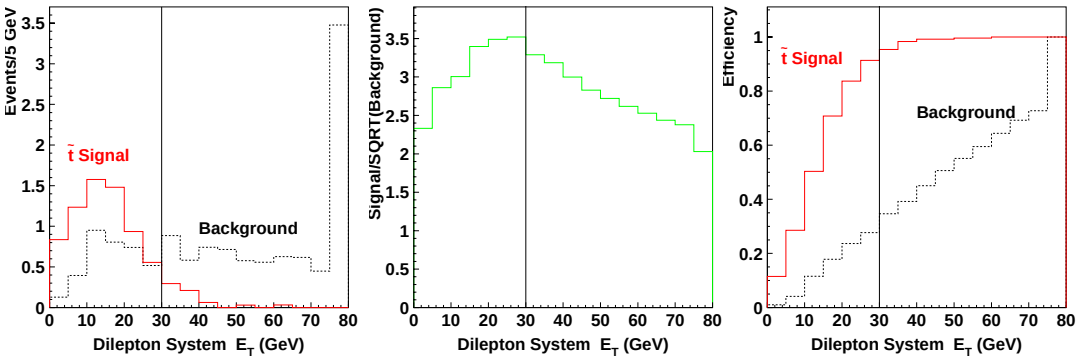

Figure 13.9. Distribution of the dilepton energy from the expected stop signal and from the background in Run 1B. The last high bin contains the overflows. Also shown the $S/\sqrt{B}$ variable and the efficiency as a function of placed dilepton energy cuts ($E_T(l_1 l_2) \leq X$). Opposite sign events passing $L_i,\ i \in \{1, \ldots, 7\}$ cuts are shown (see Tab. 13.9).

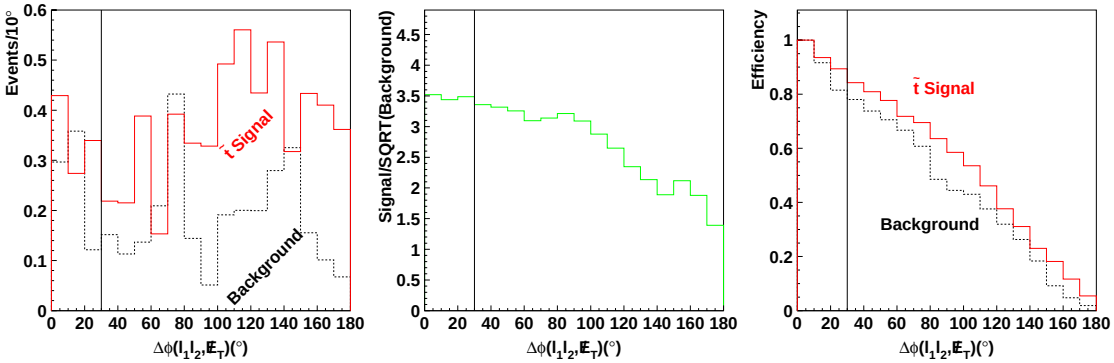

Figure 13.10. Distribution of the opening angle between the dilepton system and the missing energy, from the expected stop signal and from the background in Run 1B. Also shown the $S/\sqrt{B}$ variable and the efficiency as a function of placed opening angle cut ($\Delta\phi(l_1 l_2, \not{E}_T) \geq X°$). Events passing $L_i,\ i \in \{1, \ldots, 7\}$ and $E_T(l_1 l_2) \leq 30$ GeV cuts (see Tab. 13.9).

Table 13.3
Expected signal (assuming $m_{\tilde{t}} = 100$ GeV/c^2 and $m_{\tilde{\nu}} = 75$ GeV/c^2) and background events passing $\mathrm{L}_i,\ i \in \{1,\ldots,7\}$ and $\mathrm{E}_{\mathrm{T}}(l_1 l_2) \leq 30$ GeV and $\Delta\phi(l_1 l_2, \not\!\!E_{\mathrm{T}}) \geq 30^\circ$ are shown (see Tab. 13.9). At this stage $\mathcal{A} = 0.7\%$ and $S/\sqrt{B} = 3.3$.

Source	**Opposite Sign**	**Like Sign**
	N	N
Drell-Yan	0.75	0.00
$b\bar{b}$,$c\bar{c}$	0.28	0.12
$t\bar{t}$	1.02	0.07
WW,WZ,ZZ	0.34	0.05
Misidentified Leptons	1.02	0.80
Total Background	3.41	1.04
Expected $\tilde{t}\bar{\tilde{t}}$	6.77	0.27

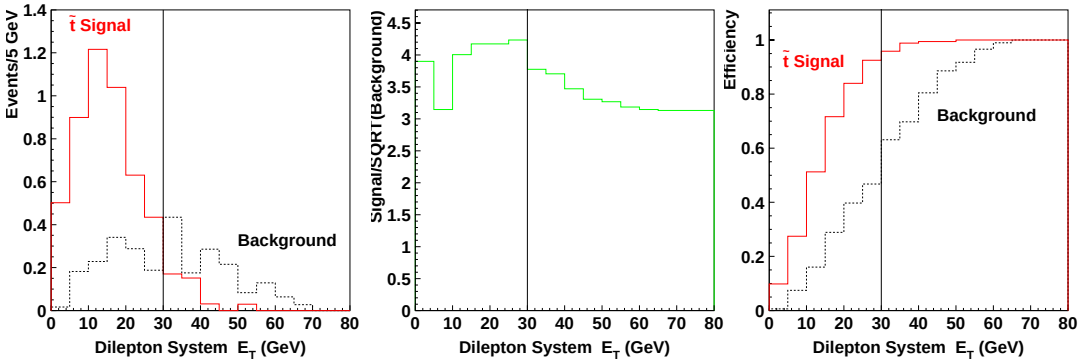

Figure 13.11. The distribution of the dilepton energy of expected stop signal and background in Run 1B. The last bin contains the overflows. Also shown the $S/\sqrt{B}$ variable and the efficiency as a function of the dilepton energy cuts ($E_T(l_1 l_2) \leq X$). Events passing all L_i, $i \in \{1, \ldots, 13\}$ cuts (except the L_8 cut on the plotted variable) are shown (see Tab. 13.9).

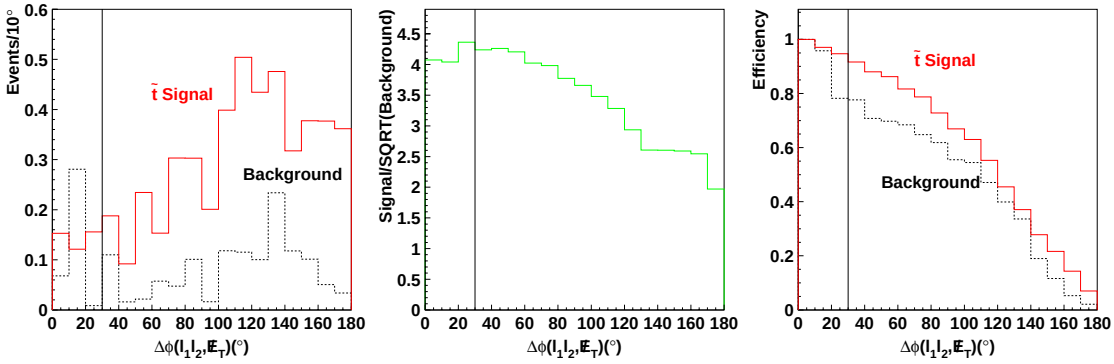

Figure 13.12. The distribution of the opening angle between the dilepton system and the missing energy, of expected stop signal and background in Run 1B. Also shown is the $S/\sqrt{B}$ variable and the efficiency as a function of th opening angle cut ($\Delta\phi(l_1 l_2, \not{E}_T) \geq X^\circ$). Events passing all L_i, $i \in \{1, \ldots, 13\}$ cuts (except the L_9 cut on the plotted variable) are shown (see Tab. 13.9).

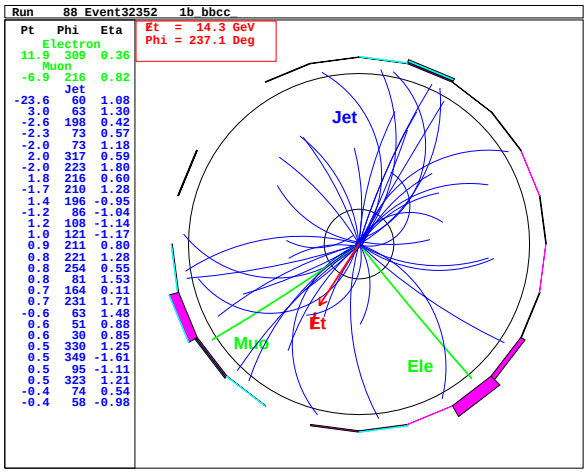

Figure 13.13. Example of a $b\bar{b}$ Monte Carlo event.

13.4. Using Jet Properties to Reduce the Background

Higher order Drell-Yan processes produce in addition to the two leptons also a jet which balances the dilepton system. The two leptons therefore have large opening angles with the jet. Similarly, for the two leptons arising when a final state radiation gluon splits into a $b\bar{b}$ (or $c\bar{c}$) pair and these quarks then balance the jet of the system. Since such $b\bar{b}$ (or $c\bar{c}$) can further decay semileptonically, and we obtain two leptons that have a large opening angle with the jet. In case of initial state gluon splitting, one b-quark goes very forward with the spectator partons (the parent of one of the leptons), while the other b-quark (the parent of the second lepton in the event) is involved in the scattering with the proton's gluon or quark (the source of the jet in the event). In this case, the lepton coming from the first b-quark balances the jet plus the other lepton, and once again, the opening angle between both of the leptons and the jet is expected to be quite large, see Fig. 13.13. Similarly the c-quarks. No such correlation is expected for the stop signal. In Fig. 13.14 we show the distribution of the opening angles between each of the leptons and the jet for the signal and background events. We veto events where both of the leptons have a large opening

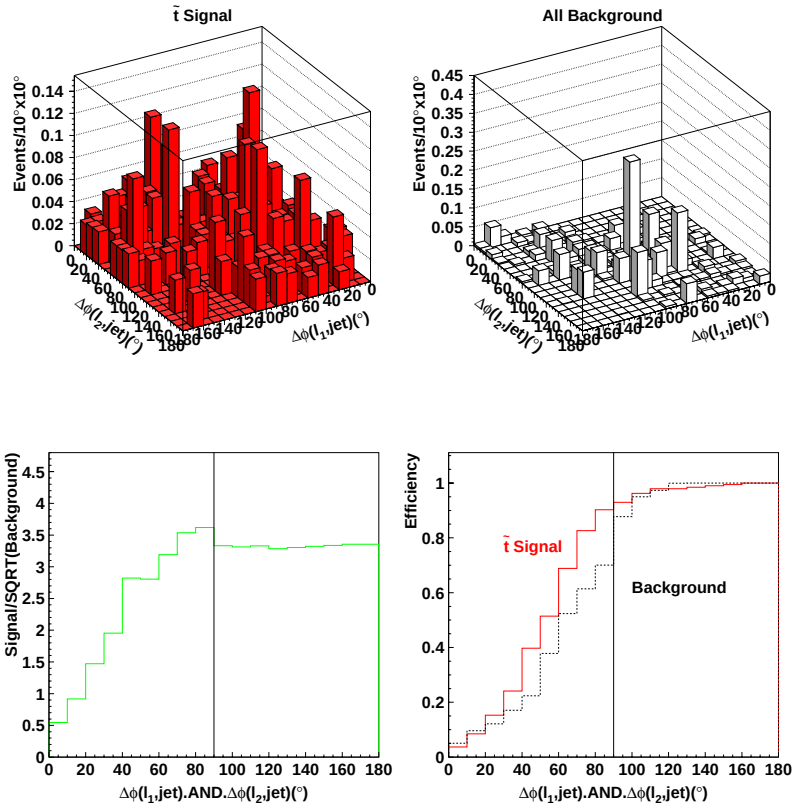

Figure 13.14. Comparison of the distribution of the opening angles between each of the leptons and the jet, for for expected background and stop signals in Run I, $\int Ldt = 107\ pb^{-1}$. Also shown is the $S/\sqrt{B}$ variable and the efficiency as a function of the $(\Delta\phi(l_1, jet) \leq X^\circ$ .OR. $\Delta\phi(l_2, jet) \leq X^\circ)$ cut. Opposite sign events passing $L_i,\ i \in \{1, \ldots, 9\}$ cuts are shown (see Tab. 13.9).

angle with the jet (listed as L_{10} in Tab. 13.9):

$$\boxed{\text{.NOT.}(\Delta\phi(l_1,\text{jet}) \geq 90^\circ \text{ .AND. } \Delta\phi(l_2,\text{jet}) \geq 90^\circ)}$$

Tab. 13.4 summarizes the number of expected signal, background and observed data events after placing the above cuts. We see that we have reduced the Drell-Yan and $b\bar{b}$,$c\bar{c}$ by another 50%, while passing 90% of the signal. Figure 13.15 shows the effect of the L_{10} cut after all analysis cuts $L_i,\ i \in \{1, \ldots, 13\}$ have been placed except cut L_{10}, showing that the cut remains optimal.

Table 13.4
Expected signal (assuming $m_{\tilde{t}} = 100$ GeV/c^2 and $m_{\tilde{\nu}} = 75$ GeV/c^2) and background events passing L_i, $i \in \{1, \ldots, 9\}$ cuts as well as the veto of ($\Delta\phi(l_1, jet) \geq 90^\circ$ .AND. $\Delta\phi(l_2, jet) \geq 90^\circ$) are shown (see Tab. 13.9). At this stage $\mathcal{A} = 0.7\%$ and $S/\sqrt{B} = 3.5$.

Source	**Opposite Sign** N	**Like Sign** N
Drell-Yan	0.44	0.00
$b\bar{b}$,$c\bar{c}$	0.13	0.04
$t\bar{t}$	0.96	0.06
WW,WZ,ZZ	0.33	0.04
Misidentified Leptons	0.53	0.70
Total Background	2.39	0.84
Expected $\tilde{t}\bar{\tilde{t}}$	6.11	0.25

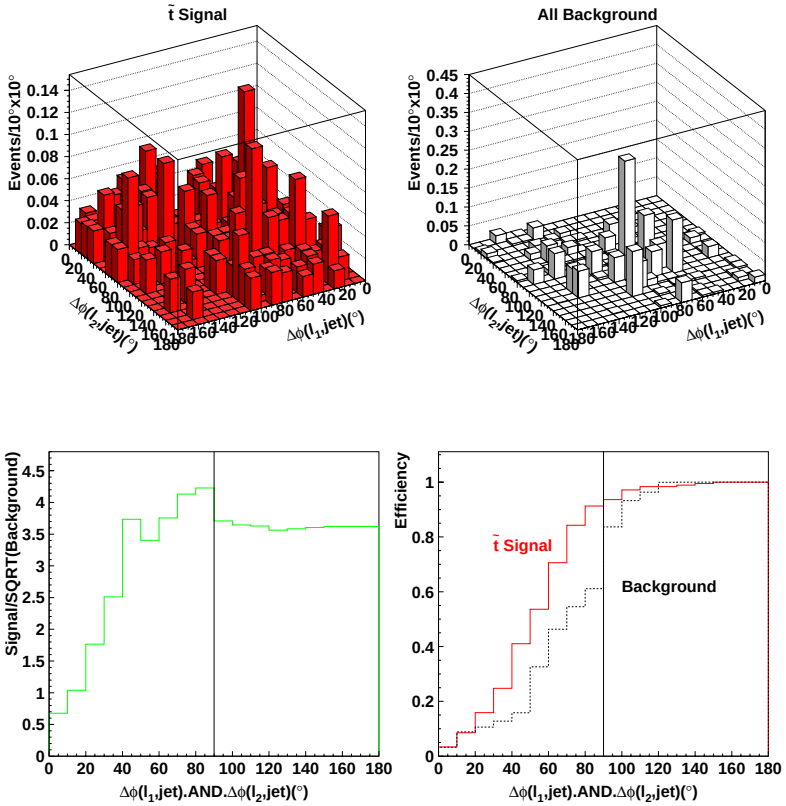

Figure 13.15. Comparison of the distribution of the opening angle between the leptons and the jet of the expected background and stop signal in Run 1B. Also shown the $S/\sqrt{B}$ variable and the efficiency as a function of placed ($\Delta\phi(l_1, jet) \leq X^\circ$ OR $\Delta\phi(l_2, jet) \leq X^\circ$) cuts. Opposite sign events passing all the analysis cuts L_i, $i \in \{1, \ldots, 13\}$ except, the cut (L_{10}) on the plotted opening angles, are shown (see Tab. 13.9).

13.5. High Momentum-Transfer Processes and the Charge Correlation Cut

The most significant remaining sources of background are the $t\bar{t}$ and misidentified lepton events. The $t\bar{t}$ is about 30% of the total background and the misidentified leptons contribute another 40%. Even though the stop production is a high momentum-transfer (Q) process, the escaping heavy sneutrinos take away a large amount of energy from each event, making it look like a substantially smaller momentum-transfer process. Contrarily, the top quark decay products are very energetic, which simplifies their identification and distinction from stop events. Previous analyses [69] used the H_T variable defined by $H_T = \mathrm{p_T}(l_1) + \mathrm{p_T}(l_2) + \not{\mathrm{E}}_\mathrm{T} + \mathrm{E_T}(jet)$ to reduce the $t\bar{t}$ background. In our analysis we proceed similarly, except we split the H_T into two separate variables (1) the scalar sum of energies of the tight and second lepton and (2) the scalar sum of the missing $\mathrm{E_T}$ and the jet energy. Both of these variables are expected to be softer in stop events than in top events. Figs. 13.16 and 13.17 show the effect of the cuts on these variables for background and stop signal events. More than 65% of the remaining top events but only about 6% of the signal events are cut out after we place the following two cuts:

$$\boxed{\mathrm{E_T(high\ lept) + E_T(low\ lept)} \leq 75\ \mathrm{GeV}}$$
$$\boxed{\not{\mathrm{E}}_\mathrm{T} + \mathrm{E_T(central\ jet)} \leq 160\ \mathrm{GeV}}$$

Figures 13.18 and 13.19 show the effect of those cuts on the the background and stop signal after all the other analysis cuts $\mathrm{L}_i,\ i \in \{1, \ldots, 13\}$ (except L_{11} (L_{12})) were applied. The cut on the scalar sum of the energies of tight and loose leptons is not placed at its optimal value in order to save some signal efficiency.

Table 13.5 compares the remaining signal and background events of Run 1A and Run 1B separately after the above cuts have been placed. We expect a total of 5.97 ± 2.17 stop signal and 2.31 ± 0.52 background events. After these cuts, the dominating background (1.14 ± 0.34 events) comes from misidentified leptons. About 60% of them result in events where the tight and the loose leptons have the same electric charge. This is in contrast to the signal events, where only about 4% of the events have

leptons with the same electric charge[3]. We further enhance the significance of the stop quark events by rejecting the like sign dilepton events and keeping the

Opposite Electric Charge Leptons Only.

Tab. 13.6 compares the expected background and stop signal events after the opposite sign cut has been placed. We expect 5.73 ± 0.45 ± 2.13 signal and 1.52 ± 0.30 ± 0.36 background events from Monte Carlo calculations. At this point we were satisfied with the enhancement of the signal region and reduction of the possible background. Compared to the preselection stage shown in Tab. 12.1, 99% of the total expected background is rejected by our selection cuts, whereas more than 25% of the signal events passed (when the nominal $m_{\tilde{t}} = 100$ GeV/c^2 and $m_{\tilde{\nu}} = 75$ GeV/c^2 combination is used). Table H.1 lists the number of expected signal events passing all of the selection cuts L_i, $i \in \{1, \ldots, 13\}$ for a variety of the MC generated $m_{\tilde{t}}$, $m_{\tilde{\nu}}$ mass combinations. We observe, that the developed set of cuts L_i is very efficient when the mass gap $\Delta(m_{\tilde{t}}, m_{\tilde{\nu}})$ is small. This is because in that case leptons from the stop decays are soft and form a dilepton system with rather small energy. Then the cut on the dilepton system's energy, L_8, is very efficient in reducing the background while still keeping the signal. Of course, in the case where $\Delta(m_{\tilde{t}}, m_{\tilde{\nu}})$ is very small, which arises when we get too close to the kinematic limit $m_{\tilde{t}} \geq m_{\tilde{\nu}} + m_b$, lepton and jet energies become very soft, limiting our stop detection capabilities.

From Tab. H.1 we also observe, that for scenarios where the $\Delta(m_{\tilde{t}}, m_{\tilde{\nu}})$ is rather large, we lose sensitivity to the stop signal. This is because leptons from the stop decays are very energetic, with a lot of energy in their dilepton system and the L_8 cut, $\mathrm{E}_{\mathrm{T}}(l_1 l_2) \leq 30$ GeV, becomes very inefficient, cutting out too many signal events.

We can significantly improve our sensitivity in the large $\Delta(m_{\tilde{t}}, m_{\tilde{\nu}})$ region, nominally represented by $m_{\tilde{t}} = 120$ GeV/c^2 and $m_{\tilde{\nu}} = 60$ GeV/c^2, by loosening the L_8 cut to 55 GeV. See Fig. 13.20. This cut is then denoted as H_8 in Tab. 13.9. Since in the high $\Delta(m_{\tilde{t}}, m_{\tilde{\nu}})$ region, the leptons from stop decays are quite energetic, we can

[3]These leptons come from semileptonic decays of the stop produced b-quarks.

tighten up the cut on the loose lepton energy, L_3, to be 10 GeV without a significant loss of signal. See Fig. 13.21. This cut is then denoted as H_3 in Tab. 13.9. All the other selection cuts remain the same and together they form the H_i set of cuts used in large $\Delta(m_{\tilde{t}}, m_{\tilde{\nu}})$ region. Their effect on the background and signal is shown in Tabs. 13.7 and 13.8. We note that we again reject 99% of the expected background while passing as much as 24% of the signal (in case of the high $\Delta(m_{\tilde{t}}, m_{\tilde{\nu}})$ nominal point), with respect to the preselection stage. Tab. H.1 summarizes the effect of the H_i set of cuts applied to all MC generated stop-sneutrino. Note for example the region around $(m_{\tilde{t}}, m_{\tilde{\nu}})$= (90,70) GeV/$c^2$ point, where the low $\Delta(m_{\tilde{t}}, m_{\tilde{\nu}})$ cuts, L_i, yield 60% more signal events than the high $\Delta(m_{\tilde{t}}, m_{\tilde{\nu}})$ cuts, H_i would. On the other hand, in the neighborhood of the $(m_{\tilde{t}}, m_{\tilde{\nu}})$=(130,60) GeV/$c^2$ point it is vice versa, making it important to have two slightly different set of cuts to be able to scan the largest possible parameter space for stop signal.

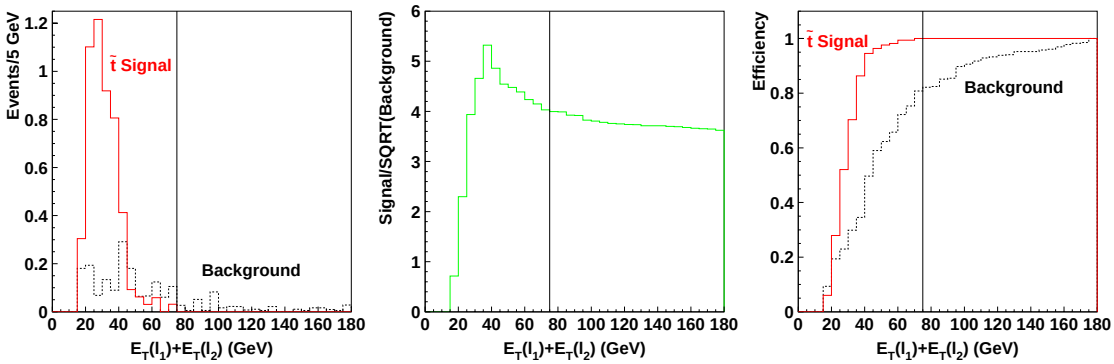

Figure 13.16. The distribution of the scalar sum of the tight and loose lepton energies for expected stop signal and background in Run 1B. The last bin contains the overflows. Also shows the $S/\sqrt{B}$ variable and the efficiency as a function of the energy cut $(E_T(l_1) + E_T(l_2) \leq X)$. Opposite sign events passing L_i, $i \in \{1, \ldots, 10\}$ cuts are shown (see Tab. 13.9).

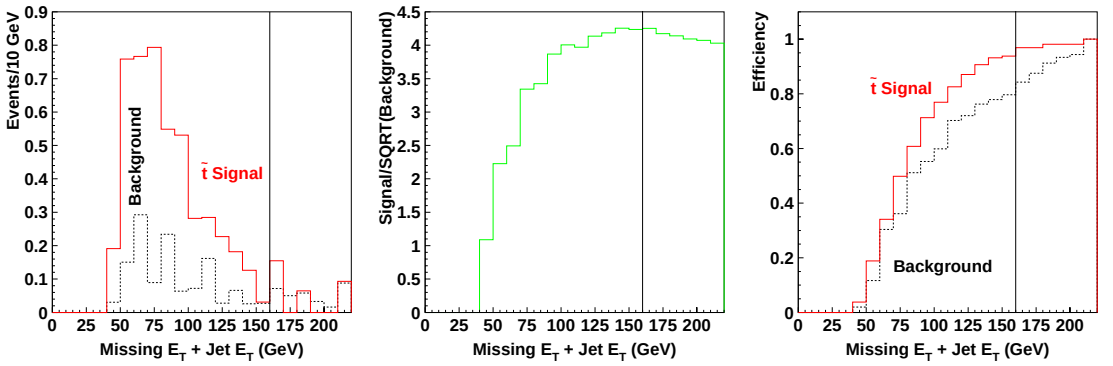

Figure 13.17. The distribution of the scalar sum of the missing transverse energy and the jet energy for expected stop signal and background in Run 1B, $\int Ldt = 107\ pb^{-1}$. The last bin contains the overflows. Also shown the $S/\sqrt{B}$ variable and the efficiency as a function of energy cut $(\not{E}_T + E_T(jet) \leq X)$. Opposite sign events passing L_i, $i \in \{1, \ldots, 11\}$ cuts are shown (see Tab. 13.9).

Table 13.5
Expected background and stop signal (assuming $m_{\tilde{t}} = 100$ GeV/c^2 and $m_{\tilde{\nu}} = 75$ GeV/c^2) in Run 1A of $\int Ldt = 18.6 pb^{-1}$, and Run 1B of $\int Ldt = 88.6 pb^{-1}$. Analysis cuts $L_i,\ i \in \{1, \ldots, 12\}$ were applied (see Tab. 13.9). OS+LS events are shown.

Source	**Run 1A**	**Run 1B**
	N ± Stat.± Syst.	N ± Stat.± Syst.
Drell-Yan	0.08 ± 0.03 ± 0.02	0.30 ± 0.13 ± 0.08
$b\bar{b}$,$c\bar{c}$	0.04 ± 0.02 ± 0.02	0.15 ± 0.07 ± 0.09
$t\bar{t}$	0.06 ± 0.01 ± 0.02	0.30 ± 0.04 ± 0.09
WW,WZ,ZZ	0.05 ± 0.01 ± 0.01	0.22 ± 0.06 ± 0.04
Misidentified Leptons	0.20 ± 0.04 ± 0.04	0.94 ± 0.20 ± 0.20
Total Background	0.42 ± 0.06 ± 0.08	1.89 ± 0.30 ± 0.35
Expected $\tilde{t}\bar{\tilde{t}}$	1.05 ± 0.08 ± 0.37	4.92 ± 0.38 ± 1.75

Table 13.6
Expected background and stop signal (assuming $m_{\tilde{t}} = 100$ GeV/c^2 and $m_{\tilde{\nu}} = 75$ GeV/c^2) in Run 1 of $\int Ldt = 107 pb^{-1}$. All analysis cuts $L_i,\ i \in \{1, \ldots, 13\}$ were applied (see Tab. 13.9). At this stage $\mathcal{A} = 0.6\%$ and $S/\sqrt{B} = 4.6$

Source	**Opposite Sign**
	N ± Stat.± Syst.
Drell-Yan	0.38 ± 0.20 ± 0.10
$b\bar{b}$,$c\bar{c}$	0.14 ± 0.08 ± 0.10
$t\bar{t}$	0.33 ± 0.05 ± 0.10
WW,WZ,ZZ	0.25 ± 0.07 ± 0.06
Misidentified Leptons	0.43 ± 0.20 ± 0.10
Total Background	1.52 ± 0.30 ± 0.36
Expected $\tilde{t}\bar{\tilde{t}}$	5.73 ± 0.45 ± 2.13

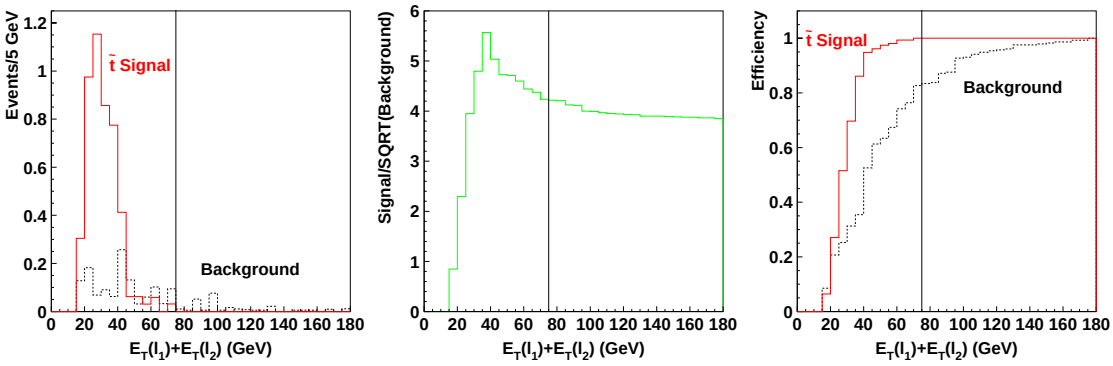

Figure 13.18. The distribution of the scalar sum of the tight and loose lepton energies for expected stop signal and background in Run 1B. The last high bin contains the overflows. Also shown the $S/\sqrt{B}$ variable and the efficiency as a function of energy cut $(E_T(l_1)+E_T(l_2) \leq X)$. Opposite sign events passing all the analysis cuts $L_i,\ i \in \{1,\ldots,13\}$ except the cut (L_{11}) on the scalar sum of the leptons are shown (see Tab. 13.9).

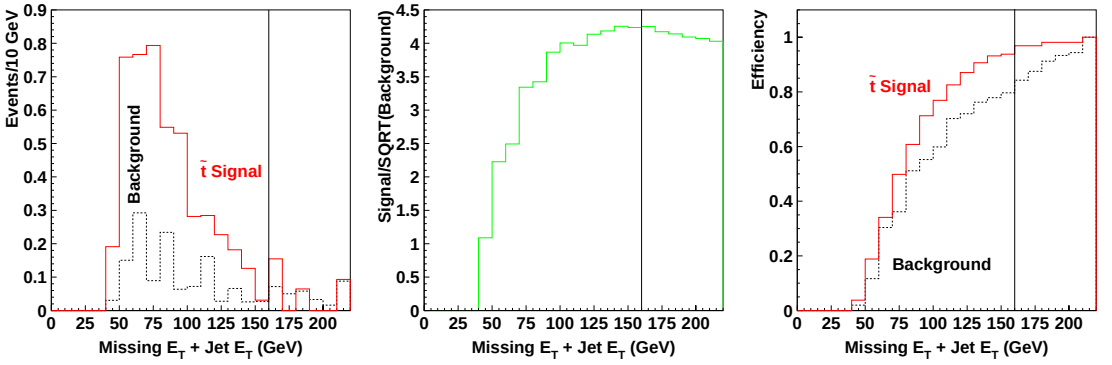

Figure 13.19. The distribution of the scalar sum of the missing transverse energy and the jet energy for expected stop signal and background in Run 1B. The last high bin contains the overflows. Also shown the $S/\sqrt{B}$ variable and the efficiency as a function of energy cut $(\not{E}_T+E_T(jet) \leq X)$. Events passing all the analysis cuts $L_i,\ i \in \{1,\ldots,13\}$ except the cut (L_{12}) on the scalar sum of the missing transverse energy and jet energy are shown (see Tab. 13.9).

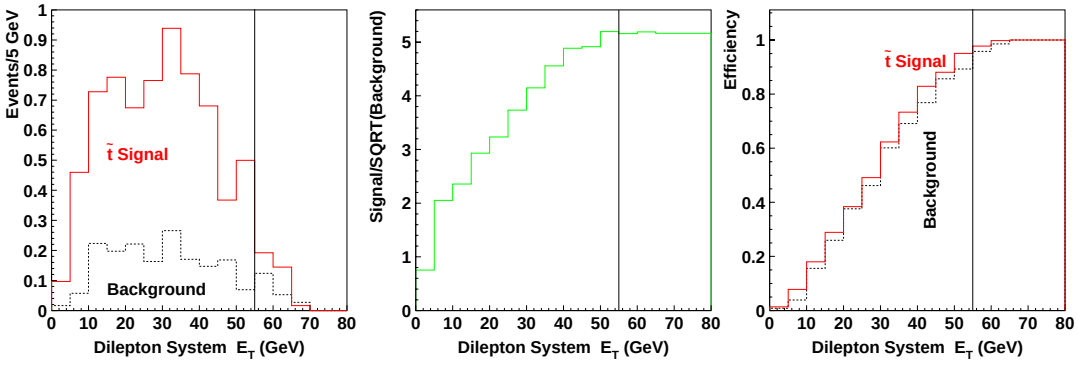

Figure 13.20. The distribution of the dilepton system energy for expected stop signal (assuming $m_{\tilde{t}} = 120$ GeV/c^2 and $m_{\tilde{\nu}} = 60$ GeV/c^2) and background in Run 1B, $\int Ldt = 107\ pb^{-1}$. The last high bin contains the overflows. Also shown the S/$\sqrt{\text{B}}$ variable and the efficiency as a function of energy cut ($E_T(l_1 l_2) \leq X$). Opposite sign events passing all the analysis cuts $\text{L}_i,\ i \in \{1, \ldots, 13\}$ except the cut (L_8) on the dilepton system energy are shown (see Tab. 13.9).

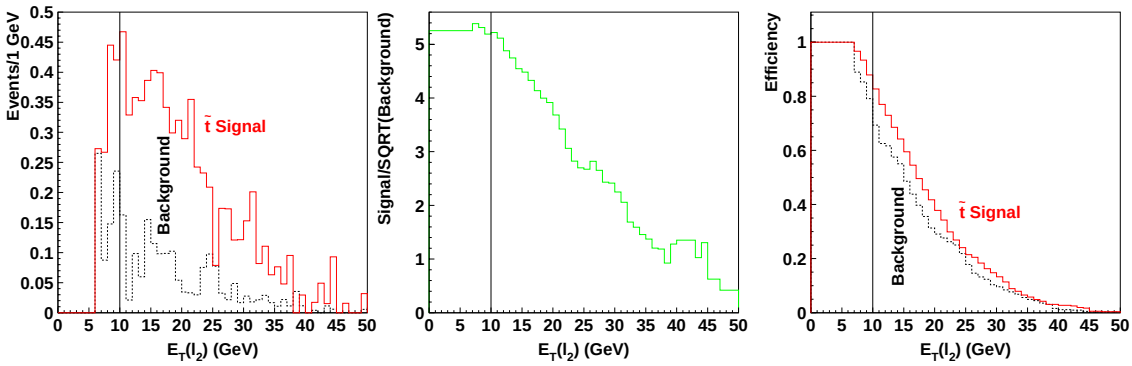

Figure 13.21. The distribution of the loose lepton energy for expected stop signal (assuming $m_{\tilde{t}} = 120$ GeV/c^2 and $m_{\tilde{\nu}} = 60$ GeV/c^2) and background in Run 1B, $\int Ldt = 107\ pb^{-1}$. The last bin contains the overflows. Also shown the S/$\sqrt{\text{B}}$ variable and the efficiency as a function of energy cut ($E_T(l_2) \leq X$). Events passing all the analysis cuts $\text{H}_i,\ i \in \{1, \ldots, 13\}$ except the cut (H_3) on the loose lepton energy are shown (see Tab. 13.9).

Table 13.7
Expected background and stop signal (assuming $m_{\tilde{t}} = 120$ GeV/c^2 and $m_{\tilde{\nu}} = 60$ GeV/c^2) in Run 1A of $\int Ldt = 18.6 pb^{-1}$, and Run 1B of $\int Ldt = 88.6 pb^{-1}$. Analysis cuts $H_i,\ i \in \{1, \ldots, 12\}$ of the large $\Delta m(\tilde{t}, \tilde{\nu})$ set were applied (see Tab. 13.9). OS+LS events are shown.

Source	**Run 1A**	**Run 1B**
	N ± Stat.± Syst.	N ± Stat.± Syst.
Drell-Yan	0.06 ± 0.03 ± 0.02	0.22 ± 0.11 ± 0.08
$b\bar{b}$,$c\bar{c}$	0.00 ± 0.00 ± 0.00	0.00 ± 0.00 ± 0.00
$t\bar{t}$	0.10 ± 0.01 ± 0.04	0.46 ± 0.05 ± 0.17
WW,WZ,ZZ	0.13 ± 0.02 ± 0.04	0.60 ± 0.10 ± 0.18
Misidentified Leptons	0.19 ± 0.04 ± 0.04	0.92 ± 0.18 ± 0.18
Total Background	0.48 ± 0.05 ± 0.09	2.21 ± 0.24 ± 0.43
Expected $\tilde{t}\bar{\tilde{t}}$	1.48 ± 0.07 ± 0.55	6.87 ± 0.40 ± 2.61

Table 13.8
Expected background and stop signal (assuming $m_{\tilde{t}} = 120$ GeV/c^2 and $m_{\tilde{\nu}} = 60$ GeV/c^2) in Run I of $\int Ldt = 107 pb^{-1}$. All analysis cuts $H_i,\ i \in \{1, \ldots, 13\}$ of the large $\Delta m(\tilde{t}, \tilde{\nu})$ set were applied (see Tab. 13.9). At this stage $\mathcal{A} = 2.3\%$ and $S/\sqrt{B} = 5.7$.

Source	**Opposite Sign**
	N ± Stat.± Syst.
Drell-Yan	0.28 ± 0.14 ± 0.10
$b\bar{b}$,$c\bar{c}$	0.00 ± 0.00 ± 0.00
$t\bar{t}$	0.54 ± 0.06 ± 0.20
WW,WZ,ZZ	0.70 ± 0.12 ± 0.22
Misidentified Leptons	0.55 ± 0.17 ± 0.16
Total Background	2.07 ± 0.26 ± 0.38
Expected $\tilde{t}\bar{\tilde{t}}$	8.23 ± 0.39 ± 3.12

13.6. Summary of the Cuts Used

Table 13.9
Summary of developed cuts to distinguish stop signal from background. We list two cut paths whose cuts are marked as L_i and H_i. They correspond to slightly different strategies applied when the mass gap $\Delta(m_{\tilde{t}}, m_{\tilde{\nu}}) = m_{\tilde{t}} - m_{\tilde{\nu}}$ between the stop and the sneutrino mass is low (L_i) or high (H_i). Most cuts are identical for both strategies except for L_3 and L_8. The cleanup cuts are grouped under one name.

Cut	Low $\Delta(m_{\tilde{t}}, m_{\tilde{\nu}})$ Gap	High $\Delta(m_{\tilde{t}}, m_{\tilde{\nu}})$ Gap	Cut
L_1	SUSY Dilepton ID		H_1
L_2	Stop Search Lepton ID		H_2
$\boxed{L_3}$	$p_T(l_2) \geq 6$ GeV/c	$p_T(l_2) \geq 10$ GeV/c	$\boxed{H_3}$
L_4	Cleanup Cuts: Good Runs; Good Vertex; $m(l_1, l_2) \geq 6$ GeV/c^2; $m(ee$ or $\mu\mu) \geq 12$ GeV/c^2; Z^0 removal; Trigger Path	Cleanup Cuts	H_4
L_5	At least 1 Jet		H_5
L_6	$\not{E}_T \geq 30$ GeV		H_6
L_7	$\Delta\phi(l_1, \not{E}_T) \geq 30°$.AND.$\Delta\phi(l_2, \not{E}_T) \geq 30°$		H_7
$\boxed{L_8}$	$E_T(l_1 l_2) \leq 30$ GeV	$E_T(l_1 l_2) \leq 55$ GeV	$\boxed{H_8}$
L_9	$\Delta\phi(l_1 l_2, \not{E}_T) \geq 30°$		H_9
L_{10}	.NOT.($\Delta\phi(l_1$,jet)$\geq 90°$ .AND. $\Delta\phi(l_2$,jet)$\geq 90°$)		H_{10}
L_{11}	$E_T(l_1) + E_T(l_2) \leq 75$ GeV		H_{11}
L_{12}	$\not{E}_T + E_T$(central jet)≤ 160 GeV		H_{12}
L_{13}	Opposite Sign Leptons		H_{13}

13.7. Opening the Box

We developed using the "blind analysis" strategy selection cuts (Tab. 13.9) that enhance our stop signal sensitivity in both the high and small $\Delta m(\tilde{t}, \tilde{\nu})$ region while they significantly reduce the known background. While still "blind", we choose the better of the (L_3, L_8) or (H_3, H_8) cuts for each $(m_{\tilde{t}}, m_{\tilde{\nu}})$ point. This becomes our final ensemble of cuts. We next finish the blind analysis: "Opening the box", we apply the find ensemble of cuts to our preselected 176 data events and search for the supersymmetric partner of the top quark. With both small and large $\Delta m(\tilde{t}, \tilde{\nu})$ sets of cuts we observed zero events in the signal region and two events in the like sign background region, in both cases consistent with the expected background. As a consistency check post-box-opening, we also sequentially applied each selection cut to the data and compared the number of passing events with the expected background. The event reduction is shown in Tab. 13.10. We find our data to be consistent with the predicted background at each stage of the selection cuts.

Table 13.10
Comparison of event reduction for data, expected background and stop signal. Stop A scenario represents the small $\Delta(m_{\tilde{t}}, m_{\tilde{\nu}})$ with $m_{\tilde{t}}$ ($m_{\tilde{\nu}}$) = 100 (75) GeV/c^2. Stop B scenario represents the large $\Delta(m_{\tilde{t}}, m_{\tilde{\nu}})$ with $m_{\tilde{t}}$ ($m_{\tilde{\nu}}$) = 120 (60) GeV/c^2. We show also the sequential effect of the L_3, L_8 cuts on the high $\Delta(m_{\tilde{t}}, m_{\tilde{\nu}})$ stop B, and the final effect of the H_3, H_8 cuts on the low $\Delta(m_{\tilde{t}}, m_{\tilde{\nu}})$ Stop A scenario. The effect of the final ensemble of cuts on other stop and sneutrino mass combinations is shown in Tab. H.1

Applied Cuts		Data	Background	Stop A	Stop B
L_{1-5}	Preselection	176	155.3	23.6	34.5
L_6	$\not\!\!E_T \geq 30$ GeV	32	33.0	13.3	25.8
L_7	$\Delta\phi(l_1, \not\!\!E_T) \geq 30^\circ$ $\Delta\phi(l_2, \not\!\!E_T) \geq 30^\circ$	14	17.5	9.1	20.3
Low	$\boxed{L_8}$ $E_T(l_1 l_2) \leq 30$ GeV	8	5.3	8.0	7.8
Δm	L_9 $\Delta\phi(l_1 l_2, \not\!\!E_T) \geq 30^\circ$	6	4.4	7.0	7.4
L_{10}	$\Delta\phi(l_1$,jet)$< 90^\circ$ or $\Delta\phi(l_2$,jet)$< 90^\circ$	6	3.2	6.4	6.5
L_{11}	$E_T(l_1) + E_T(l_2) \leq 75$ GeV	2	2.3	6.0	5.5
L_{12}	$\not\!\!E_T + E_T$(jet)≤ 160 GeV				
L_{13}	Opposite Sign	0	1.5 ± 0.5	5.7 ± 2.1	5.4 ± 2.0
High Δm	Other cuts				
H_3	$E_T(l_2) \geq 10$ GeV				
$\boxed{H_8}$	$E_T(l_1 l_2) \leq 55$ GeV	2	2.7	3.5	8.3
	Opposite Sign	0	2.1 ± 0.5	3.5 ± 1.3	8.2 ± 3.1

14. Uncertainties

In this section we describe the systematic and statistical uncertainties on the number of expected signal and background events in our search sample. The expected signal events are obtained from Monte Carlo generation. Similarly, for the expected heavy flavor, Drell-Yan, WW, WZ, ZZ background events. But there is an additional source of background events: the misidentified lepton events, which are very difficult to simulate. Therefore we studied them using CDF Run 1 data samples which are independent of our dilepton stop search sample.

The number of Monte Carlo generated events (N^{MC}) is given by:

$$N^{MC} = \int \sigma \cdot BR \cdot \frac{\epsilon^{DATA}}{\epsilon^{MC}} \cdot \epsilon_{sel} \cdot Ldt \ , \tag{14.1}$$

where σ is the cross section of the process of interest, BR is the involved branching ratio of decays of interest, $\frac{\epsilon^{DATA}}{\epsilon^{MC}}$ is the product of various efficiency corrections (see Sec. 11), ϵ_{sel} is the product of efficiencies of selection cuts. For both signal and background we determine the systematic uncertainties due to each term in (14.1) in the following sections.

The number of expected fake events (N^{FAKE}) has been estimated in Sec. 10.2.6 and the calculation of its systematic uncertainty will be described in Sec. 14.1.11.

The discussion of the statistical uncertainties on N^{MC} and N^{FAKE} is described in Sec. 14.2. The systematic and statistical uncertainties on the expected signal were combined into a total uncertainty and were used in setting the upper limit on stop production. For total background uncertainty, we combined the systematic and statistical uncertainties of N^{MC} with the systematic and statistical uncertainties of N^{FAKE}.

14.1. Systematic Uncertainties

14.1.1. Production Cross Section Uncertainty

The uncertainty on the production cross section of a process directly influences the uncertainty on the number of produced events. The Drell-Yan and $t\bar{t}$ cross sections used in MC generations were scaled to the CDF measurements (see Sec. 11.3 for details). Therefore we use the uncertainty of those measurements, 15% and 26% as their cross section uncertainties. The generated $b\bar{b}$ and $c\bar{c}$ events were compared to CDF electron-muon data with a 26% precision[70] which we use as the uncertainty of its cross section. The diboson production cross sections were adjusted to next-to-leading order calculations, reducing the Q^2 scale uncertainty compared to Born level calculations significantly.

The uncertainty of the number of expected signal events due to effects influencing the stop production cross section are discussed below.

14.1.2. Q^2 Scale Uncertainty

The amount of energy, Q, transfered during the collision of partons plays an important role when we generate signal and background Monte Carlo events. It is this quantity to which both the renormalization and factorization scales are usually set. In ISAJET, the nominal Q^2 scale in the stop quark production is taken to be

$$Q^2 = \mathrm{Max}(\frac{2\hat{u}\hat{s}\hat{t}}{\hat{u}^2 + \hat{s}^2 + \hat{t}^2}, 4m_{\tilde{t}}^2), \tag{14.2}$$

where $\hat{u}$, $\hat{s}$, and $\hat{t}$ are the Mandelstam variables.

The renormalization scale is a parameter, at which the strong coupling constant, α_s, is calculated from the renormalization group equation (RGE). Since the matrix elements of color particle production depend on α_s, this suggests a strong dependence of strong production cross sections on Q. This is true for leading order perturbative calculations, but as we include next-to-leading order (NLO) calculations, the depen-

dence on Q weakens and vanishes as we approach the non-perturbative true value of the cross section. Since in our analysis we use the NLO calculation for the stop-antistop pair production cross section, the effect of the choice of the Q on this cross section is very small.

The factorization scale is a parameter, at which the Altarelli-Parisi RGE equations for the dependence of the parton distribution functions on the transfered energy are evaluated. Therefore, the PDF's depend on Q which then has a large impact on many kinematic variables used to detect the stop signal and ultimately affects the selection efficiencies. In order to determine the effect of the choice of the Q used on our expected stop signal, CDF has adopted a procedure, where Q is varied between $\frac{Q}{2}$ and $2Q$. Then the maximum variation (from nominal Q) of the number of MC events (after final selection cuts) is taken to be the uncertainty due to the choice of Q scale. In general, an increase of Q leads to more energy being transfered into the transverse plane. This gives a higher boost to the produced stop anti-stop pairs and causes them to be more back-to-back, which leads to some cancellations of missing $\mathrm{E_T}$, lowering the number of expected events. It also means that the stop decay products acquire in general more energy (thus acts tending to increase the number of expected signal events). The stop decay products also tend to be more in the direction of the parent stop, therefore the leptons will be less isolated. This tends to lower the expected number of stop events.

In the other case, when the available Q is reduced, the above effects act in the opposite direction. The decay products tend to be less energetic (decreasing the number of expected events) but their angular dependences are less pronounced (this decreases the average cancellations of $\not\!\!\mathrm{E}_\mathrm{T}$). We found that the relative signal uncertainty due to the Q scale is 32% (30.2%) for the small (large) mass gap $\Delta(m_{\tilde{t}}, m_{\tilde{\nu}})$ set of cuts respectively.

14.1.3. Uncertainty Due to the Choice of the Structure Function

The choice of the parton distribution function (PDF) has an effect on the cross section of MC processes but also on the distribution of kinematic variables. Therefore it affects both the signal and background Monte Carlo generation results.

We used the CTEQ-3 PDF in the Monte Carlo to generate the stop signal. In order to study the uncertainties due to this choice, we generated for the nominal point ($m_{\tilde{t}} = 100$ GeV/c^2, $m_{\tilde{\nu}} = 75$ GeV/c^2) samples with other PDF's, namely with MRSD0', GRV94 and GRV. For the uncertainty, we took the largest deviation of the acceptance from the nominal CTEQ-3 acceptance. We found that the relative uncertainty on the number of expected signal events is 11% (16%) for the small (large) $\Delta(m_{\tilde{t}}, m_{\tilde{\nu}})$ mass gap set of cuts respectively.

The Monte Carlo background simulation was done by using five different structure functions: MRSD0', GRV94, GRV, CTEQ-2, and CTEQ-3. With each of these, we have generated samples of $b\bar{b}$, $c\bar{c}$, Drell-Yan, $t\bar{t}$ and diboson events, of approximately the same integrated luminosity (an order of magnitude larger then the luminosity of the data sample). For each background type, all five sets were used to obtain the nominal number of background events. The largest deviation (from nominal) of the number of background events, when separate PDFs were used, was taken to be the uncertainty due to the choice of PDF. In order to ensure enough statistics, all this has been done at the preselection stage, see Sec. 12. The uncertainties on the background due to the choice of PDF obtained from Run 1B MC samples are summarized in Tab. 14.1. When the uncertainties were asymmetric, we conservatively chose the larger value and symmetrized it. The results are listed in Tabs. 13.5-13.8. Since these uncertainties are correlated, we linearly sum them up to receive their contribution to the total uncertainty of the background estimation.

Table 14.1
Systematic uncertainties due to the choice of PDF studied on Run 1B Monte Carlo samples. Table shows the number of expected background events and their uncertainties at the preselection level. In case of the large mass gap cuts, we tightened the $E_T(l_2)$ cut to be larger than 10 GeV

Source	Small Mass Gap		Large Mass Gap	
	Opposite Sign	Like Sign	Opposite Sign	Like Sign
$b\bar{b}c\bar{c}$	$35.51^{+23.66}_{-13.6}$	$13.41^{+13.76}_{-4.72}$	$8.55^{+8.69}_{-2.57}$	$3.60^{+3.57}_{-1.47}$
Drell-Yan	$42.83^{+5.12}_{-8.1}$	$0.33^{+0.19}_{-0.23}$	$33.90^{+3.68}_{-4.67}$	$0.11^{+0.11}_{-0.11}$
$t\bar{t}$	$7.83^{+0.31}_{-0.95}$	$0.46^{+0.02}_{-0.04}$	$7.33^{+0.50}_{-0.96}$	$0.32^{+0.02}_{-0.06}$
Dibosons	$3.15^{+0.7}_{-0.43}$	$0.33^{+0.04}_{-0.03}$	$3.00^{+0.75}_{-0.44}$	$0.31^{+0.06}_{-0.02}$

14.1.4. Jet Energy Scale Uncertainty

The calibration of calorimeters has been done with the help of test beam, radioactive and laser sources. These calibration data were then used to set the absolute energy scales of the calorimeters. These values are know with a precision of 5%. The uncertainties in the energy scale of the calorimeter effect the energy measurements of particles and the determination of the energy misbalance of the detector[1]. Therefore they affect our selection efficiencies and must be included in the estimation of the final uncertainties of both signal and background. In order to estimate the uncertainty of our results due to the uncertainty of the absolute energy scale, we vary up and down the jet energies and the missing energy in both signal and background events by 5%. We obtained the relative uncertainty on the expected number of background events to be $\delta N^{background} = \pm 5\%$.

In case of the stop signal, we studied this uncertainty on the two nominal stop and sneutrino mass combinations $m_{\tilde{t}} = 120$ GeV/c^2, $m_{\tilde{\nu}} = 60$ GeV/c^2 ($m_{\tilde{t}} = 100$ GeV/c^2 and $m_{\tilde{\nu}} = 75$ GeV/c^2) representing a typical large and small mass gap between the stop and the sneutrino masses. We expect the uncertainties to differ somewhat in

[1]They also affect the calorimeter isolation determination, but in our analysis we use only tracking isolation of leptons

these two cases. If we lower the jet energies by 5% when the $\Delta(m_{\tilde{t}}, m_{\tilde{\nu}})$ mass gap is small, we can expect some of the low energy jets not to be reconstructed, whereas when the gap is large, jets are more energetic and the loss of a few GeV energy might not be significant. In case of the small $\Delta(m_{\tilde{t}}, m_{\tilde{\nu}})$ mass gap, the uncertainty was found to be $\delta N^{signal} = \pm 11\%$, larger; for of the large $\Delta(m_{\tilde{t}}, m_{\tilde{\nu}})$ mass gap it is smaller: $\delta N^{signal} = \pm 3\%$.

14.1.5. Uncertainty Due to Gluon Radiation

The presence of gluon radiation in events is a higher order QCD process and therefore very difficult to incorporate in Monte Carlo generation. The amount of gluon radiation in events affects the number of energetic jets and impacts the selection efficiencies. The jet multiplicities of background events from our parton shower Monte Carlo generators are in a good agreement with data and we do not further study possible uncertainties due to uncertainties of gluon radiation.

With the signal, we cannot compare the results of MC generation to SUSY top data, therefore we determine the effect of the gluon radiation on our expected signal by taking for the uncertainty half of the difference (from nominal case, when the gluon radiations are switched on) of the expected signal events when the final state gluon radiation is switched off. This uncertainty is found to be 6.9% for both the large and small mass gap nominal points.

14.1.6. Lepton Trigger Efficiency Uncertainty

Previous multilepton analyses determined the trigger efficiencies of the triggers with which our data have been collected (see [55] and references therein). The uncertainties on the trigger efficiencies were found by varying the parameterized trigger efficiency curves by one standard deviation. The uncertainty entering both the signal and background determination is 4.9%.

14.1.7. Lepton ID Efficiency Uncertainty

The detector simulations tend to overestimate the lepton identification efficiencies by a small fraction (see Sec. 11.1.2). The lepton ID efficiencies were previously studied in [56]. As we described in Sec. 11.1.2, we correct the Monte Carlo results for the difference found between the lepton identification efficiencies in MC and real data events. The uncertainty is taken to be half of the difference of the MC and data lepton ID efficiencies. This uncertainty is 2.5% and affects both the number of expected signal and background events.

14.1.8. Lepton Tracking Isolation Efficiency Uncertainty

Multiple primary interactions in the beam crossing affect the tracking isolation variable but were not included to MC (see Sec. 11.1.2). We correct the MC results for the difference observed between the tracking isolation efficiency in MC and data.

The uncertainty due to the tracking isolation efficiencies is taken to be the of the difference between the MC lepton tracking isolation efficiencies and the data lepton tracking isolation efficiencies previously studied in [56]. This uncertainty is 1.0% and affects both the number of expected signal and background events.

14.1.9. Uncertainty on Integrated Luminosity

As mentioned previously, the luminosity is measured by the beam-beam counters (BBC). Most of the uncertainty of the luminosity measurement comes from the uncertainty on the normalization of the BBC data. We take the reported uncertainty [71] of 4.1% of the Run 1A + Run 1B total integrated luminosity.

14.1.10. Fake Rates Uncertainties

Lepton misidentification rates $\mathcal{P}$ were calculated (Sec. 10.2.4) as the ratio of the number of found fake leptons in a given p_T bin to the number of tracks in that p_T bin,

$\mathcal{P}^i_{\rm lepton}(\rm p_T) \equiv \frac{N^i_{\rm lepton}(\rm p_T)}{N^i_{\rm tracks}(\rm p_T)}$. They were studied in two very different data samples (Minimum Bias and Jet 50). Both the shape of the fake rate distributions and the absolute values agreed in those two samples within statistical uncertainties. The fake rate uncertainties are statistics dominated and determined as follows.

The relative uncertainty $\delta\mathcal{P}^i$ on the fake rate $\mathcal{P}^i$ is determined for each $\rm p_T$ bin as the quadratic sum of the relative uncertainties $\delta N^i_{\rm lepton} \equiv \frac{\sqrt{N^i_{\rm lepton}}}{N^i_{\rm lepton}}$ and $\delta N^i_{\rm tracks} \equiv \frac{\sqrt{N^i_{\rm tracks}}}{N^i_{\rm tracks}}$. Then the absolute uncertainty $\Delta\mathcal{P}^i = \mathcal{P}^i\delta\mathcal{P}^i$ is calculated. The results are listed in Tabs. 10.1-10.5 and graphically shown as a band around the fake rate distributions in Figs. 10.4-10.8.

14.1.11. Uncertainties of Fakes' Contributions to the Dilepton Sample

The contribution of the misidentified leptons (N^{fakes}) to our dilepton sample is described in Sec. 10.2.5. The absolute uncertainty ΔN^{fakes} was obtained by calculating the change in the number of found fakes $N^{fakes} + \Delta N^{fakes}$ ($N^{fakes} - \Delta N^{fakes}$) when the $\mathcal{P}^i + \Delta\mathcal{P}^i$ (or equivalently $\mathcal{P}^i - \Delta\mathcal{P}^i$) were used as the fake rates. The relative uncertainty of the fake contributions to the dilepton sample is then 30%.

14.2. Statistical Uncertainties

In this section we discuss the statistical uncertainties of weighted events. We denote the search data sample's integrated luminosity by $L^{search} = \int \mathcal{L}\rm dt = 107.2\ pb^{-1}$. The total integrated luminosity of a Monte Carlo generated sample[2] is denoted by L^{gen}, with an integer number, N^{gen}, of generated events. Then in L^{search} we expect to see a number of events $N^{search} = \frac{L^{search}}{L^{gen}} N^{gen} = \sum_{i=1}^{N^{gen}} 1 * wgt$, where $wgt = \frac{L^{search}}{L^{gen}}$ denotes the weight that of each generated event. Note that N^{search} is in general

[2]In order to have large statistics of MC samples even after all selection cuts were applied, and the number of expected events is small, it is necessary to generate a large integrated luminosity sample and scale the MC results to the integrated luminosity of the search data sample.

a non-integer. The question of interest then is, what is the statistical uncertainty ΔN^{search}?

Each event's absolute uncertainty[3] is $1 * wgt$. Since events are assumed to be statistically independent, we sum up their absolute uncertainties in quadrature and obtain:

$$\Delta N^{search} = \sqrt{\sum_{i=1}^{N_{gen}} wgt^2}$$

Furthermore, we impose selection cuts on N^{gen} reducing it to n^{gen}. We also impose various efficiency corrections which alter event weights on an event by event basis. Therefore, the wgt quantity receives an index $i \in \{1, \ldots, n^{gen}\}$. Then the number of expected MC events, n^{search}, in the search sample is given by

$$n^{search} = \sum_{i=1}^{n^{gen}} wgt_i, \qquad \Delta n^{search} = \sqrt{\sum_{i=1}^{n^{gen}} wgt_i^2}$$

where Δn^{search} is the absolute uncertainty of n^{search}. Notice, that these results show the reason to generate as much MC data as possible, because with $L^{gen} \gg L^{search}$ the weights are $wgt_i \ll 1.0$ which leads to very small statistical uncertainty Δn^{search}.

The statistical uncertainties were calculated for the stop signal and also for the background and are about 5%.

14.3. The Total Uncertainty

The systematic uncertainties of the expected numbers of signal and background events were determined by using the Run 1B Monte Carlo files. The relative uncertainties from each source were then translated to Run 1A MC events as well. Since we used the same[4] MC files for Run 1A and Run 1B signal and background estimation, their uncertainties are correlated and we linearly combine them to obtain the total Run 1 uncertainties from each source (see Tab. 14.2). Then the absolute uncertainties

[3] In case of $N = 1$ event, both the Poisson (N) and the Gaussian ($\sqrt{N}$) uncertainties are identical.
[4] of course with their appropriate trigger efficiencies

Table 14.2
The relative systematic and statistical uncertainties (in %) on the number of expected signal and background events in Run 1.

Source	Small Mass Gap Cuts		Large Mass Gap Cuts	
	Stop Signal	Background	Stop Signal	Background
$\sigma \cdot Br$	-	12.2	-	11.8
Q^2	32	-	30.2	-
PDF's	11	38	16	29
Jet Energy Scale	11	5	2.8	5
Gluon Radiation	6.9	-	6.9	-
Lept Trigg	4.9	4.9	4.9	4.9
Lept ID	2.5	2.5	2.5	2.5
Lept Trk ISO	1.0	1.0	1.0	1.0
Luminosity	4.1	4.1	4.1	4.1
Fakes	-	30	-	30
Stat. Uncert	7.8	19.7	4.7	12.6
TOTAL:	37.8	30.0	36.0	23.8

of various sources were combined in quadrature, and the total uncertainty listed in Tab. 14.2 was calculated.

The statistical uncertainties were calculated separately for Run 1A and Run 1B events and (since they are correlated) were linearly combined to obtain the statistical uncertainties of the Run 1 sample. In the case of the stop signal, the statistical uncertainties were calculated for each point separately.

Tab. 14.2 summarizes the relative uncertainties found on the number of Run 1 expected signal and background events after the final selection cuts have been applied. The results of using both the high and low $\Delta(m_{\tilde{t}}, m_{\tilde{\nu}})$ groups of cuts is shown.

15. Results and Setting Mass Limits

We have done a "blind" search for the stop quark. This means the collected data were explored only with loose preliminary cuts, where the expected signal is still swamped by background, until we developed the sets of selection cuts (done on MC generated events and "fake lepton" events simulated from non-search-sample CDF data) that would distinguish in a statistically significant way the stop signal from expected backgrounds. After applying the selection cuts to the search data sample, no evidence was found for the existence of a light stop quark that would decay into a light sneutrino, lepton and a bottom quark. The zero observed events are consistent with the expected small background. This allowed us (see below) to set a 95% confidence level (C.L.) upper limit on the number of signal events which could have been in a search sample of this size.

Since the number of experimentally observed events n_0 is a result of drawing from a Poisson distributed variable whose mean is μ, the probability of observing n_0 events is given by

$$P(n_0;\mu) = \frac{\mu^{n_0} e^{-\mu}}{n_0!} \ .$$

We wish to find a real number N, such that there is a probability ϵ to observe n_0 or fewer events, (*i.e.* a probability $1-\epsilon$ to observe more than n_0 events)

$$\epsilon = \sum_{n=0}^{n_0} P(n;N) = \sum_{n=0}^{n_0} \frac{N^n e^{-N}}{n!} \ .$$

If the predicted number of events for a given $m_{\tilde{t}},\ m_{\tilde{\nu}}$ exceeds N, there is even less than ϵ probability of seeing as few events as are observed, and we are able to rule out such region of $m_{\tilde{t}},\ m_{\tilde{\nu}}$ parameter space with even greater than $1-\epsilon$ confidence level. In our case $n_0 = 0$ events[1]. We have $0.05 = P(0;N) = \frac{N^0 e^{-N}}{0!}$, therefore $N =$

[1]Since we do not observe any events, we also do not observe any background μ_b among them and our formulae will be somewhat simpler than the ones which include possible background subtraction.

$-\ln 0.05 = 2.99$. This result tells us that with a 95% probability, at most three stop signal events statistically, might have been observed in the data. Therefore, any mass combination of stop and sneutrino predicting more than three events after all selection cuts were placed is excluded with 95% probability. This would be true, if we were able to predict the possible stop signal events without any uncertainty. In Sec. 14.3, we found a combined theoretical and experimental uncertainty of $\delta_{signal} = 37.8\%$. To incorporate them into the upper limit N, we must determine the mean of a Poisson distribution which is "smeared" by a Gaussian distribution of width δ_{signal}, such that the probability of observing zero events is 95%. While for the no-uncertainty case we were able to find an analytic solution, we use a Monte Carlo procedure to fold in the uncertainties.

The CDF experiment has adopted the following method of determining the upper limit N for non-zero δ_{signal}. We assume a Gaussian distribution $G(N, \delta_{signal}) = \frac{1}{\sqrt{2\pi\delta^2_{signal}}} e^{-\frac{(x-N)^2}{2\delta^2_{signal}}}$ with mean N and width δ_{signal}. We assume a Poisson probability distribution $P(n_0, N) = \frac{N^{n_0} e^{-N}}{n_0!}$ for the measured number of events n_0 with a mean N. This N is to be determined. We start from an arbitrary initial value of N denoted N_{init}. We randomly generate a real ν according to $G(N_{init}, \delta_{signal})$. We repeat this 10,000 times. We count how many times (denoted c) we obtain a non-negative ν such that after using it as the mean of a Poisson distribution we generate an integer number that is greater than n_0. The ratio $\frac{c}{10000}$ is called ϵ_{init}. Then we check if this ϵ_{init} coincides with the desired ϵ (of course within desired precision). If not, the initial guess N_{init} is adjusted to N_1 and with the above procedure ϵ_1 (instead of ϵ_{init}) is determined. We repeat the search for N_i until the desired confidence level $1 - \epsilon_i = 1 - \epsilon$ is reached. We use `poilim.f`, a CDF program[72] for executing the above procedure.

In our case, when we observed $\boxed{n_0 = 0}$ events with the uncertainty of the expected signal being $\boxed{\delta_{signal} = 37.8\%}$ the 95% C.L. upper limit of stop events in the data is determined to be $\boxed{N = 4.01}$ events. This allows us to exclude at 95% C.L. any stop

and sneutrino mass combination (listed in Tab. H.1), that predicts[2] at least 4.01 signal events in the CDF Run 1 data.

The CDF excluded region is graphically shown on Fig. 15.1 as a shaded contour. We also show the results of Fermilab's D$\emptyset$ experiment[73] and CERN's LEP experiments[33, 34, 35] (for the minimum stop mixing angle $\theta = 0^\circ$ *i.e.* the maximal reach). The band at $m_{\tilde{\nu}} = 44.7$ GeV is the current most general, model independent upper limit on the sneutrino mass[13]. Our exclusion contour starts at $m_{\tilde{t}} = 80$ GeV/c^2 because those are the lowest stop mass Monte Carlo points we have generated to have a good overlap with LEP's excluded region. Close to the kinematic limit, $m_{\tilde{t}} \geq m_{\tilde{\nu}} + m_b$, our sensitivity is limited by the ability to detect the low energetic leptons and jets, eventually losing the stop signature, i.e the required two leptons and jet. In the high stop mass region, our reach is determined by the rapidly falling stop production cross section. In contrast to the D$\emptyset$ strategy, with our selection cuts, we select a kinematic region with the smallest possible background and large enough signal[3]. This way, we minimize the impact of the rather large systematic uncertainties on our result.

The maximum sneutrino mass we exclude is $m_{\tilde{\nu}} = 88.4$ GeV/c^2 for $m_{\tilde{t}} = 126 - 127$ GeV/c^2 . The highest stop mass we reach is $m_{\tilde{t}} = 135$ GeV/c^2 for $m_{\tilde{\nu}} = 72 - 79$ GeV/c^2 .

[2]with either the high or low $\Delta(m_{\tilde{t}}, m_{\tilde{\nu}})$ mass gap set of cuts

[3]If we loosen some of the cuts designed to distinguish stop signal from top background, we would gain back some signal events compensating the falling cross section, but with the available integrated luminosity we would not be able to distinguish them anymore from the $t\bar{t}$ background.

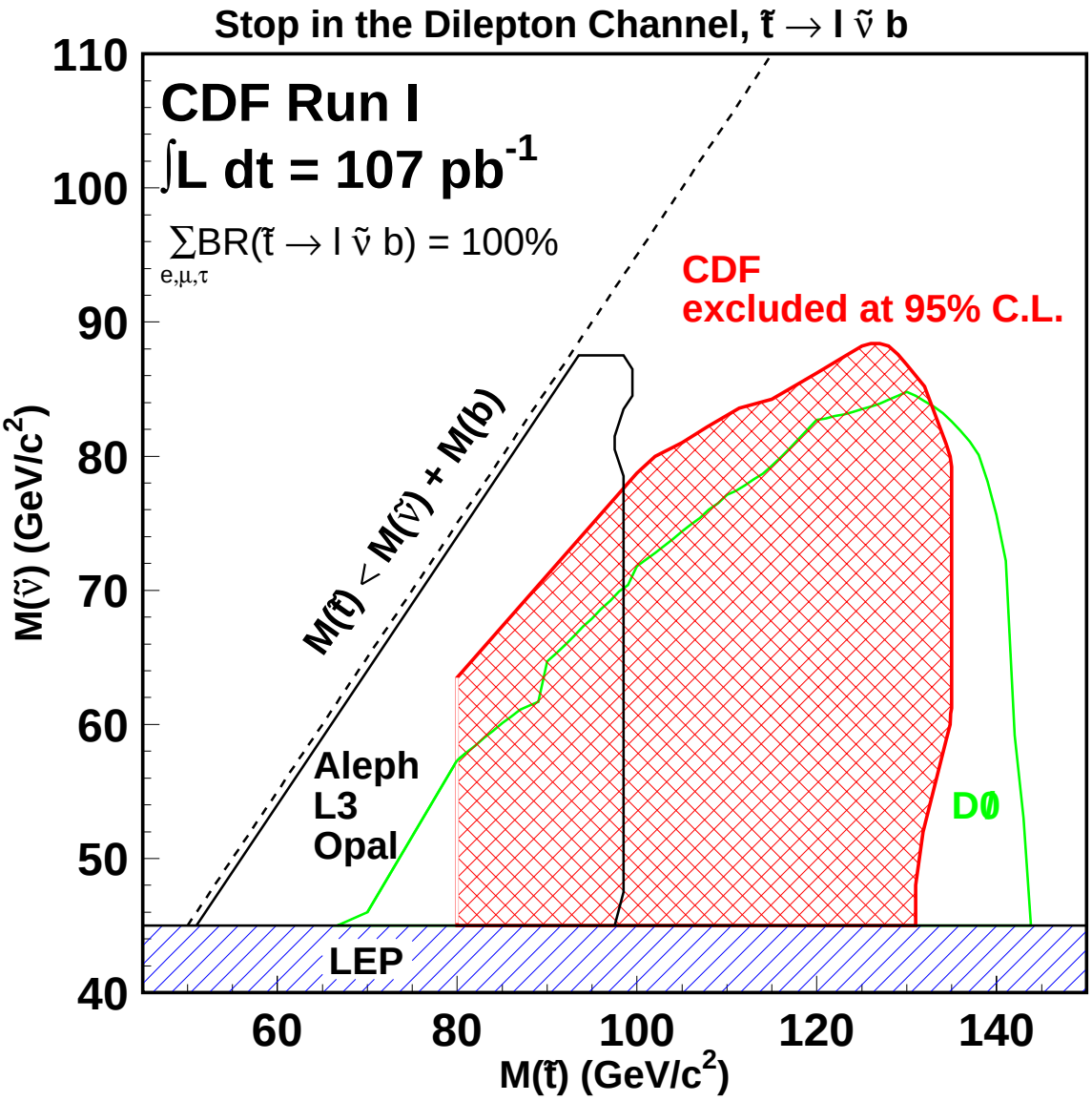

Figure 15.1. CDF 95% C.L. excluded region in the $m_{\tilde{t}}$, $m_{\tilde{\nu}}$ parameter plane. For the 3-body stop decay, $\tilde{t} \rightarrow l\tilde{\nu}b$, a 33.3% branching ratio to each of the three lepton flavors is used.

16. Conclusion

In the work documented in this thesis we searched for the presence of the supersymmetric partner of the top quark in $\int \mathcal{L}\mathrm{dt} = 107.2\ pb^{-1}$ of the Run 1 dilepton data sample collected by the CDF experiment at Fermilab. Stop anti-stop pairs would be strongly pair produced at the Tevatron if kinematically allowed. We considered the three body decay of the stop quark $\tilde{t} \to bl\tilde{\nu}$ to dominate, taking 100% of the branching ratio with $l \in \{e, \mu, \tau\}$. The signature the stop-antistop pairs would leave in the detector would denote the presence of energetic, opposite electric charge leptons, bottom quark jets and substantial missing transverse energy. The main background mimicking this signature comes from events with $t\bar{t}$, $b\bar{b}$, $c\bar{c}$ production and decays, Drell-Yan events, diboson production and decays and events with misidentified or non-prompt leptons. The background and stop signal events were generated with the ISAJET generator and they underwent a full CDF detector simulation. We placed selection cuts on various kinematic variables in order to enhance the statistical significance of stop events in the data while at the same time reducing the background. We found that the relative uncertainty in determining the amount of stop events in the data was 37.8%. We observed zero events in agreement with the predicted background. This allowed us to set an upper limit of 4.01 events on the amount of stop signal in the data and we determined our excluded region in the stop versus sneutrino mass plane. The highest stop mass we were able to reach was $m_{\tilde{t}} = 135\ \mathrm{GeV}/c^2$ and the highest excluded sneutrino mass was $m_{\tilde{\nu}} = 88.4\ \mathrm{GeV}/c^2$. We observed no sign of supersymmetry manifesting itself in our data, and we look forward to the results of Run 2 at Fermilab and, later, the results from the Large Hadron Collider of CERN, both of which will extend the reach of the analysis presented here.

LIST OF REFERENCES

LIST OF REFERENCES

[1] S. Weinberg. *Phys.Rev.Lett.*, 19:1264, 1967.

[2] A. Salam. Elementary particle theory:relativistic groups and analyticity. In *8th Nobel Symposium*, 1968.

[3] J. Illiopoulos, S. L. Glashow, and L. Maiani. *Phys.Rev.D*, 2:1285, 1970.

[4] H. P. Nilles. *Phys.Rep.*, 110:1, 1984.

[5] H. E. Haber and G. L. Kane. *Phys.Rep.*, 117:75, 1985.

[6] M. F. Sohnius. *Phys.Rep.*, 128:39, 1985.

[7] G. Arnison et al. *Phys.Lett.B*, 122:103, 1983.

[8] P. W. Higgs. *Phys.Lett.*, 12:132, 1964.

[9] CDF Collaboration. *Phys.Rev.Lett.*, 74:2626, 1995.

[10] K. Kodama et al. *Phys.Lett.B*, 504:218, 2001.

[11] M. Kobayashi and T. Maskawa. *Prog.Theoret.Phys.*, 49:652, 1973.

[12] SNO Collaboration. *Phys.Rev.Lett.*, 89:011301, 2002.

[13] E. J. Weinberg et al. *Phys.Rev.D*, 66:919, 2002.

[14] C. Quigg. *Gauge Theories of the Strong, Weak and Electromagnetic Interactions*. Addison-Wesley Publishing Company, 1983.

[15] M. Drees. An introduction to supersymmetry. *KEK-TH-501, hep-ph/9611409*, 1996.

[16] D. A. Dicus and V. S. Mathur. *Phys.Rev.D*, 7:3111, 1973.

[17] B. W. Lee, C. Quigg, and H. Thacker. *Phys.Rev.D*, 16:1519, 1977.

[18] M. E. Peskin. Beyond the standard model. *SLAC-PUB-7479, hep-ph/9705479*, 1997.

[19] CDF Collaboration. *Phys.Rev.Lett.*, 82:3206, 1999.

[20] J. D. Lykken. Introduction to supersymmetry. *FERMILAB-PUB-96/445-T, hep-th/9612114*, 1996.

[21] S. P. Martin. A supersymmetry primer. *hep-ph/9709356*, 1997.

[22] F. A. Berezin. *Metod vtoricnovo kvantovania*. Nauka, Moskva, 1965.

[23] C. Klimčík, A. Pompoš, and V. Souček. *Let. in Math. Phys.*, 30:259, 1994.

[24] J. A. Bagger. Weak-scale supersymmetry: Theory and practice. *Lectures at TASI 95, hep-ph/9604232*, 1995.

[25] J. Wess and J. Bagger. *Supersymmetry and Supergravity.* Princeton University Press, Princeton NJ, 2nd edition, 1992.

[26] M. Kaku. *Quantum Field Theory.* Oxford University Press, 1993.

[27] L. Girardello and M. T. Grisaru. *Nuc.Phys.*, B194:65, 1982.

[28] H. E. Haber and G. L. Kane. *Phys.Rep.*, 117:75, 1985.

[29] G. 't Hooft. *Recent Developments in Gauge Theories*, volume 1980. Plenum, New York.

[30] S. Dawson. SUSY and such. In *Nato Advanced Study of Techniques and Computations on HEP*, St. Croix, 1996. hep-ph/9612229.

[31] W. Porod. More on higher order decays of the stop quark. *UWThPh-1998-60,hep-ph/9812230*, 1998.

[32] W. Beenakker et al. *Nuc.Phys.*, B515:3, 1998.

[33] LEP SUSY Working Group ALEPH DELPHI L3 and OPAL Collaborations. *LEPSUSYWG/01-03.1,* `http://lepsusy.web.cern.ch/lepsusy/`, 2001.

[34] LEP SUSY Working Group ALEPH DELPHI L3 and OPAL Collaborations. *LEPSUSYWG/02-01.1,* `http://lepsusy.web.cern.ch/lepsusy/`, 2002.

[35] LEP SUSY Working Group ALEPH DELPHI L3 and OPAL Collaborations. *LEPSUSYWG/02-02.1,* `http://lepsusy.web.cern.ch/lepsusy/`, 2002.

[36] R. Demina, J. D. Lykken, K. T. Matchev, and A. Nomerotski. *Phys.Rev.D*, 62:035011, 2000.

[37] F. Abe et al. The collider detector at fermilab. *Nucl.Instrum.Methods A*, A271, 1988.

[38] D. Gerdes. Study of the conversion removal for the lepton+jets sample. CDF note 2903, unpublished, 1995.

[39] V. D. Barger and R. J. N. Phillips. *Collider Physics.* Addison-Wesley Publishing Company, 1987.

[40] B. Flaugher et al. A guide to JETCLU: the CDF jet cluster algorithm. Technical report, CDF/DOC/JET/CDFR/1813, Fermilab, 1993.

[41] CDF Collaboration et al. *Phys.Rev.D*, 50:2966, 1994.

[42] J. P. Done et al. Run 1A and 1B low-$p_{\rm t}$ dilepton sample. Internal CDF note CDF/ANAL/EXOTIC/CDFR/4446, 1996.

[43] D. Cronin-Hennessy, A. Beretvas, and S. Segler. Getting your luminosity. CDF Internal Note, CDF/DOC/CDFR/4317, 1997.

[44] J. P. Done. SUSY dilepton selection for Run 1B. Internal CDF note CDF/DOC/EXOTIC/CDFR/3472, 1996.

[45] M. Worcester, D. Saltzberg, and J. Nachtman. Development of new isolation variables and estimation of fake rates in dilepton SUSY searches at CDF. Internal CDF note CDF/ANAL/EXOTIC/CDFR/5081, 1999.

[46] S. Tehter. The fake lepton rate for the Run 1B SUSY trilepton analysis. Internal CDF note CDF/ANAL/EXOTIC/CDFR/3566, 1996.

[47] A. Kngeter, T. Muller, and S. Lammel. Track based fake rate calculation for the four-lepton r_p violating SUSY analysis. Internal CDF note CDF/ANAL/EXOTIC/CDFR/5213, 2000.

[48] B. T. Huffman and A. F. Garfinkel. Measuring hadronic backgrounds and the cross section of inclusive muon. Internal CDF note CDF/ANAL/TOP/CDFR/1822, 1992.

[49] B. T. Huffman. Measuring the decay-in-flight cross-section of central muons. Internal CDF note CDF/ANAL/TOP/CDFR/1663, 1992.

[50] Q. F. Wang. A dilepton fake rate study in top search. Internal CDF note CDF/ANAL/TOP/CDFR/2102, 1993.

[51] CDF Collaboration. *Phys.Rev.Lett.*, 76:3070, 1996.

[52] CDF Collaboration. *Phys.Rev.D*, 65:052005, 2002.

[53] S. Gromoll Ch. Paus S. Tkaczyk. Heavy quark cross section predictions for CDF in Run 2. Internal CDF note CDF/DOC/BOTTOM/CDFR/5984, 2002.

[54] H. Baer, F. E. Paige, S. D. Protopopescu, and X. Tata. *BNL-HET-98-39(1998) and hep-ph/9810440. We use ISAJET version 7.20.*

[55] B. Tanenbaum. *A Search for Chargino-Neutralino Production at the Fermilab Tevatron Collider*. PhD thesis, University of New Mexico, 1997.

[56] J. P. Done et al. Study of Run 1B lepton identification efficiencies for SUSY searches. Internal CDF note CDF/ANAL/EXOTIC/CDFR/4218, 1997.

[57] J. P. Done et al. Study of Run 1B lepton isolation efficiencies for SUSY searches. Internal CDF note CDF/ANAL/EXOTIC/CDFR/4291, 1998.

[58] CTEQ Collaboration, H. L. Lai, et al. *Phys.Rev.D*, 51:4763, 1995.

[59] W. Beenakker, R. Höpker, M. Spira, and P. M. Zerwas. *Nuc.Phys.B*, 492:51, 1997.

[60] M. Glück, E. Reya, and A. Vogt. *Z.Phys.C - Particles and Fields*, 69:433, 1995.

[61] A. D. Martin, R. G. Roberts, and W. J. Stirling. *Phys.Lett.B*, 387:419, 1996.

[62] CDF Collaboration. *Phys.Rev.D*, 55:2546, 1997.

[63] CDF Collaboration. *Phys.Rev.D*, 59:052002, 1999.

[64] CDF Collaboration. *Phys.Rev.D*, 49:1, 1994.

[65] CDF Collaboration. *Phys.Rev.D*, 64:032002, 2001.

[66] J. Ohnemus. *Phys.Rev.D*, 44:1403, 1991.

[67] J. Ohnemus. *Phys.Rev.D*, 44:3477, 1991.

[68] J. Ohnemus and J. Owens. *Phys.Rev.D*, 43:3626, 1991.

[69] CDF Collaboration. *Phys.Rev.Lett.*, 84:5273, 2000.

[70] J. P. Done et al. ISAJET monte carlo validation. Internal CDF note CDF/ANAL/EXOTIC/CDFR/4903, 1999.

[71] D. Cronin-Hennessy and A. Beretvas. Luminosity at CDF. CDF Internal Note, CDF/DOC/CDFR/4721, 1998.

[72] J. Conway and K. Maeshima. Poisson upper limits incorporating uncertainties in acceptance and background. CDF/PUB/EXOTIC/PUBLIC/4476, 1998.

[73] D$\emptyset$ Collaboration, V. M. Abazov, et al. *Phys.Rev.Lett.*, 88:171802, 2002.

APPENDICES

Appendix A: Conventions

- $\hbar = c = 1$
- The metric tensor is $\eta^{mn} = \text{diag}(1,\text{-}1,\text{-}1,\text{-}1)$
- The dotted (undotted) indices are for $(0, \frac{1}{2})$ $((\frac{1}{2}, 0))$ spinor representation of the Lorentz group (see Appendix D).
- Weyl spinors with a bar are the left-handed Weyl spinors.
- The "bar" over a Weyl spinor is part of its name and does not signify any kind of conjugation.
- The symbols for superpartners to Standard Model particles have an additional tilde above their notation.
- The "handedness" index of a superpartner to a SM fermion refers to the helicity of the SM fermion.

Appendix B: Chiral Spinors

From a historical point of view, an electron is an object described by a 4-component Dirac spinor, ψ_e, which solves the Dirac equation[1]

$$(i\gamma^\mu \partial_\mu - m)\psi_e = 0, \tag{B.1}$$

where $m = 0.5$ MeV$/c^2$ and the γ^μ are the Dirac matrices defined by the relation

$$\{\gamma^\mu,\ \gamma^\nu\} = 2\eta^{\mu\nu}, \tag{B.2}$$

where $\eta^{\mu\nu}$ is the flat metric tensor. This anticommutation relation defines an algebra called the Clifford algebra. It has 16 generators,

$$I,\ \gamma^u,\ \sigma^{u\nu},\ \gamma^5,\ \gamma^5\gamma^\mu$$

where I is the 4×4 unity matrix, $\sigma^{u\nu} \equiv \frac{i}{2}[\gamma^\mu, \gamma^\nu]$ and $\gamma^5 = i\gamma^0\gamma^1\gamma^2\gamma^3\gamma^4$.

The Dirac representation of the Clifford algebra is given by the following matrices:

$$\gamma^0 = \begin{pmatrix} 1 & 0 \\ 0 & -1 \end{pmatrix} \qquad \gamma^j = \begin{pmatrix} 0 & \sigma^j \\ -\sigma^j & 0 \end{pmatrix} \qquad \gamma^5 = \begin{pmatrix} 0 & 1 \\ 1 & 0 \end{pmatrix} \tag{B.3}$$

where the Pauli sigma matrices are given in Appendix D.

From the 4-component Dirac spinor ψ_e, we can form two 4-component chiral Dirac spinors

$$(\psi_e)_L \equiv \frac{1-\gamma^5}{2}\psi_e, \quad (\psi_e)_R \equiv \frac{1+\gamma^5}{2}\psi_e. \tag{B.4}$$

[1]Similarly for the other spin 1/2 particles

Appendix C: Anticommuting Variables

Grassmann variables θ^α are objects, which satisfy the following anticommutation relations:

$$\{\theta^\alpha, \theta^\beta\} = 0. \tag{C.1}$$

Since $(\theta^\alpha)^2 = 0$, the most general function of a single Grassmann variable has the following form:

$$f(\theta^\alpha) = f_0 + \theta^\alpha f_1,$$

where f_0 and f_1 are complex numbers.

The differentiation rules are

$$\begin{aligned} \partial_\alpha &= \frac{\partial}{\partial\theta^\alpha},\ \partial^\alpha = \frac{\partial}{\partial\theta_\alpha} = -\epsilon^{\alpha\beta}\partial_\beta, \\ \partial_\alpha\theta^\beta &= \delta^\beta_\alpha,\ \partial_\alpha\theta^\beta\theta^\gamma = \delta^\beta_\alpha\theta^\gamma - \delta^\gamma_\alpha\theta^\beta, \end{aligned}$$

The Levi-Civita symbol $\epsilon^{\alpha\beta}$ is defined in Appendix B.

The integration rules for single variable are

$$\begin{aligned} \int d\theta^\alpha\ \theta^\alpha &= 1, \\ \int d\theta^\alpha &= 0, \\ \int d\theta^\alpha\ f(\theta^\alpha) &= f_1 \end{aligned} \tag{C.2}$$

Using the anticommutation relations (C.1), these formulae can be extended to multiple variable systems.

Notation of higher dimensional measures:

$$\begin{aligned} d^2\theta &= -\frac{1}{4} d\theta^\alpha\, d\theta^\beta\, \epsilon_{\alpha\beta}, \\ d^2\overline{\theta} &= -\frac{1}{4} d\overline{\theta}_{\dot\alpha}\, d\overline{\theta}_{\dot\beta}\, \epsilon^{\dot\alpha\dot\beta}, \\ d^4\theta &= d^2\theta\ d^2\overline{\theta}. \end{aligned} \tag{C.3}$$

For more on differentiation or integration see [22] or [20].

Appendix D: Weyl-spinors

The Lorentz group SO(1,3) is isomorphic to SL(2,C). It can be shown that irreducible representations of the Lorentz group (labeled by $(j,\ j')$) can be constructed from irreducible representations of two SU(2) groups labeled by j and j'[26]. In our case we use the spin $j = j' = 1/2$ representations, so we have the two Weyl base spinors [20]

$$\begin{aligned}(\tfrac{1}{2},0) &= \text{left}-\text{handed } 2-\text{component Weyl spinor}\\ (0,\tfrac{1}{2}) &= \text{right}-\text{handed } 2-\text{component Weyl spinor}\end{aligned}$$

In Van der Waerden notation, the undotted indices correspond to $(\frac{1}{2},0)$ and the dotted ones correspond to $(0,\frac{1}{2})$:

$$\begin{aligned}(\tfrac{1}{2},0) &: \psi_\alpha,\\ (0,\tfrac{1}{2}) &: \bar{\psi}^{\dot{\alpha}} \equiv (\psi_\alpha)^*.\end{aligned}$$

Also:

$$\bar{\psi}_{\dot{\alpha}} \equiv (\psi_\alpha)^\dagger; \quad \psi^\alpha \equiv (\bar{\psi}_{\dot{\alpha}})^*. \tag{D.1}$$

The raising and lowering of the indices is done by the 2-dimensional Levi-Civita symbols:

$$\begin{aligned}\epsilon_{\alpha\beta} = \ \epsilon_{\dot{\alpha}\dot{\beta}} &= \begin{pmatrix} 0 & -1 \\ 1 & 0 \end{pmatrix};\\ \epsilon^{\alpha\beta} = \ \epsilon^{\dot{\alpha}\dot{\beta}} &= \begin{pmatrix} 0 & 1 \\ -1 & 0 \end{pmatrix} = i\sigma^2.\end{aligned} \tag{D.2}$$

Thus:

$$\begin{aligned}\psi^\alpha &= \epsilon^{\alpha\beta}\psi_\beta; \qquad \psi_\alpha &= \epsilon_{\alpha\beta}\psi^\beta;\\ \bar{\psi}^{\dot{\alpha}} &= \epsilon^{\dot{\alpha}\dot{\beta}}\bar{\psi}_{\dot{\beta}}; \qquad \bar{\psi}_{\dot{\alpha}} &= \epsilon_{\dot{\alpha}\dot{\beta}}\bar{\psi}^{\dot{\beta}}.\end{aligned} \tag{D.3}$$

Spinor Summation Convention

Let us have two spinors, ψ and χ. Then for their scalar product we have

$$\begin{aligned} \psi\chi &= \psi^\alpha\chi_\alpha &= -\psi_\alpha\chi^\alpha = \chi^\alpha\psi_\alpha = \chi\psi \\ \bar{\psi}\bar{\chi} &= \bar{\psi}_{\dot{\alpha}}\bar{\chi}^{\dot{\alpha}} &= -\bar{\psi}^{\dot{\alpha}}\bar{\chi}_{\dot{\alpha}} = \bar{\chi}_{\dot{\alpha}}\bar{\psi}^{\dot{\alpha}} = \bar{\chi}\bar{\psi} \end{aligned} \tag{D.4}$$

Sigma matrices:

$$\begin{aligned} \sigma^m &= (I, \vec{\sigma}) &= \bar{\sigma}_m, \\ \bar{\sigma}^m &= (I, -\vec{\sigma}) &= \sigma_m, \end{aligned} \tag{D.5}$$

where $\vec{\sigma}$ are the Pauli matrices:

$$\sigma^1 = \begin{pmatrix} 0 & 1 \\ 1 & 0 \end{pmatrix} \qquad \sigma^2 = \begin{pmatrix} 0 & -i \\ i & 0 \end{pmatrix} \qquad \sigma^3 = \begin{pmatrix} 1 & 0 \\ 0 & -1 \end{pmatrix} \tag{D.6}$$

The SL(2,C) generators are defined as

$$\begin{aligned} \sigma_\alpha^{mn\beta} &= \frac{i}{4}\left[\sigma^m_{\alpha\dot{\gamma}}\bar{\sigma}^{n\dot{\gamma}\beta} - \sigma^n_{\alpha\dot{\gamma}}\bar{\sigma}^{m\dot{\gamma}\beta}\right] \\ \bar{\sigma}^{mn\dot{\alpha}}{}_{\dot{\beta}} &= \frac{i}{4}\left[\bar{\sigma}^{m\dot{\alpha}\gamma}\sigma^n_{\gamma\dot{\beta}} - \bar{\sigma}^{n\dot{\alpha}\gamma}\sigma^m_{\gamma\dot{\beta}}\right] \end{aligned} \tag{D.7}$$

Appendix E: From Dirac to Weyl Notation

The notation of the particle content of the SM by using 2-component **left handed** Weyl spinors:

$$
\begin{aligned}
Q_i &= \begin{pmatrix} u \\ d \end{pmatrix}, \ \begin{pmatrix} c \\ s \end{pmatrix}, \ \begin{pmatrix} t \\ b \end{pmatrix} && \text{(E.1)} \\
\overline{u}_i &= \overline{u}, \, \overline{c}, \, \overline{t} && \text{(E.2)} \\
\overline{d}_i &= \overline{d}, \, \overline{s}, \, \overline{b} && \text{(E.3)} \\
L_i &= \begin{pmatrix} \nu_e \\ e \end{pmatrix}, \ \begin{pmatrix} \nu_\mu \\ \mu \end{pmatrix}, \ \begin{pmatrix} \nu_\tau \\ \tau \end{pmatrix} && \text{(E.4)} \\
\overline{e}_i &= \overline{e}, \, \overline{\mu}, \, \overline{\tau} && \text{(E.5)} \\
H_u &= \begin{pmatrix} H_u^+ \\ H_u^0 \end{pmatrix} && \text{(E.6)} \\
H_d &= \begin{pmatrix} H_d^0 \\ H_d^- \end{pmatrix} && \text{(E.7)}
\end{aligned}
$$

where $i = 1, 2, 3$ is the family index. Notice, the bars do not mean any kind of conjugation, they are part of the name.

As an example here, we take the Dirac spinor describing the electron. It is denoted Ψ_D and has two components e_L and e_R

$$(\psi_e)_L = \begin{pmatrix} e_L \\ e_R \end{pmatrix} \tag{E.8}$$

defined by the projection operators $P_{L,R} = (1 \mp \gamma_5)/2$ as follows:

$$P_L(\psi_e)_L = \begin{pmatrix} e_L \\ 0 \end{pmatrix}; \qquad P_R(\psi_e)_L = \begin{pmatrix} 0 \\ e_R \end{pmatrix}. \tag{E.9}$$

We also define e and $\bar{e}$ as two **left handed** Weyl spinors such that $e \equiv e_L$ and $\bar{e} \equiv e_R^\dagger$, so the Dirac spinor (E.8) has the form

$$(\psi_e)_L = \begin{pmatrix} e \\ \bar{e}^\dagger \end{pmatrix} \tag{E.10}$$

Then the kinetic parts of (2.5) and (2.6) can be rewritten into 2-component Weyl-spinor notation:

$$\mathcal{L} = -iQ^{\dagger i}\overline{\sigma}^\mu \partial_\mu Q_i - i\overline{u}^{\dagger i}\overline{\sigma}^\mu \partial_\mu \overline{u}_i - i\overline{d}^{\dagger i}\overline{\sigma}^\mu \partial_\mu \overline{d}_i - iL^{\dagger i}\overline{\sigma}^\mu \partial_\mu L_i - i\overline{e}^{\dagger i}\overline{\sigma}^\mu \partial_\mu \overline{e}_i, \tag{E.11}$$

where we summed over the family index $i = 1, 2, 3$.

For completeness we show also the two component Weyl-spinors for the supersymmetric sector:

$$\tilde{Q}_i = \begin{pmatrix} \tilde{u} \\ \tilde{d} \end{pmatrix}, \begin{pmatrix} \tilde{c} \\ \tilde{s} \end{pmatrix}, \begin{pmatrix} \tilde{t} \\ \tilde{b} \end{pmatrix} \tag{E.12}$$

$$\bar{\tilde{u}}_i = \bar{\tilde{u}}, \bar{\tilde{c}}, \bar{\tilde{t}} \tag{E.13}$$

$$\bar{\tilde{d}}_i = \bar{\tilde{d}}, \bar{\tilde{s}}, \bar{\tilde{b}} \tag{E.14}$$

$$\tilde{L}_i = \begin{pmatrix} \tilde{\nu} \\ \tilde{e} \end{pmatrix}, \begin{pmatrix} \tilde{\nu}_\mu \\ \tilde{\mu} \end{pmatrix}, \begin{pmatrix} \tilde{\nu}_\tau \\ \tilde{\tau} \end{pmatrix} \tag{E.15}$$

$$\bar{\tilde{e}}_i = \bar{\tilde{e}}, \bar{\tilde{\mu}}, \bar{\tilde{\tau}} \tag{E.16}$$

$$\tilde{H}_u = \begin{pmatrix} \tilde{H}_u^+ \\ \tilde{H}_u^0 \end{pmatrix} \tag{E.17}$$

$$\tilde{H}_d = \begin{pmatrix} \tilde{H}_d^0 \\ \tilde{H}_d^- \end{pmatrix} \tag{E.18}$$

where $i = 1, 2, 3$ is the family index.

Appendix F: Run 1A and Run 1B SUSY Dilepton Sample ID Cuts

Table F.1

Run 1A electron (top) and muon (bottom) identification cuts applied to select the Run 1A SUSY dilepton samples. The hemcut is the measure of the amount of energy E allowed to leak to Had calorimeter. It is defined by $0.055 + 0.045(E/100)$. The σ_{charge} requires at least one standard deviation C.L. on determination of the sign of the charge.

Name	TCE	LCE	LPE
Calorimeter	CEM	CEM	PEM
$p_T(GeV/c)$	≥ 6.0	≥ 2.8	-
$E_T(GeV)$	≥ 7.5	≥ 4.0	≥ 4.0
E/P	≤ 2.0	≤ 2.0	-
E_{HAD}/E_{EM}	≤ 0.05	$\leq$ hemcut	≤ 0.1
$LSHR$	≤ 0.2	≤ 0.2	-
$\chi^2_{3\times 3}$	-	-	≤ 3.0
CTC- CES match $\Delta x(cm)$	$\leq$3.0	≤ 3.0	-
CTC- CES match $\Delta z(cm)$	$\leq$5.0	≤ 5.0	-
Strip χ^2	≤ 10.0	≤ 15	-
VTX_{OCCP}	-	-	≥ 0.5
σ_{charge}	≥ 1	≥ 1	≥ 1

Name	TCM	LCM	LXM	LMI
Muon chamber	CMU/CMP	CMU/CMP	CMX	-
$p_T(GeV/c)$	≥ 7.5	≥ 2.8	≥ 2.8	≥ 10.0
$E_{EM}(GeV)$	≤ 2.0	≤ 2.0	≤ 2.0	≤ 2.0
$E_{HAD}(GeV)$	≤ 6.0	≤ 6.0	≤ 6.0	≤ 6.0
Raw d_0 (cm)	≤ 0.5	≤ 0.8	≤ 0.8	≤ 0.8
CTC- CMU match $\Delta x(cm)$	≤ 2.0	≤ 2.0	-	-
or CTC-CMU match χ^2	≤ 9.0	≤ 9.0	-	-
CTC-CMP match $\Delta x(cm)$	≤ 5.0	≤ 5.0	-	-
or CTC-CMP match χ^2	≤ 9.0	≤ 9.0	-	-
CTC-CMX match $\Delta x(cm)$	-	-	≤ 5.0	-
or CTC-CMX match χ^2	-	-	≤ 9.0	-
σ_{charge}	≥ 1	≥ 1	≥ 1	≥ 1

Table F.2
Run 1B electron (top) and muon (bottom) identification cuts applied to select the Run 1B SUSY dilepton samples. The hemcut is the measure of the amount of energy E allowed to leak to Had calorimeter. It is defined by $0.055 + 0.045(E/100)$.

Name	TCE	LCE	LPE
Calorimeter	CEM	CEM	PEM
$p_T(GeV/c)$	≥ 4.0	≥ 2.8	-
$E_T(GeV)$	≥ 8.0	≥ 4.0	≥ 4.0
E/P	≤ 2.0	≤ 2.0	-
E_{HAD}/E_{EM}	≤ 0.05	$\leq$ hemcut	≤ 0.1
$LSHR$	≤ 0.2	≤ 0.2	-
$\chi^2_{3\times 3}$	-	-	≤ 3.0
CTC- CES match $\Delta x(cm)$	$\leq$3.0	≤ 3.0	-
CTC- CES match $\Delta z(cm)$	$\leq$5.0	≤ 5.0	-
Strip χ^2	≤ 10.0	≤ 15	-
VTX_{OCCP}	-	-	≥ 0.5

Name	TCM	LCM	LXM	LMI
Muon chamber	CMU/CMP	CMU/CMP	CMX	-
$p_T(GeV/c)$	≥ 7.5	≥ 1.4	≥ 1.4	≥ 10.0
$E_{EM}(GeV)$	≤ 2.0	≤ 2.0	≤ 2.0	≤ 2.0
$E_{HAD}(GeV)$	≤ 6.0	≤ 6.0	≤ 6.0	≤ 6.0
Raw d_0 (cm)	≤ 0.5	≤ 0.8	≤ 0.8	≤ 0.8
CTC-CMU match $\Delta x(cm)$	≤ 2.0	≤ 2.0	-	-
or CTC-CMU match χ^2	≤ 9.0	≤ 9.0	-	-
CTC-CMP match $\Delta x(cm)$	≤ 5.0	≤ 5.0	-	-
or CTC-CMP match χ^2	≤ 9.0	≤ 9.0	-	-
CTC-CMX match $\Delta x(cm)$	-	-	≤ 5.0	-
or CTC-CMX match χ^2	-	-	≤ 9.0	-

Appendix G: Run 1A and Run 1B Data Trigger Paths

Table G.1

Run 1A SUSY dilepton events passing stop search lepton ID's and cleanup cuts. On a given row the number of events passing the listed trigger, but not passing any of the previous row triggers is shown.

Trigger Status	Run 1A: Level 1 Trigger Name	Events
Required	**L1_CALORIMETER***	**775**
	CMU_CMP_6PT0*	**333**
	CMX_10PT0_HTDC*	**4**
	Total	**1,112**
Not Required	L1_4_PRESCALE*	16
	L1_DIELECTRON*	0
	TWO_CMU_3PT3	10
	TWO_CMU_CMX_3PT3	4
	CEM_CMU_OR_CMX	19
	Total	49
Unidentified Origin	-	0

Table G.2

Run 1A SUSY dilepton events passing stop search lepton ID's, cleanup cuts and the required level 1 triggers. On a given row the number of events passing the listed trigger, but not passing any of the previous row triggers is shown.

Trigger Status	Run 1A: Level 2 Trigger Name	Events
Required	**CEM_9_SEED_9_SH_7_CFT_9_2***	**602**
	CMU_CMP_CFT_9_2	**255**
	CMUNP_CFT_9_2_5DEG	**41**
	CMUP_CFT_9_2_5DEG	**109**
	CMX_CFT_9_2	**8**
	CMX_CFT_13	**4**
	MET_35_NOT_GAS	**1**
	Total	**1,020**
Not Required	CEM_6_SEED_5_SH_4_CFT_6	8
	CEM_5_CFT_4_8	23
	CMUP_CFT_6_5DEG	2
	TWO_CEM_5_CFT_4_8	26
	TWO_CMU_ONE_CFT_3	7
	CMX_ONE_CMU_CFT_3	3
	CMU_OR_CMX_ONE_CMX_CFT_3_ET	0
	CEM_5_CFT_4_8_CMU_3	0
	CEM_5_CFT_4_8_CMX_3_ET	1
	Total	70
Unidentified Origin	-	22

Table G.3

Run 1A SUSY dilepton events passing stop search lepton ID's, cleanup cuts, the required level 1 and level 2 triggers. On a given row the number of events passing the listed trigger, but not passing any of the previous row triggers is shown.

Trigger Status	Run 1A: Level 3 Trigger Name	Events
Required	**MUO1_CMU_CMP_7PT5**	**1,020**
	MUO1_CMU_ONLY_15PT0	**28**
	MUO1_CMX_10PT0	**18**
	MUO1_CMP_ONLY_7PT5	**10**
	ELE1_CEM_9_6	**231**
	ELE1_CEM_15_10	**95**
	LE1_CEM_8	**211**
	EXO1_MET_30_COSFLT	**0**
	Total	**945**
Not Required	ELE1_CEM_20GEV_NOTRK	0
	EXO1_MET_30_TRK_3	0
	Total	0
Unidentified Origin	-	75

Table G.4

Run 1B SUSY dilepton events passing stop search lepton ID's and cleanup cuts. No special triggers have been required. On a given row the number of events passing the listed trigger, but not passing any of the previous row triggers is shown.

Trigger Status	Run 1B: Level 1 Trigger Name	Events
Required	**L1_CALORIMETER***	**3,242**
	CMU_CMP_6PT0*	**2,061**
	CEM_CMU_OR_CMX*	**115**
	Total	**16,040**
Not Required	L1_4_PRESCALE*	51
	L1_DIELECTRON*	24
	Total	75
Unidentified Origin	-	109

Table G.5

Run 1B SUSY dilepton events passing stop search lepton ID's, cleanup cuts and the required level 1 triggers. On a given row the number of events passing the listed trigger, but not passing any of the previous row triggers is shown.

Trigger Status	Run 1B: Level 2 Trigger Name	Events
Required	**CEM_8_CFT_7_5***	**2,710**
	CEM_12_CFT_12_XCES*	**145**
	CEM_16_CFT_12*	**25**
	CMUP_CFT_7_5_5DEG*	**998**
	CMUP_CFT_12_5DEG*	**561**
	CMNP_CFT_12_5DEG*	**255**
	CMX_CFT_12_5DEG*	**44**
	CEM_5_CFT_4_7_CMU_2_7*	**187**
	CEM_5_CFT_4_7_CMX_2_7*	**9**
	CMX_CMU_TWO_CFT_2_2*	**45**
	TWO_CMU_TWO_CFT_2_2*	**211**
	MET_35_TEX_2_NOT_GAS*	**4**
	Total	**5,194**
Not Required	CEM_5_CFT_4_7_CMUP_2_7*	9
	MET_35_TWO_JETS*	0
	Total	9
Unidentified Origin	-	215

Table G.6

Run 1B SUSY dilepton events passing stop search lepton ID's, cleanup cuts, the required level 1 and level 2 triggers. On a given row the number of events passing the listed trigger, but not passing any of the previous row triggers is shown.

Trigger Status	Run 1B: Level 3 Trigger Name	Events
Required	**ELEB_CEM_8***	**2,777**
	ELEB_CEM_18*	**46**
	MUOB_CMU_CMP_8*	**1,477**
	MUOB_CMU_CMP_15*	**61**
	MUOB_CMP_ONLY_15*	**17**
	MUOB_CMU_ONLY_15*	**95**
	MUOB_CMX_15*	**12**
	EXOB_MET_30_COSFLT*	**4**
	Total	**4,489**
Not	COMBINED_EXOB_DIL	696
	Total	696
Unidentified Origin	-	9

Appendix H: Monte Carlo Generated Stop Signal Files

Table H.1

Monte Carlo generated signal for various $m_{\tilde{t}}$, $m_{\tilde{\nu}}$ scenarios expected in $\int Ldt = 107\ pb^{-1}$. N^{gener} is the number of signal events expected to be produced in $p\bar{p}$ collisions. N_{low}^{final} and N_{high}^{final} are the number of expected events after the final low and high $\Delta(m_{\tilde{t}}, m_{\tilde{\nu}})$ selection cuts were applied. Excl. means excluded by the Run 1 data with our final ensemble of cuts.

$m_{\tilde{t}}$	$m_{\tilde{\nu}}$	N^{gener}	N_{low}^{final}	N_{high}^{final}	Excl.	$m_{\tilde{t}}$	$m_{\tilde{\nu}}$	N^{gener}	N_{low}^{final}	N_{high}^{final}	Excl.
80	50	3,089	17.8	13.9	√	115	70	450	6.5	8.2	√
80	55	3,098	13.2	7.9	√	115	75	450	6.0	6.2	√
80	65	3,075	2.1	0.7	-	115	80	447	4.9	4.6	√
90	45	1,670	22.4	25.4	√	115	85	449	3.9	3.1	-
90	50	1,667	18.6	18.9	√	120	45	353	4.3	7.0	√
90	55	1,679	15.1	14.2	√	120	50	354	4.7	7.9	√
90	65	1,674	7.5	4.6	√	120	55	355	4.7	7.9	√
90	70	1,672	5.7	3.6	√	120	60	354	5.4	8.2	√
90	75	1,668	1.6	0.9	-	120	65	353	5.1	7.7	√
90	80	1,634	0.1	0.3	-	120	70	355	5.4	7.2	√
100	45	955	13.8	20.0	√	120	75	354	5.3	6.8	√
100	50	954	12.4	16.8	√	120	80	354	4.8	5.2	√
100	55	954	13.3	16.4	√	120	85	353	4.2	4.3	√
100	65	959	10.4	9.6	√	120	90	352	3.4	2.7	-
100	75	957	5.7	3.5	√	125	45	281	3.0	5.8	√
100	80	954	3.5	1.7	-	125	50	283	3.9	6.4	√
105	75	736	5.4	4.6	√	125	60	281	3.7	6.0	√
105	80	738	4.6	3.3	√	125	70	284	4.3	6.2	√
105	85	735	2.4	1.5	-	125	80	283	4.1	5.2	√
105	90	736	0.8	0.5	-	125	85	283	4.2	4.6	√
110	45	572	7.9	13.0	√	130	45	226	2.3	4.6	√
110	50	570	7.6	11.8	√	130	50	225	2.4	4.2	√
110	55	573	7.8	11.2	√	130	60	227	3.0	5.1	√
110	65	572	7.9	10.1	√	130	70	225	3.1	5.0	√
110	75	570	6.5	6.3	√	130	80	225	3.3	4.7	√
110	80	571	5.1	4.2	√	130	90	225	3.1	3.3	-
110	85	571	3.6	2.4	-	135	45	182	1.6	3.1	-
115	45	446	6.0	10.0	√	135	50	182	1.7	3.3	-
115	50	448	5.6	9.6	√	135	60	182	1.9	3.6	-
115	55	446	6.1	9.9	√	135	70	182	2.2	3.9	-
115	60	447	6.2	9.2	√	140	80	147	2.0	3.7	-
115	65	446	7.2	9.3	√	145	60	120	1.1	1.9	-

[redacted]

Arnold Pompoš [redacted] He completed his high school education at Gymnazium in Levice in 1989. He continued to study at the Department of Theoretical Physics of the Faculty of Mathematics and Physics at Charles University in Prague, Czech Republic. For his studies he conducted his thesis research "Gravity in Non-Commutative Geometry" as the student of Ctirad Klimčík. In June 1994 he graduated with an M.Sc. in Physics with Summa Cum Laude. In August 1995 he started a Ph.D. program in physics at Purdue University in West Lafayette, Indiana, USA. He joined the CDF collaboration at Fermi National Accelerator Laboratory in 1996, as the student of Daniela Bortoletto and Virgil Barnes, where he conducted his thesis research until completing his thesis in November 2002 and receiving his Ph.D. in Physics in December 2002. Arnold is a member of the Phi Beta Delta Honor Society, and the American Physical Society. He has been awarded the Purdue's George W. Tautfest Memorial Award.